TOWARDS ELECTROCHEMICAL DIAGNOSTICS OF BIOCHEMICAL FREE
RADICAL SPECIES IN AQUEOUS MICROLITER VOLUMES

BY

EDWARD TORRES CHAINANI

DISSERTATION

Submitted in partial fulfillment of the requirements
for the degree of Doctor of Philosophy in Chemistry
in the Graduate College of the
University of Illinois at Urbana-Champaign, 2012

Urbana, Illinois

Doctoral Committee:

      Professor Alexander Scheeline, Chair
      Professor Andrzej Wieckowski
      Professor Arne Pearlstein
      Associate Professor Ryan Bailey

ABSTRACT

Reactive oxygen species (ROS) are free radicals often implicated in disease states. In probing related enzyme processes, reactant consumption must be minimized. Levitated drops show potential as microreactors where radicals are present as reactants or products. Solid/liquid interfaces are absent or minimized, avoiding adsorption and interfacial reaction of conventional microfluidics. Probing small volumes electrochemically requires an integrated sensor with reference, counter-, and one or more working electrodes. Microfabrication allows production of planar gold sensor microelectrodes. A design that placed eight copies of the sensor on a single wafer maximized throughput and use of available substrate area. Titanium was found to be superior to chromium in corrosion resistance while providing adequate adhesion between gold and the polyimide-passivated silicon substrate. A lithographic process using image reversal with lift-off proved superior to etching in terms of line width range, allowing resolution of narrow electrodes (<25 µm) and wider conductive paths. Photosensitive polyimide proved capable of insulating non-electroactive sensor regions, prevented the occurrence of metal delamination encountered in previous electrode designs, as well as defining active electrode areas. Laser milling detached individual electrodes from the wafer and shaped the tip for piercing the levitated drop. The resulting three-electrode sensor with microdisk gold working electrode of radius 19 µm was characterized using ferrocenemethanol in aqueous buffer. Using cyclic

ii

voltammetry, the electrochemically active surface area was estimated by combining a recessed microdisk electrode model with the Randles-Sevcik equation.

Computer-controlled ballistic introduction of reactant droplets into a levitated drop was developed. Chronoamperometric measurements of ferrocyanide with the microfabricated electrode demonstrated the electrochemical monitoring of reactions in a levitated drop, as well as the feasibility of adding reactants ballistically to the drop. Although concentration increases with time due to drop evaporation, it was found to be predictable with a linear evaporation model. Comparison of diffusion-limited currents in pendant and levitated drops shows that convection arising from acoustic levitation causes an enhancement of diffusion-limited current on the order of 16%.

The study of ROS-mediated processes requires a supply of the ROS under investigation. A flow system was designed to generate superoxide radical anion ($O_2^{\bullet-}$) at near-neutral pH by rapid mixing of potassium superoxide dissolved in dimethyl sulfoxide by two-stage mixing with aqueous buffers. This system's intended application is the delivery of $O_2^{\bullet-}$ to bacteria immobilized on filters for investigating attenuation by $O_2^{\bullet-}$ on *Salmonella enterica* serovar *typhimurium*. Measurements of flow rates and calculations of residence times indicate final aqueous $O_2^{\bullet-}$ concentrations up to 50 μM are possible. A spectrophotometric flow cell was devised to confirm the concentration of superoxide.

*This dissertation is dedicated to those struggling with ADHD,
and their loved ones who struggle along with them.*

ACKNOWLEDGEMENTS

the fun times in the lab. I appreciate the help with ZEMAX given by Christopher Nellesen.

The wonderful people of the School of Chemical Sciences (SCS) deserve mention. They have each provided assistance and support that has made my experiments possible and my educational experience all the more valuable.

- Julie Sides of the Analytical Chemistry division, for her untiring support of all graduate students who have come under her wing;

- SCS Machine Shop staff Bill Knight, Mike Harland, Roger Smith, Ed Runyon, Tom Wilson, Dave Hire, Rob Brown, and Brad Lutz for turning my ideas into working devices;

- SCS Electronics Services staff Jim Wentz, Mike Thompson, John Rosheck, and Ben Fisher for their help in developing electronic instrumentation;

- SCS Glass shop staff Don O'Brien, Rich Parrish and Dave Perry for their expertise;

- Mail Room staff Lori Sage-Karlson and Mike Rhoton for the operational support;

- SCS computer wiz Mike Hallock, for assistance with the group server;

- SCS Graphics Services design maven Dorothy Loudermilk for creating the various figures in our posters and presentations and making us look good;

TABLE OF CONTENTS

CHAPTER 1

INTRODUCTION

Radicals are highly reactive species; always looking for another electron to fulfill their valence. Yet aerobic cells use oxygen, a diradical, as the final acceptor in the mitochondrial respiratory electron transport chain.[1, 2] Reactive oxygen species (ROS) is the phrase used to describe the molecules and radicals derived from molecular oxygen. Two-electron transfer to oxygen does not produce radicals. However, some intermediates along the chain can transfer a single electron to oxygen to produce the oxygen radical anion, superoxide. [3-5] Superoxide is deleterious to the cell, primarily because it is as a precursor for other reactive oxygen species (ROS), such as hydrogen peroxide, peroxynitrite, and hydroxyl radicals, which can cause oxidative damage to lipids, proteins, and DNA.[6-8]

However, ROS play a dual role. Hydrogen peroxide and superoxide may play a role in intracellular signaling,[9, 10] and both play a defensive role against invading pathogens. When foreign organisms stimulate leukocytes, these innate immune cells respond with phagocytosis wherein the pathogens are trapped, and then bombarded with ROS during the so-called respiratory burst, and destroyed. The main enzymatic players are NADPH oxidase, responsible for generating superoxide and hydrogen peroxide, and

myeloperoxidase (MPO), which use these two oxidants to produce other oxidants, such as hypochlorous acid (HOCl).[11] Several antioxidant defenses are in place to prevent the damaging effects of ROS on the cell: superoxide dismutase (SOD) and catalase keep steady-state concentrations of superoxide and hydrogen peroxide at the lowest possible level. Even then, pathophysiological conditions, collectively known as oxidative stress, result from an imbalance between the excessive formation of radicals and antioxidant capacity.[9, 12-14] Despite the vast literature chronicling the advances in understanding the generation and effects of ROS in extremely complex biological systems, there is still a gap in translating the biochemical understanding into cellular mechanisms.[15] On the one hand, there is a need to understand the underlying chemical mechanisms in processes where oxidants are implicated, and for this we need to have specific and accurate detection methods for ROS. Understanding of ROS-mediated cellular processes, on the other hand, relies in part on being able to either drive the production of or supply the ROS in question to the biological system under study. Thus, there is also a need to have a source of ROS on demand for use in biological studies. Chapter 4 discusses the development of an apparatus for delivering superoxide at near-neutral pH.

The complexity of enzyme-driven biochemical systems is staggering. The sheer number of parameters involved has led to the development of systems biology as a tool for studying biological networks.[16, 17] Obtaining kinetic information for an enzyme in a reaction network can be a monumental task. Experimental studies of enzyme kinetics

require a thermostatted reaction vessel and a stirring mechanism so that the reaction kinetics is thermally and spatially homogeneous, and thus, simpler to observe and model than heterogeneous kinetics. In addition, delivery methods for reagents, and multiple sensors to monitor concentrations of enzyme, substrate and product species are needed.[18]

In vitro measurements are carried out to isolate the network under investigation in order to reduce complexity, but this can introduce its own complexities. Radicals can recombine upon coming in contact with the walls of the reaction vessel. Biofilm formation can change enzyme dynamics.[19] Any enzymatic reaction that involves oxygen is dependent on the mass-transport properties of oxygen, which varies with temperature, stirring rate, gas flow rate, solution volume, and surface area.[18] If limited amounts of enzymes or other reagents are to be used, a microfluidic reaction vessel is a must, but conventional microfluidic devices have large adsorption surface area in proportion to volume.[20] Although polydimethylsiloxane (PDMS) is highly permeable to low molecular weight gasses, controlling oxygen concentration in a microfluidic device requires some engineering.[21] What could be better than a reaction vessel without walls? Levitation of small volumes of sample in air can be used to avoid contact with solid walls.[22] Levitation has advantages similar to those of lab-on-chip methods, yet avoids the wall effects mentioned earlier. Contamination between the sample and external objects is prevented.

3

An apparatus for acoustic levitation has been described as far back as 1933.[23] Welter and Neidhart reported on the earliest applications of acoustic levitation to analytical chemistry.[24] Many more analytical applications have been reported since.[25-34] This dissertation employs the levitated drop reactor developed by Field, Pierre and Scheeline[27, 31, 35, 36] to add electrochemistry to the growing list of methods applied to a levitated drop. Because of the small size of the drop (1 to 2 millimeters in diameter), a microelectrode must be used, lest the geometry be that of a sessile, stationary drop on a planar surface rather than a levitated drop with continuous circulation. Since an electrode is an added solid, creating a solid-liquid interface, the ideal of no solid-liquid interfaces is, of course, not perfectly obtained. The goal was to eventually create electrodes for simultaneous oxygen, superoxide, and hydrogen peroxide monitoring in the myeloperoxidase (MPO) reaction network. [37-39] For the present, it will suffice to demonstrate fundamental electrochemical measurements such as cyclic voltammetry and chronoamperometry in the levitated drop, as well as the use of drop-on-demand (DOD) sample injection. Chapters 2 and 3 discuss the fabrication of the microelectrode, its characterization and its use in the levitated drop.

The original motivation for the development of a microfabricated electrode came from a suggestion to investigate the mechanism of noise-induced hearing loss (NIHL). Approximately 5% of the population worldwide suffers from industrial, military or

recreational NIHL at a great economic cost and detriment to the quality of life of the affected individuals. Across the world, the loss of hearing in adults attributed to occupational noise is estimated to be at 16%. [40] Approximately 10 million adults and 5.2 million children in the US are already suffering from irreversible noise-induced hearing impairment and 30 million more are exposed to dangerous levels of noise each day. [41] Varying degrees of deafness afflict 30 million Americans and cost the nation almost $56 billion annually. Fifteen percent of Americans between the ages of 20 and 69 have high frequency hearing loss that may have been caused by exposure to loud sounds or noise at work or in leisure activities. The mechanism of NIHL points to reduced blood flow, disruption of calcium homeostasis and oxygen radical production in the cochlea after exposure to sound volumes greater than 85 dB.[14, 42, 43] Additional pathways that cause death of neuronal cells have been identified: Fessenden and Schacht [44] have proposed a model wherein calcium influx activates nitric oxide synthase (NOS) in auditory neurons, thereby driving production of NO, which subsequently reacts with superoxide to form the highly toxic peroxynitrite radical, ultimately resulting in neural degeneration. The pharmacological interventions currently being investigated for mitigating hearing loss after exposure to noise trauma include antioxidants [45, 46], calcium blockers, [47] NADPH oxidase inhibitors [48] and others [43, 49], and point to a complex mechanism involving numerous actors. The cochlear volume is a small space (about 30, 5 and 1 μl, respectively for a human, guinea pig and gerbil *scala tympani*). [50, 51] Demonstrations of *in vivo* electrochemical sensors made from glass capillaries demonstrates the utility of a

microscale sensor. [52] A capillary is a single-species sensor. Ideally, one would prefer to monitor multiple species, thereby requiring several capillaries, which would take up too much cochlear space. A microfabricated sensor with multiple sensing elements for several ROS could accomplish this goal. It would contribute to the investigation of the mechanism of NIHL and might even accelerate the development of discoveries for treatments of NIHL. Rebekah Wilson's work [53, 54] is a step in that direction. Improvements made in sensor design and fabrication since that work are described in Chapter 2.

For an instrument to remain useful, its development must be continued. Certainly, there are further directions to take in the evolution of the levitated drop reactor, and a few are mentioned in brief here: A controlled environment where the humidity, temperature and gas composition in the immediate vicinity of the levitated drop are regulated can slow evaporation of the drop to allow for longer experiments. Enhanced mixing in the drop will enable the investigation of fast reactions. Microfabrication can continue to provide multi-species sensors. Interfacing of the LDR to other instruments such as a mass spectrometer will allow it to be used in identifying reaction intermediates. Chapter 5 provides details of these suggestions.

1.1 References

1. Turrens, J. F., Mitochondrial formation of reactive oxygen species. *J. Physiol.* **2003,** *552,* 335-344.

2. Murphy, M. P., How mitochondria produce reactive oxygen species. *Biochem. J.* **2009,** *417,* 1-13.

3. Misra, H. P.; Fridovich, I., The Univalent Reduction of Oxygen by Reduced Flavins and Quinones. *J. Biol. Chem.* **1972,** *247,* 188-192.

4. Massey, V., Activation of molecular oxygen by flavins and flavoproteins. *J. Biol. Chem.* **1994,** *269,* 22459-22462.

5. Gadda, G., Oxygen Activation in Flavoprotein Oxidases: The Importance of Being Positive. *Biochem.* **2012,** *51,* 2662-2669.

6. Radi, R.; Beckman, J. S.; Bush, K. M.; Freeman, B. A., Peroxynitrite-induced membrane lipid peroxidation: The cytotoxic potential of superoxide and nitric oxide. *Arch. Biochem. Biophys.* **1991,** *288,* 481-487.

7. Dalle-Donne, I.; Scaloni, A.; Giustarini, D.; Cavarra, E.; Tell, G.; Lungarella, G.; Colombo, R.; Rossi, R.; Milzani, A., Proteins as biomarkers of oxidative/nitrosative stress in diseases: The contribution of redox proteomics. *Mass Spectrom. Rev.* **2005,** *24,* 55-99.

8. Imlay, J. A., Pathways of Oxidative Damage. *Annu. Rev. Microbiol.* **2003,** *57,* 395-418.

9. Loor, G.; Kondapalli, J.; Iwase, H.; Chandel, N. S.; Waypa, G. B.; Guzy, R. D.; Vanden Hoek, T. L.; Schumacker, P. T., Mitochondrial oxidant stress triggers cell death in simulated ischemia–reperfusion. *Biochimica et Biophysica Acta (BBA) - Molecular Cell Research* **2011,** *1813,* 1382-1394.

10. Devadas, S.; Zaritskaya, L.; Rhee, S. G.; Oberley, L.; Williams, M. S., Discrete generation of superoxide and hydrogen peroxide by T cell receptor stimulation: selective regulation of mitogen-activated protein kinase activation and Fas ligand expression. *J. Exp. Med.* **2002,** *195,* 59-70.

11. Winterbourn, C. C.; Kettle, A. J., Redox Reactions and Microbial Killing in the Neutrophil Phagosome. *Antioxid. Redox. Sign.* **2012,** .

12. Bostwick, D. G.; Alexander, E. E.; Singh, R.; Shan, A.; Qian, J.; Santella, R. M.; Oberley, L. W.; Yan, T.; Zhong, W.; Jiang, X.; Oberley, T. D., Antioxidant enzyme expression and reactive oxygen species damage in prostatic intraepithelial neoplasia and cancer. *Cancer* **2000,** *89,* 123-134.

13. Cutler, R. G. ; Rodriguez, H., *Critical reviews of oxidative stress and aging: advances in basic science, diagnostics and intervention,* World Scientific, New Jersey, 2003.

14. Henderson, D.; Bielefeld, E. C.; Harris, K. C.; Hu, B. H., The Role of Oxidative Stress in Noise-Induced Hearing Loss. *Ear & Hearing* **2006,** *27,* 1-19.

15. Winterbourn, C. C., Reconciling the chemistry and biology of reactive oxygen species. *Nat Chem Biol* **2008,** *4,* 278-286.

16. Kitano, H., Computational cellular dynamics: a network–physics integral. *Nat. Rev. Mol. Cell Biol.* **2006,** *7,* 163-163.

17. van Riel, N. A. W., Dynamic modelling and analysis of biochemical networks: mechanism-based models and model-based experiments. *Briefings in Bioinformatics* **2006,** *7,* 364-374.

18. McDonald, A. G.; Tipton, K. F., Computer-Controlled System for the Study of Oxidase Reactions: Application to the Peroxidase–Oxidase Oscillator. *J Phys Chem B* **2010,** *114,* 16244-16252.

19. Lewis, D. D.; Ruane, M. L.; Scheeline, A., Biofilm Effects on the Peroxidase–Oxidase Reaction. *J Phys Chem B* **2006,** *110,* 8100-8104.

20. Scheeline, A.; Behrens, R. L., Potential of levitated drops to serve as microreactors for biophysical measurements. *Biophys. Chem.* **2012,** *165–166,* 1-12.

21. Polinkovsky, M.; Gutierrez, E.; Levchenko, A.; Groisman, A., Fine temporal control of the medium gas content and acidity and on-chip generation of series of oxygen concentrations for cell cultures. *Lab Chip* **2009,** *9,* 1073-1084.

22. Vandaele, V.; Lambert, P.; Delchambre, A., Non-contact handling in microassembly: Acoustical levitation. *Precis Eng* **2005,** *29,* 491-505.

23. Bücks, K.; Müller, H. Z., Über einige Beobachtungen an schwingenden Piezoquarzen und ihrem Schallfeld. *Z. Phys.* **1933,** *84,* 75-86.

24. Welter, E.; Neidhart, B., Acoustically levitated droplets — a new tool for micro and trace analysis. *Fresenius J. Anal. Chem.* **1997,** *357,* 345-350.

25. Santesson, S.; Nilsson, S., Airborne chemistry: acoustic levitation in chemical analysis. *Anal. Bioanal. Chem.* **2004,** *378,* 1704-1709.

26. Priego-Capote, F.; de Castro, L., Ultrasound-assisted levitation: Lab-on-a-drop. *TrAC, Trends Anal. Chem.* **2006,** *25,* 856-867.

27. Field, C. R.; Scheeline, A., Design and implementation of an efficient acoustically levitated drop reactor for in stillo measurements. *Rev. Sci. Instrum.* **2007,** *78,* 125102.

28. Delißen, F.; Leiterer, J.; Bienert, R.; Emmerling, F.; Thünemann, A., Agglomeration of proteins in acoustically levitated droplets. *Anal. Bioanal. Chem.* **2008,** *392,* 161-165.

29. Schiffter, H.; Lee, G., Single-droplet evaporation kinetics and particle formation in an acoustic levitator. Part 1: Evaporation of water microdroplets assessed using boundary-layer and acoustic levitation theories. *J. Pharm. Sci.* **2007,** *96,* 2274-2283.

30. Schiffter, H.; Lee, G., Single-droplet evaporation kinetics and particle formation in an acoustic levitator. Part 2: Drying kinetics and particle formation from microdroplets of aqueous mannitol, trehalose, or catalase. *J. Pharm. Sci.* **2007,** *96,* 2284-2295.

31. Pierre, Z. N.; Field, C. R.; Scheeline, A., Sample Handling and Chemical Kinetics in an Acoustically Levitated Drop Microreactor. *Anal. Chem.* **2009,** *81,* 8496-8502.

32. Lorenzen, E.; Lee, G., Slow motion picture of protein inactivation during single-droplet drying: A study of inactivation kinetics of l-glutamate dehydrogenase dried in an acoustic levitator. *J. Pharm. Sci.* **2012,** *101,* 2239-2249.

33. Santesson, S.; Andersson, M.; Degerman, E.; Johansson, T.; Nilsson, J.; Nilsson, S., Airborne Cell Analysis. *Anal. Chem.* **2000,** *72,* 3412-3418.

34. Tuckermann, R.; Puskar, L.; Zavabeti, M.; Sekine, R.; McNaughton, D., Chemical analysis of acoustically levitated drops by Raman spectroscopy. *Anal. Bioanal. Chem.* **2009,** *394,* 1433-1441.

35. Field, C. R., *Developments in Analytical Chemistry: Acoustically Levitated Drop Reactors for Enzyme Reaction Kinetics and Single-walled Carbon Nanotube-based Sensors for Detection of Toxic Organic Phosphonates,* Ph.D. Thesis, University of Illinois at Urbana-Champaign, 2009.

36. Pierre, Z. N., *Acoustically-levitated Drop Reactor (LDR) employable for Kinetics Measurements of Biochemical Networks,* Ph.D. Thesis, University of Illinois at Urbana-Champaign, 2011.

37. Sliskovic, I.; Abdulhamid, I.; Sharma, M.; Abu-Soud, H. M., Analysis of the mechanism by which tryptophan analogs inhibit human myeloperoxidase. *Free Radical Bio. Med.* **2009,** *47,* 1005-1013.

38. Kettle, A. J.; Maroz, A.; Woodroffe, G.; Winterbourn, C. C.; Anderson, R. F., Spectral and kinetic evidence for reaction of superoxide with compound I of myeloperoxidase. *Free Radical Bio. Med.* **2011,** *51,* 2190-2194.

39. Kettle, A. J.; Anderson, R. F.; Hampton, M. B.; Winterbourn, C. C., Reactions of Superoxide with Myeloperoxidase. *Biochem.* **2007,** *46,* 4888-4897.

40. Nelson, D. I.; Nelson, R. Y.; Concha-Barrientos, M.; Fingerhut, M., The global burden of occupational noise-induced hearing loss. *Am. J. Ind. Med.* **2005,** *48,* 446-458.

41. Seidman, M. D.; Standring, R. T., Noise and Quality of Life. *Int. J. Environ. Res. Public Health* **2010,** *7,* 3730-3738.

42. Yamane, H.; Nakai, Y.; Takayama, M.; Konishi, K.; Iguchi, H.; Nakagawa, T.; Shibata, S.; Kato, A.; Sunami, K.; Kawakatsu, C., The Emergence of Free Radicals after Acoustic Trauma and Strial Blood Flow. *Acta Oto-Laryngol.* **1995,** *115,* 87-92.

43. Le Prell, C. G.; Yamashita, D.; Minami, S. B.; Yamasoba, T.; Miller, J. M., Mechanisms of noise-induced hearing loss indicate multiple methods of prevention. *Hear. Res.* **2007,** *226,* 22-43.

44. Fessenden, J. D.; Schacht, J., The nitric oxide/cyclic GMP pathway: A potential major regulator of cochlear physiology. *Hear. Res.* **1998,** *118,* 168-176.

45. Fetoni, A. R.; Troiani, D.; Eramo, S. L.; Rolesi, R.; Paludetti, T., Gaetano., Efficacy of different routes of administration for Coenzyme Q10 formulation in noise-induced hearing loss: Systemic versus transtympanic modality. *Acta Oto-Laryngol.* **2012,** *132,* 391-399.

46. Xiong, M.; He, Q.; Lai, H.; Wang, J., Astragaloside IV inhibits apoptotic cell death in the guinea pig cochlea exposed to impulse noise. *Acta Oto-Laryngol.* **2012,** *132,* 467-474.

47. Shen, H.; Zhang, B.; Shin, J.; Lei, D.; Du, Y.; Gao, X.; Wang, Q.; Ohlemiller, K. K.; Piccirillo, J.; Bao, J., Prophylactic and therapeutic functions of T-type calcium blockers against noise-induced hearing loss. *Hear. Res.* **2007,** *226,* 52-60.

48. Park, J. S.; Kim, S. W.; Park, K.; Choung, Y. H.; Jou, I.; Park, S. M., Pravastatin attenuates noise-induced cochlear injury in mice. *Neuroscience* **2012,** *208,* 123-132.

49. Oishi, N., Emerging treatments for noise-induced hearing loss. *Expert Opin. Emerg. Drugs* **2011,** *16,* 235.

50. Salt, A. N., "Inner Ear Fluid Space Dimensions," http://oto2.wustl.edu/cochlea/model/cochdim.htm. (last accessed 8/10/2012).

51. Thorne, M.; Salt, A. N.; DeMott, J. E.; Henson, M. M.; Henson Jr., O. W.; Gewalt, S. L., Cochlear Fluid Space Dimensions for Six Species Derived From Reconstructions of Three-Dimensional Magnetic Resonance Images. *Laryngoscope* **1999,** *109,* 1661-1668.

52. Liu, J.; Yu, P.; Lin, Y.; Zhou, N.; Li, T.; Ma, F.; Mao, L., In Vivo Electrochemical Monitoring of the Change of Cochlear Perilymph Ascorbate during Salicylate-Induced Tinnitus. *Anal. Chem.* **2012,** *84,* 5433-5438.

53. Wilson, R. C. K., *Micron-scale Flexible Electrodes for Detection of Reactive Oxygen Species for in vivo Applications*, Ph.D. Thesis, University of Illinois at Urbana-Champaign, 2010.

54. Wilson, R. C. K.; Phuong, D. T.; Chainani, E.; Scheeline, A., Flexible, micron-scaled superoxide sensor for in vivo applications. *J. Electroanal. Chem.* **2011,** *662,* 100-104.

CHAPTER 2

DESIGN AND FABRICATION OF MICRON-SCALE ELECTRODES

2.1 Introduction

Microelectrodes are electrodes with characteristic dimensions in the micrometer or sub-micrometer scale.[1] Traditionally, microelectrodes were made by sealing a metal wire in a glass capillary, then polishing the tip to reveal a metal disk inlaid in the insulating glass.[2] In fact, for the smallest diameter nanoelectrodes, this technique is often the only way by which such electrodes can be made. But for probing small volumes, the three electrodes (working, counter-, and reference) should be integrated together into a single, microfabricated sensor. This is advantageous in cases where there is no current return path, such as in a microliter-volume levitated drop[3], or *in vivo* investigations of inner-ear chemistry.[4] This chapter describes the fabrication of 3-electrode probes with tip widths of less than 0.5 mm.

By definition, a microelectrode has one dimension below 25 micrometers, which is smaller than the diffusion layer thickness for small aqueous ions at times greater than ~1 s after a potential step. While the current response decreases in proportion to electrode area, there are certain advantages to using electrodes with small areas:

- The ohmic drop increases with decreasing radius, specifically the uncompensated resistance is given by: $R_u = \frac{1}{4\pi\kappa r_0}$.

- Decreased double-layer capacitance, which is proportional to electrode area: $C_d = \pi r_0^2 C_d^0$, where C_d^0 is the specific interfacial capacitance (capacitance per unit area).

- Multiplying the above equations together results in the following expression for the time constant, $R_u C_d = \frac{\pi r_0 C_d^0}{4\kappa}$. This shows that a decreased radius shortens the time required to change the double-layer charge. As it is not meaningful to impose a potential step on a time scale shorter than the cell time constant, a microelectrode translates to faster experimental times.

- Diffusion to a disk electrode changes linear diffusion (Cottrellian behavior) to the hemispherical diffusion regime for a microdisk at long times. When this happens, steady-state conditions are rapidly established where the rate of electrolysis is equal to the rate at which molecules diffuse to the surface.

With today's potentiostats having current sensitivities in the picoamp or femtoamp range, the low currents are no longer a cause for concern. It should be noted that true steady-state behavior can be achieved rapidly only at electrodes of very small electrode areas. However, the main advantage that is being exploited in this work is that the small size and integration of multiple electrodes allows electrochemical probing of small sample volumes, such as those *in vivo* or in microliter-volume liquid drops.

Lithography and microfabrication have made it possible to create reproducible microelectrodes and electrode microarrays on an appropriate substrate. It is possible to

make arrays with arbitrary shapes and areas, and to designate each electrode as a working, counter-, or reference electrode. Micromachining allows forming or cutting the substrate on which the electrodes reside to a desired length, width, or shape to fit the application.[5] This approach is most useful where the microelectrode will be used with samples of microliter volume, in which case the working, sample, and reference electrodes have to be integrated into a single micro-sensor. Such a case exists for *in vivo* sensing and electrochemical analysis of drops, the latter of which is the topic of the next chapter. This chapter focuses on the design and materials of the sensor necessary to achieve that goal, and the fabrication steps taken to realize such a sensor.

2.2   Sensor Design

The electrode owes much of its lineage to the work done by Rebekah Wilson. The electrode was originally meant to be used as an electrochemical sensor in a levitated drop. Donna Whitlon (Northwestern University) suggested its use for *in vivo* investigations of reactive oxygen species in noise-induced hearing loss (NIHL). Designed to pierce the round window in a Mongolian gerbil cochlea, this restricted the width of the tip of the sensor to 200 microns. To reach the first turn of the cochlea, it was originally designed to be 2.54 cm in length, but with the narrow tip being 3 mm long. The original substrate was a square quartz fiber, which proved to be difficult to pattern by laser ablation. The subsequent substrate was silicon, where a 200-micron

wide tip, 4 inches long, proved to be too brittle. Thus a polyimide substrate, Kapton®, was subsequently chosen. However, problems of adhesion of the metal films to the polyimide substrate became evident, despite the inclusion of an intervening Cr layer between the polyimide and gold, which is known to provide good adhesion for flexible electrodes.[6] Delamination between gold and chromium would indicate a sputtering/deposition problem, while total metal separation would indicate insufficient adhesion of chromium to Kapton®. Based on interfacial energy, the best adhesion layer metal is Cr, followed by Ti, Ta, then Ti/W. These values are derived from mechanical bend tests and do not take into account electrochemical corrosion issues (to be discussed below).

Figure 2.1 shows a microscope image of adhesion failure of Cr/Au electrodes to polyimide. The presence of pinholes in the metallization due to the rough nature of the polymer surface was also noted. The surface area of the electrode was not defined lithographically but by the manual application of a liquid polyimide precursor, which was then cured at high temperature into an insulating film covering most of the metal areas with the exception of the tip.   This made for a large variation in surface area between sensors from one substrate to the next. Despite these challenges, work *in vivo* was demonstrated[4] and the experience informed the current generation of microelectrode design.

For levitated drop work, it was found that the flexibility of the polyimide-based electrode turned out to be a liability because, rather than piercing the drop, the surface tension would deflect away the electrode. A rigid electrode would avoid this issue, so the design of the flexible electrode was adapted to a 3″ diameter silicon substrate. To maximize the use of the silicon wafer, a pattern of 8 sensors arranged around the center was adapted.

Also, an improvement to the layout of the electrodes was suggested by post-doctoral researcher Woo-Hyuck Choi. In the previous design, the electrodes were simply 3 metal strips corresponding to working, counter-, and reference electrodes. The new layout encloses the circular working electrode with the counter-electrode area, with a much smaller disk-shaped reference electrode nearby. The justification for the redesign was that the reference electrode is now placed closer to the working electrode, with the counter-electrode forming a ring around the working electrode, improving current distribution.

To address the delamination issue, two changes had to be made: First, the adhesion layer metal was changed from chromium to titanium to avoid the toxicity of Cr for reasons of biocompatibility. Another reason favoring Ti is that a comparison of the Pourbaix (potential-pH) diagram of Cr and Ti shows that corrosion of Cr produces

primarily soluble products above 1 V vs. NHE even at near- neutral pH, while that of Ti

forms insoluble TiO_2 over the potential range –2.0 V to +2.0 V vs. NHE in the vicinity of

pH 7 (see Figure 2.2).[7] The passivation of the Ti adhesion layer prevents corrosion and

subsequent delamination should electrolyte come into contact with it.

Second, a thin protective insulating film over the metal layer was applied. Apertures in

the film patterned by photolithography define the electrode areas and contact pads.

The resulting coating not only protected the metallization, but also prevented ingress of

electrolytes at the interface between the gold and the adhesion metal, thus preventing

corrosion in the first place. In microelectronic integrated circuit (IC) packaging,

passivation layers of curable polymers are used as stress buffers and vias (etched

openings). A photodefinable polyimide, HD-4100 (HD Microsystems, Parlin, NJ), used

in microelectronics specifically for passivating silicon, was selected for this use. In all, 4

mask patterns were required to define each of the following layers: 1) passivation

(bottom polyimide), 2) metal (lift-off), 3) protective coating (top polyimide) and also 4) a

temporary resist overcoat to protect against debris generated during the laser cutting

process. Figure 2.3 below is a diagram of the layers involved in forming the sensor.

The use of polyimide above and below the gold layer required that both sides of the

gold be coated with adhesion layers of titanium. This requires an additional Ti etch

step to expose the gold after curing the final polyimide layer. Figure 2.4 through Figure

2.11 shows the design and dimensions of the sensor.

2.3   Sensor Fabrication Procedure

2.3.1   *Microfabrication.*

Microfabrication processes were carried out at the Beckman Institute cleanroom at the University of Illinois. Blank 3-inch silicon (<100>, N type) wafers, typically 285 µm thick (WRS Materials, San Jose, CA) were cleaned with water and solvents and baked on a hotplate at 200 °C for 5-10 min to drive off surface-bound water. HD-4100 polyimide resist (HD MicroSystems, Parlin, NJ) was spin-coated onto the wafer at 5000 rpm using a Cee 200X spin coater (Brewer Science, Rolla, MO) to a film thickness of 4 µm (when cured). The resist edge-bead was removed with a spatula and post-baked according to the recommended procedure. The passivation mask was used to expose the polyimide on the Kasper 2001 aligner/exposure tool (Kasper Instruments, Mountain View, CA). This was followed by a post-exposure bake and developed using the recommended developer PA-401D and rinsed in PA-400R solutions (HD MicroSystems, Parlin, NJ). The post-development bake was done at 150 °C for 100 s, followed by 200 °C for 100 s. The final cure was carried out on a hotplate (HP 61, Torrey Pines Scientific, Carlsbad, CA) with a nitrogen purge using an inverted glass funnel to keep oxygen levels below 800 ppm as required for the final cure. The recommended temperature program was used: room temperature (RT) to 200 °C at 10 °C min^{-1}; hold 200 °C for 30 min, ramp to 375 °C at 10 °C min^{-1}; hold 375 °C for 60 min; gradual cool to RT.

21

To create the metal pattern, an image reversal resist is laid on the polyimide passivation prior to metal deposition. Image reversal is useful for turning a positive mask into a negative resist pattern. This procedure is an alternative to metal etching, where the tendency is to have narrow lines over-etched and the wide patterns to be under-etched when both wide and narrow features are present in the design. Image reversal is useful for evaporated metal lift-off techniques, since the process results in a negative wall profile.[8] This process retains fine (< 10 µm) features much better than etching a pattern protected by a positive resist. Prior to the use of the lift-off procedure, photoresist patterning followed by metal etching was the procedure used. Poor adhesion of the resist caused undesired etching of metal, and undercutting cause failure of adhesion of metal to substrate.

Polyimide-passivated substrates are cleaned with solvent, then water, and then subjected to O_2 plasma using a Plasmod system (Nordson-MARCH, Concord, CA) for 100 watts, 30 s. The wafer is baked at 180 °C for 2 min to remove the water layer, then cooled to room temperature in a nitrogen atmosphere. An adhesion promoter was made by dissolving 1 g diphenylsilanediol (Sigma-Aldrich, St. Louis, MO) in 200 mL SU-8 developer (MicroChem, Newton, MA) and the resulting solution is spin-coated at 6000 rpm for 60 s and post-baked at 180 °C for 2 min. After cooling to room temperature, AZ 5214E image reversal resist (AZ Electronic Materials, Branchburg, NJ)

is spin-coated at 4000 rpm for 30 sec. After softbaking for 1 min at 95 °C, the resist is exposed using the positive image mask for a total of 19 mJ cm^{-2}, followed by post-exposure bake for 2 min at 120 °C. This temperature is critical for image reversal, as it has to be 5 ° to 10 °C below the thermal cross-linking temperature. This is followed by flood exposure, using no mask, at a dose > 1000 mJ cm^{-2}, which makes the unexposed areas from the image exposure soluble. The pattern is developed with AZ 400 K (AZ Electronic Materials, Branchburg, NJ), diluted 1:5 with distilled water for 60-90 s. The wafer is rinsed with distilled water, dried with nitrogen, and inspected under a microscope. After bake-out for 1 min at 95 °C and O$_2$ plasma 100W for 30 s, the wafer is ready for metal deposition. Metal deposition was carried out on a Temescal e-beam evaporator, at a vacuum < 5×10^{-6} torr. An initial 6 nm Ti adhesion layer is followed by a 100 nm Au layer, with an additional 6 nm Ti adhesion layer over the gold.

Lift-off is carried out by first soaking the wafer in acetone, followed by 180 sec ultrasonication. This is done twice to remove large lift-off areas. Inspection under a microscope reveals if the lift-off process has been completed. If not, additional lift-off is done using 1165 Microposit remover (Shipley Co., Marlborough, MA), made up of N-methyl-2-pyrrolidone or NMP, instead of acetone. Ultrasonication in 1165 remover for 10 min breaks up the lift-off metal into tiny particles and does not harm the cured polyimide. 1165 remover may be heated to 80 °C (no higher, as the flash point of Microposit 1165 is 85 °C) using the hotplate inside a fume hood to hasten the process.

The wafer is rinsed with isopropyl alcohol (electronic grade, Fisher Scientific, Pittsburgh, PA). The metal layer is then covered with a polyimide layer that is spin-coated, patterned and developed, and cured in much the same way as the initial polyimide passivation layer described above.

An additional layer of thick photoresist was found necessary to protect the electrode areas from being covered or marred by debris from the laser cutting process. A 10 μm layer of AZ P4620 photoresist (AZ Electronic Materials, Branchburg, NJ) was spin-coated at 2500 rpm for 60 s. Softbaking at 110 °C 180 s was followed by cooling to room temperature, then exposure with the debris protection layer pattern at a dose of 1500-1700 mJ cm^{-2}. The pattern was developed using AZ 400K diluted with deionized water, 1:4, at immersion time of 60 s at room temperature. The wafer was rinsed with deionized water, dried and placed on a 110 °C hotplate for five minutes. The wafer was inspected after every process step using a Zeiss Axioscope A1. Images were acquired with a Zeiss AxioCam ICc3 color CCD camera using AxioVision LE software (Carl Zeiss, Inc., Thornwood, NY). A calibration slide (MicroBrightField, Inc., Chicago, IL) with both 250 μm and 25 μm grid was used to set the image scale for 2.5x, 10x and 20x microscope objectives.

Laser cutting was carried out in the SCS Machine Shop's Potomac laser system (Lanham, MD). The score lines required 80 passes while the central area in the vicinity of tips,

24

which are cut through completely, required 300 passes for the 3-inch wafer (thickness about 285 μm).

After the laser cutting procedure, the wafer is thoroughly washed with water and isopropyl alcohol. The eight diamond-shaped segments of wafer in the tip area should be dislodged right after the laser cutting procedure. Otherwise, a gentle spray of water will free them while leaving the narrow tips intact. Soaking the wafer with undiluted AZ 400K for 20 min, strips the debris protection layer as well as any debris embedded in it. The wafer is then rinsed with water and solvents and dried with a nitrogen gun. If the presence of organic residue on the metal areas is suspected, oxygen plasma etching is carried out on the wafer. The resulting wafer is shown in Figure 2.12.

The individual sensors can be removed from the wafer by carefully placing the wafer on a cleanroom wipe or glass slide on a flat surface, with the edge of the wipe or slide along the score line and applying pressure on each side of the line until a clean break occurs. This is best done in a manner that causes the wafer to break into halves, then, each half can be further subdivided into quarters, and so on. Because the laser-scored lines did not extend to the wafer edge, it was necessary to use a diamond-tipped scribe and ruler to manually extend the score lines. In retrospect, the laser could have been made to score the lines to the wafer edge, because the 285 μm-thick wafer would be able to endure handling without breaking apart prematurely when taken off the laser mill. A

similar procedure was attempted on thinner (80 µm) wafers, but these proved to be too fragile to undergo the non-automated fabrication process, breaking at the slightest opportunity.

The Ti layer over the gold was removed by soaking the tip and the pad areas in Ti etchant (TFT, Transene Corp., Danvers, MA) while sonicating. Sonication was deemed necessary for the etchant to reach the small recessed areas of the working, counter-, and reference electrodes.

2.3.2 *Metrology and Inspection.*

A 3D optical profiler (Wyko NT 1000, Veeco Instruments, Inc., Plainview, NY) was used to measure the recess depth of the working electrode. The recess depth of the microelectrode was confirmed to be between 7.6 to 7.8 µm using the 3D optical profiler, and the electrode diameter was measured to be 38 µm from calibrated microscope images.   The recess depth (7.8 µm) is close to the designed thickness of the polyimide coating (5 µm cured film), taking into account the possibility of increased feature height near the top corner of the recess pattern, a phenomenon known as "crowning" (also referred to as a "pinched corner"). The reduction in electrode radius (19 µm measured versus 22.5 µm designed) may be attributed to the shallow slope of the wall coupled with the development of "footing" in the polyimide at the bottom of the opening

(adjacent to the metal). The deviation of actual widths from design widths is typical of photosensitive polyimides (PSPI) used to form "vias" (etched openings) in IC packaging in the sense that the actual polyimide via diameters are always smaller than the design diameters. This variation is also a function of the location on the wafer.[9] A study on the optimization of the profile of HD-4000 series photosensitive polyimide was undertaken by HD MicroSystems, the manufacturer, and reported in the 2004 Symposium on Polymers for Microelectronics. A PDF of the symposium presentation is available at the HD MicroSystems website.[10]

2.3.3 CYTOP coating.

Brush coating the inactive portion of the electrode with CYTOP (Asahi Glass Co., Ltd., Tokyo, Japan), a hydrophobic fluoropolymer, prevents wicking of the drop into the body of the electrode. CYTOP type M has isocyanate end functional groups that react directly with silicon surface hydroxyl groups, avoiding the need for surface activation prior to coating. However, the electrode area itself must remain uncoated to allow for contact with the solution. Beyond half a millimeter from the tip, the rest of the body is CYTOP coated. During the coating process, the electrode areas are temporarily protected by the solid lauric acid, which can be easily removed after CYTOP coating. Lauric acid was melted in a small glass dish at 50 °C and the amount of liquid adjusted so that the depth was slightly less than needed to completely submerge the tip. The

sensor tip was dipped into the melted lauric acid and withdrawn to cool and solidify.

CYTOP solution was then applied to the sensor by brush coating a thin layer. CYTOP

coating solution is a 1:1 solution of CT-107M and CT-SOLV, and was applied by brush

coating, then allowed to air dry. The CYTOP-coated electrode was then placed on a

hotplate at 100 °C, at which point the lauric acid melts away. A rinse in isopropyl

alcohol was used to completely remove all lauric acid. To cure the CYTOP, the electrode

is then placed in a reduced-pressure oven (20″ Hg) at 115 °C overnight. This procedure

results in an adherent CYTOP coating that remains bonded even when the sensor is

repeatedly cleaned by ultrasonication.

2.3.4 *Electrical connections.*

An electrochemical sensor requires that electrical connections be made from the sensor

to the potentiostat. The sensor design incorporates large-area pads for this purpose.

Soldering of wire leads to these gold pads is possible, but it is more suitable to use a

spring-loaded electrical connector to create a conducting path to the pads. With a

connector, the sensor can be removed and reattached after calibration, or replaced if

desired. A holder, consisting of polycarbonate blocks mounted to an aluminum rod,

was fabricated in the SCS Machine Shop. Three gold-plated spring contact probes

(GSS103.8G) by Interconnect Devices, Inc. (Kansas City, KS) were embedded at the

appropriate locations within the blocks to make low-resistance connections to the gold pads.

2.4   Conclusions

The fabrication of electrochemical sensors suitable for use in small volumes or in drops using conventional photolithography methods that use a silicon wafer as substrate, has been demonstrated. The method employed aims to maximize the utilization of the wafer surface, and thus makes use of a circular arrangement of the sensors. The metal lift-off process used avoids the inherent difficulties of etching patterns that combine wide and narrow features. The use of a photodefinable polyimide as a masking material over the metal pattern simultaneously insulates non-electrode areas and allows control of the active electrode area. Suitable connectors made from off-the-shelf components were built and used with the sensors. The fabrication method allows for identical sensors to be made efficiently, paving the way for disposable electrochemical sensors for use in *in vivo* investigations.

2.5   References

1. Forster, R. J. and Keyes, T. E., "Behavior of ultramicroelectrodes," in *Handbook of Electrochemistry*, C. G. Zoski, ed. Elsevier, 2007, pp. 155-171.

2. Fan, F. F., Fernandez, J., Liu, B., Mauzeroll, J., and Zoski, C. G., "Platinum and gold inlaid disks ≥5 µm diameter," in *Handbook of Electrochemistry*, C. G. Zoski, ed. Elsevier, 2007, pp. 189-197.

3. Field, C. R.; Scheeline, A., Design and implementation of an efficient acoustically levitated drop reactor for in stillo measurements. *Rev. Sci. Instrum.* **2007,** *78,* 125102.

4. Wilson, R. C. K.; Phuong, D. T.; Chainani, E.; Scheeline, A., Flexible, micron-scaled superoxide sensor for in vivo applications. *J. Electroanal. Chem.* **2011,** *662,* 100-104.

5. Hollenberg, B. A.; Richards, C. D.; Richards, R.; Bahr, D. F.; Rector, D. M., A MEMS fabricated flexible electrode array for recording surface field potentials. *J. Neurosci. Methods* **2006,** *153,* 147-153.

6. Yeager, J. D.; Phillips, D. J.; Rector, D. M.; Bahr, D. F., Characterization of flexible ECoG electrode arrays for chronic recording in awake rats. *J. Neurosci. Methods* **2008,** *173,* 279-285.

7. Bockris, J. O.; Conway, B. E.; Yeager, E. B., *Comprehensive Treatise of Electrochemistry;* Plenum Press, 1980.

8. Madou, M. J., *Fundamentals of Microfabrication: the Science of Miniaturization;* CRC Press, 2002.

9. Daubenspeck, T. H., Petrosky, A. L., Sauter, W., and Ostrowski, K. A., "Evaluation of HD4004 Photosensitive Polyimide for Semiconductor Applications," http://hdmicrosystems.com/HDMicroSystems/en_US/tech_info/tech_info.html. (last accessed 10/23/2012).

10. Dunn, S., "HD-4000 Profile Optimization Through Process Enhancement," http://hdmicrosystems.com/HDMicroSystems/en_US/tech_info/tech_info.html. (last accessed 10/23/2012).

2.6 Chapter 2 Figures
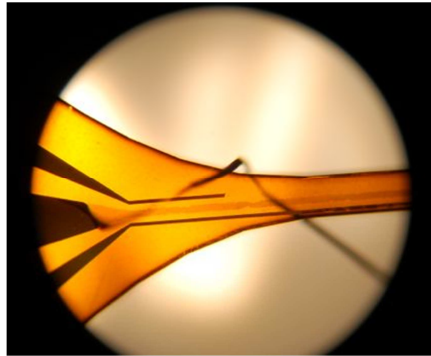
Figure 2.1. Delamination of the metal trace from the polyimide substrate.
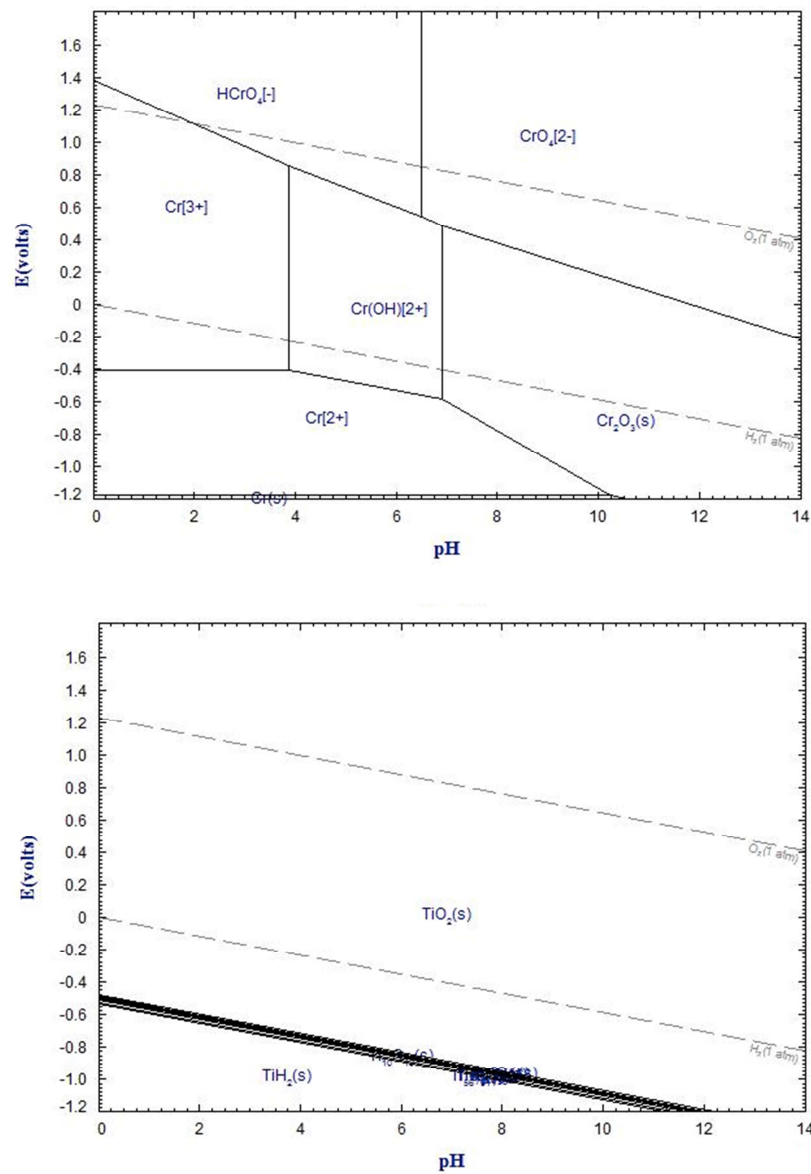
Figure 2.2. Pourbaix diagrams for chromium (top) and titanium (bottom). These diagrams are reproduced with permission from the free version of the FactSage package at http://www.crct.polymtl.ca/factweb.php (Bale, C. W. and Belisle, E.).
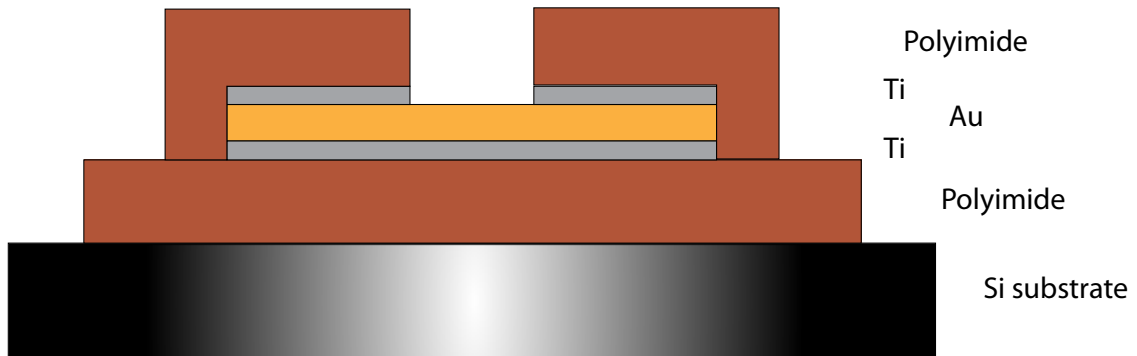
Figure 2.3. Cross-sectional representation of the sensor showing various patterned layers on the silicon wafer. Layer thicknesses are: Si substrate 285μm, basal polyimide 5μm, Ti 6 nm, Au 150 nm, and overlayer polyimide 5μm.
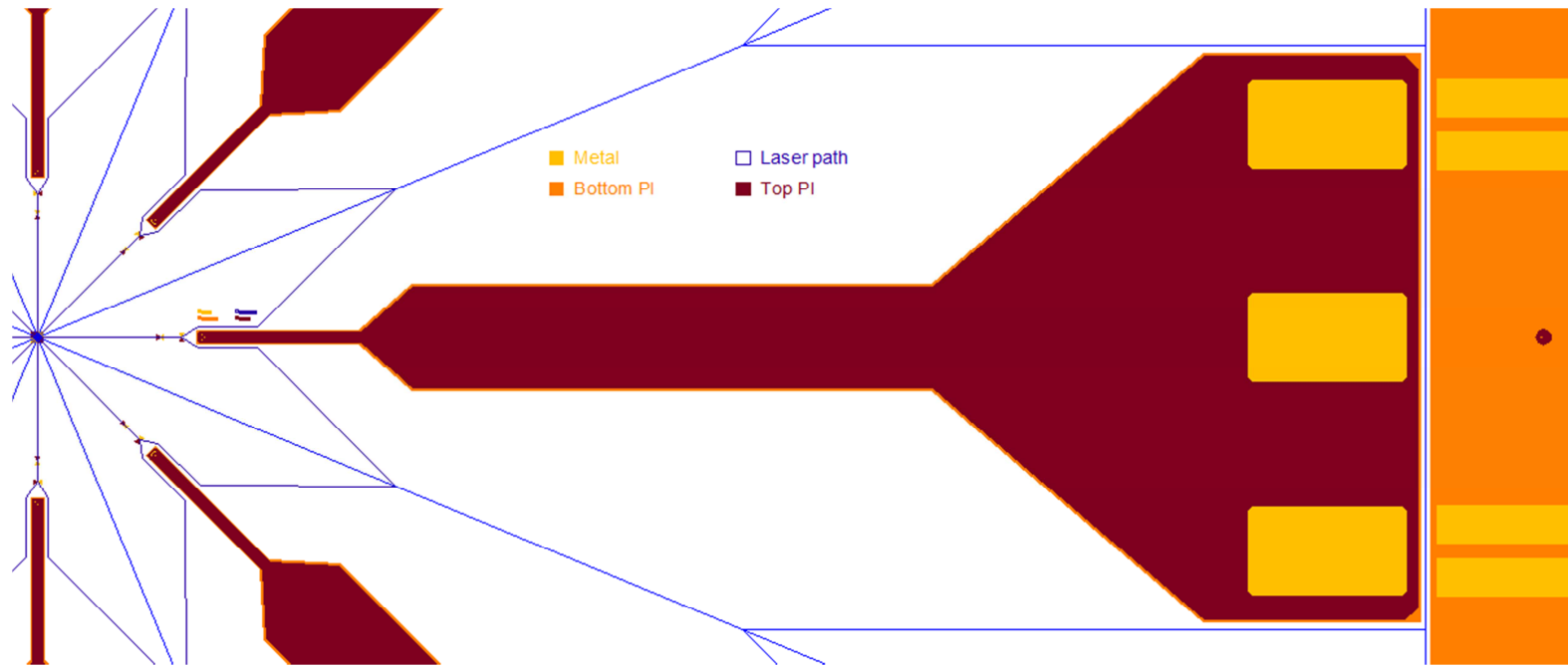
Figure 2.4. Section of mask wafer pattern showing a full electrode, one of eight arranged radially around the wafer center. Each color represents a mask layer for metal, polyimide passivation layers, and laser cutting path. Not shown is a pattern for a temporary protection layer against laser cutting debris.
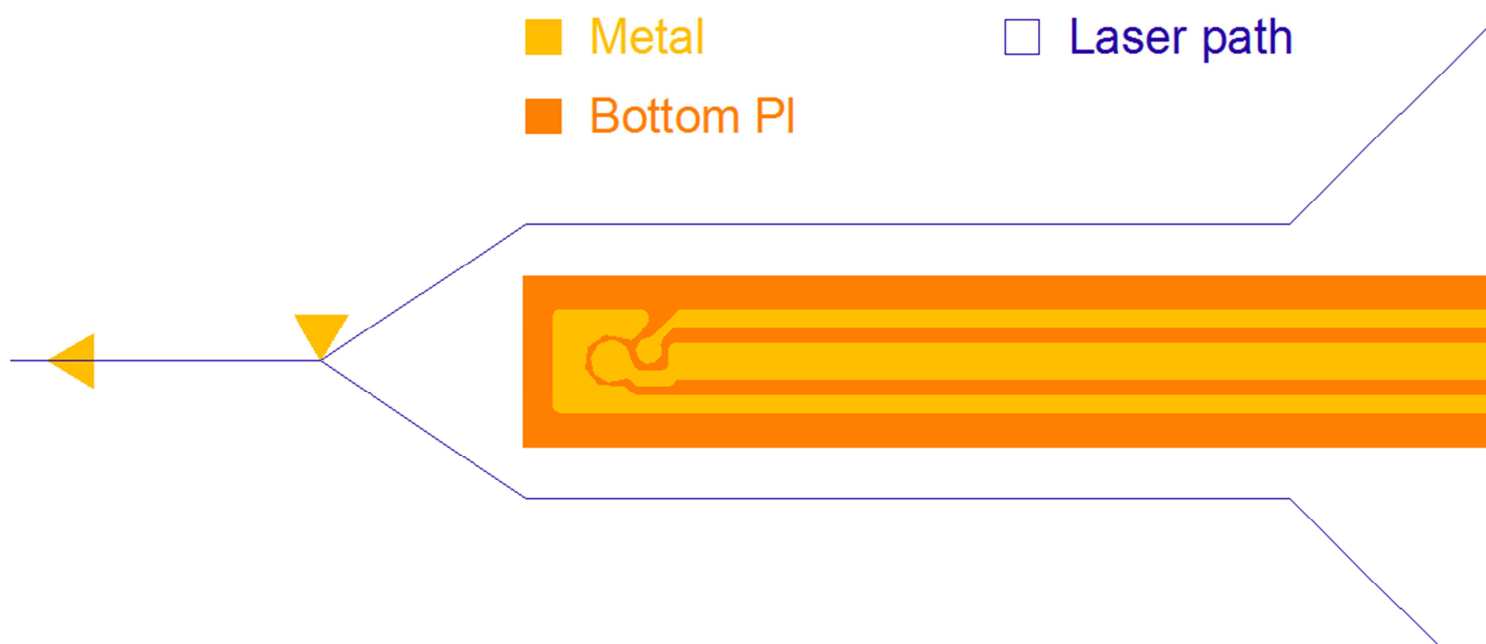
Figure 2.5. Sensor design showing the three-electrode arrangement of the gold layer. Also shown are the passivating polyimide (PI) pattern and laser cutting path.
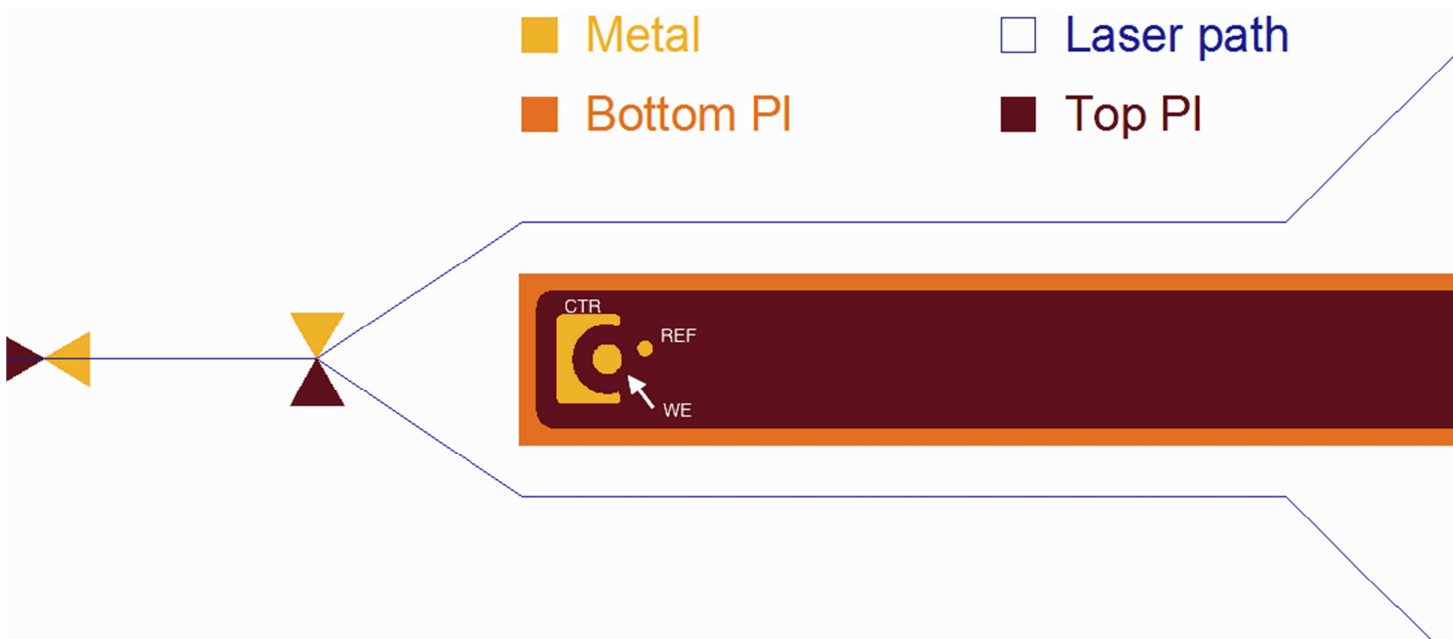
Figure 2.6. Sensor design showing the top polyimide (PI) layer patterned with areas for working, reference, and counter-electrodes.
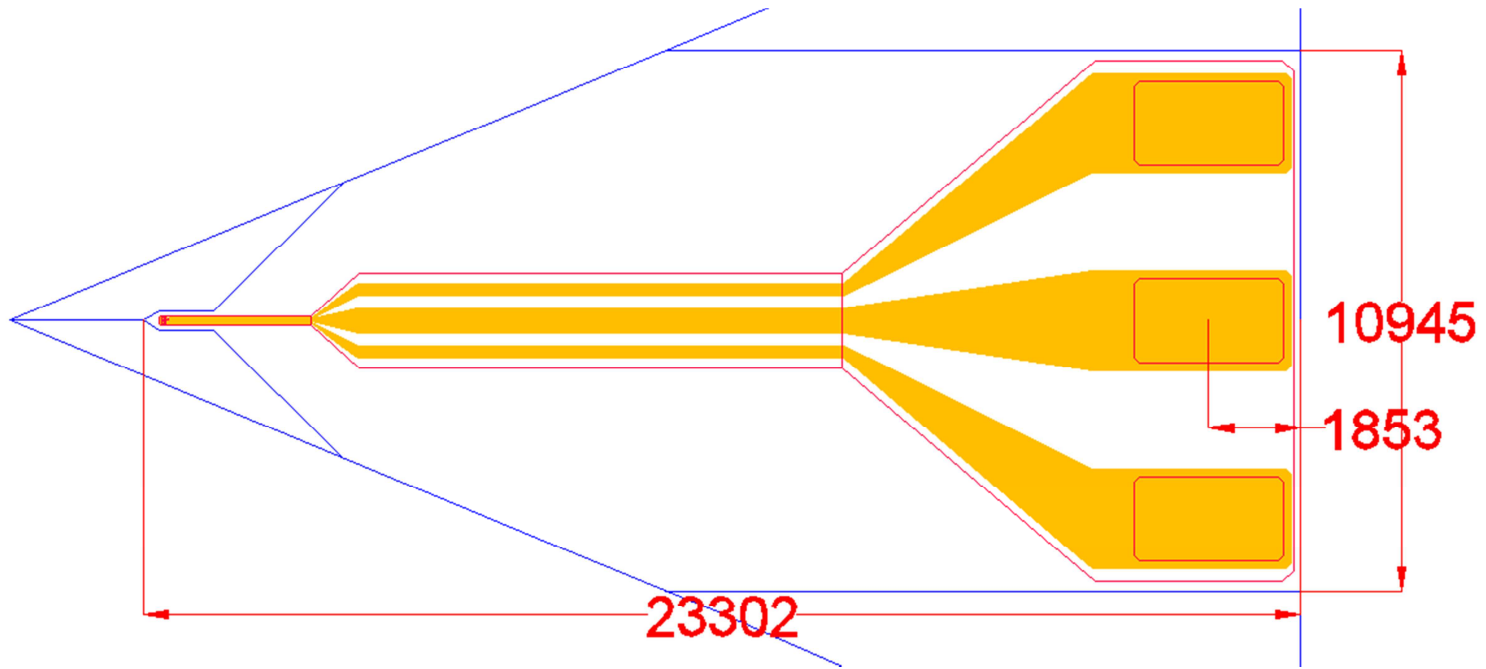
Figure 2.7. Overall dimensions of a single sensor. Units are in micrometers.
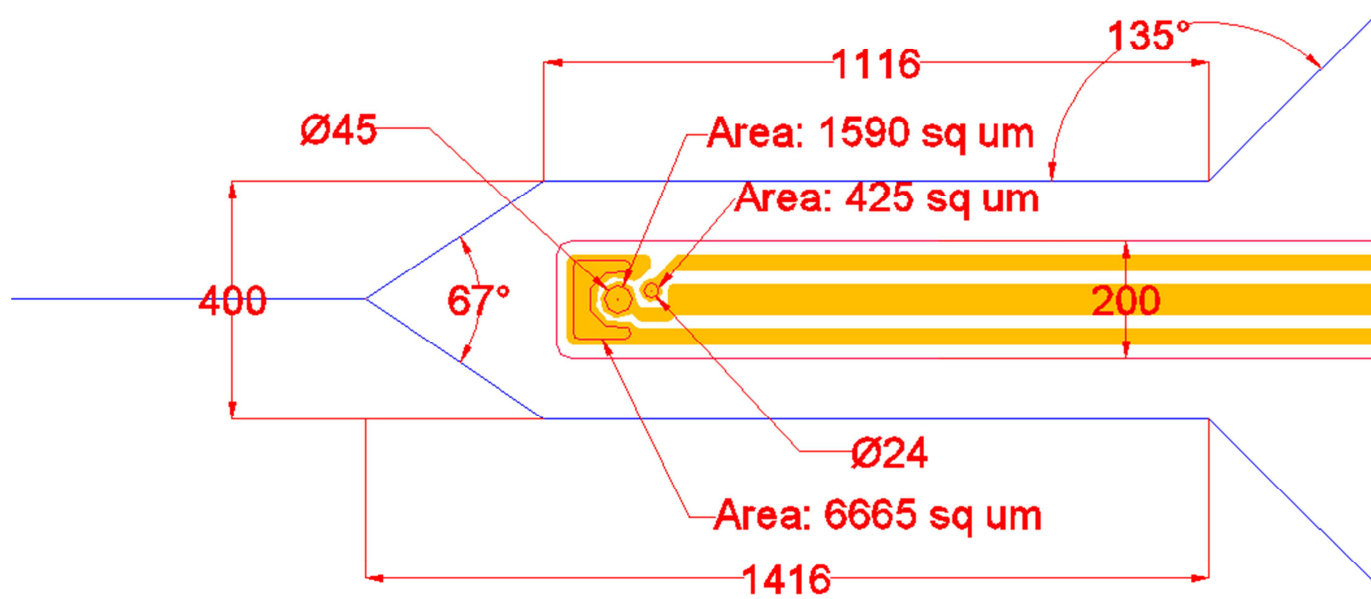
Figure 2.8. Tip dimensions of the sensor.
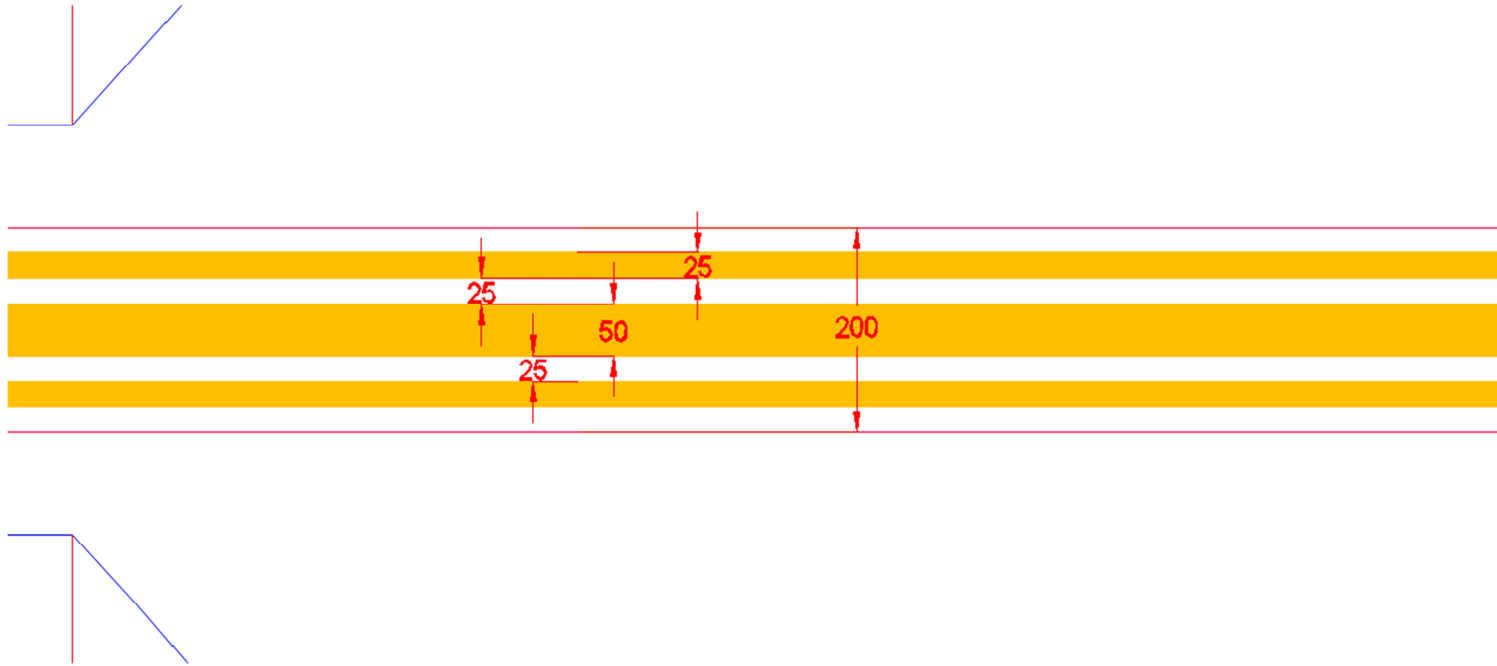
Figure 2.9. Dimensions of the neck area of the sensor. Units are in micrometers.
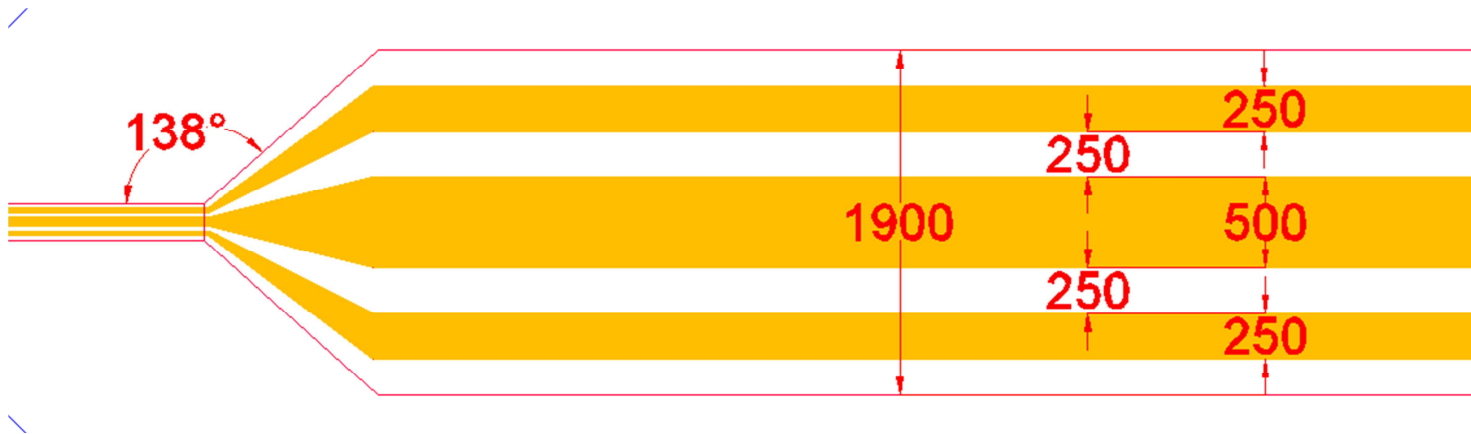
Figure 2.10. Dimensions of the shank area of the sensor. Units are in micrometers.
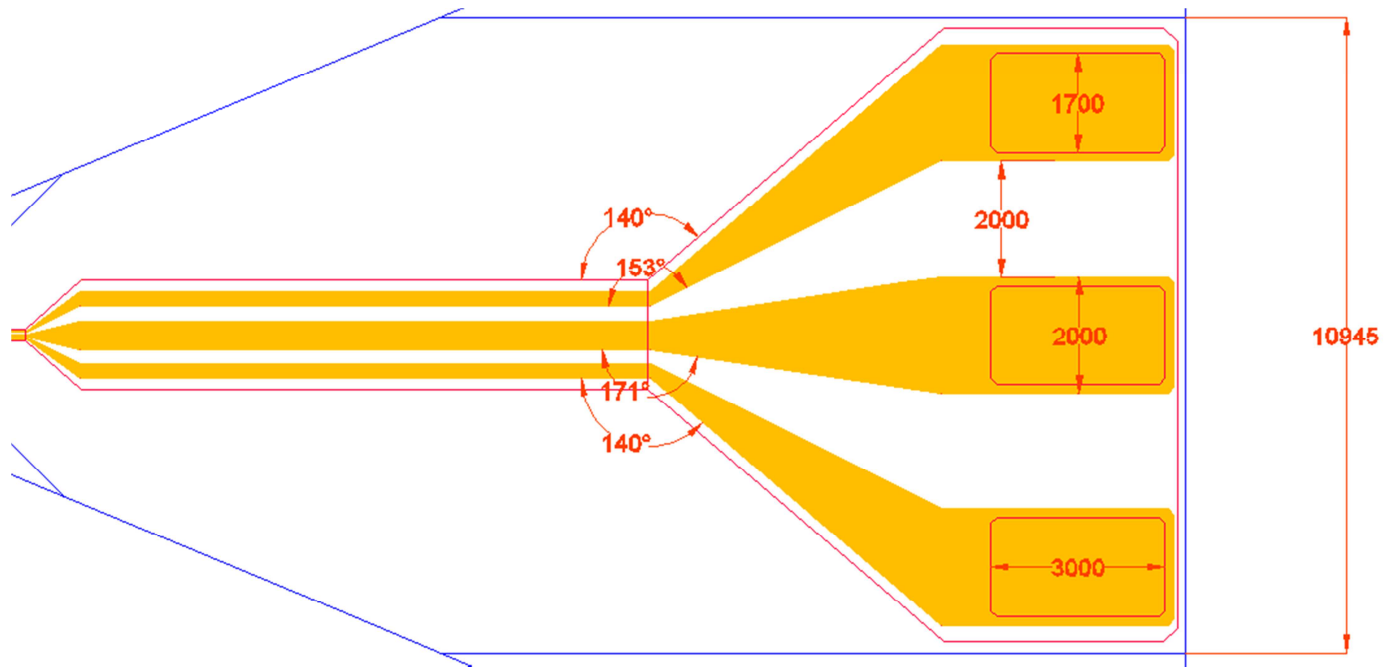
Figure 2.11. Dimensions of the pad area of the sensor. Again, units are in micrometers.

Figure 2.12. Patterned sensors on a 3-inch diameter silicon wafer. The laser-trimmed tips and the laser score lines are visible. The wafer thickness is 285 μm.
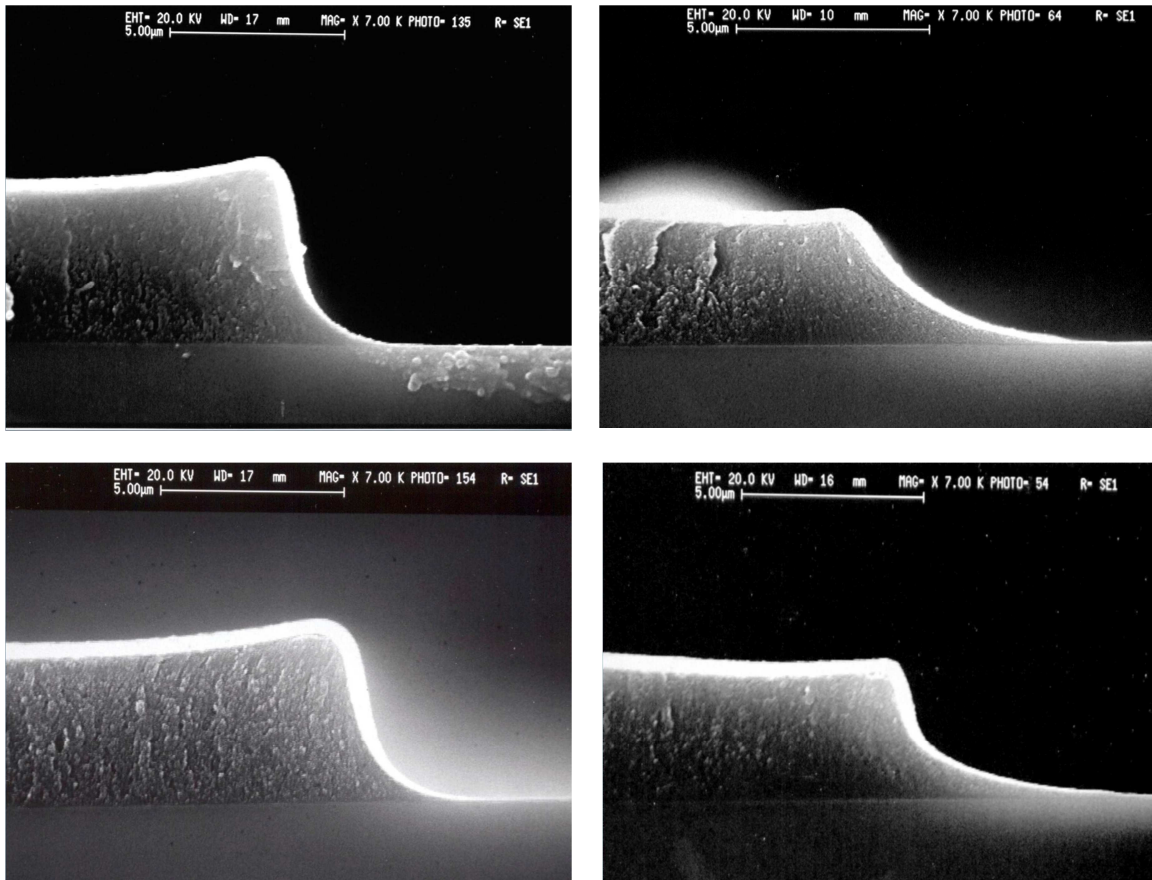
Figure 2.13. Various HD-4000 profiles resulting from variations in processing parameters. Clockwise, from top left: Standard HD-4000 process profile resulting in crowning; post-exposure queue with post-develop bake resulting in shallow slope; post-exposure queue only, resulting in increased footing; and post-develop bake only, best compromise between slope, minimal crowning and footing. Reproduced with permission from HD Microsystems, Inc.

44
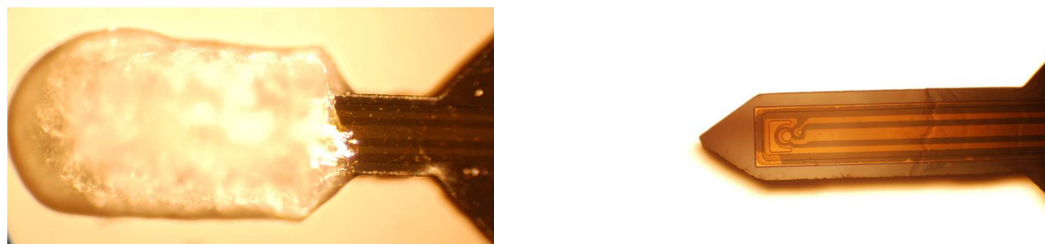
Figure 2.14. Left: Lauric acid coated electrode tip, prior to CYTOP coating. Right: electrode tip after CYTOP coating.
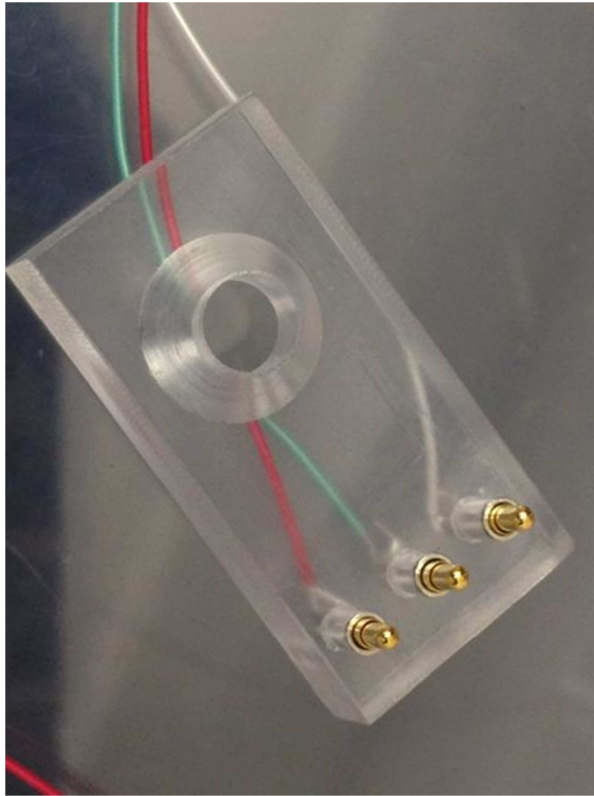
Figure 2.15. Polycarbonate block holder with embedded spring-loaded connectors.

CHAPTER 3

ELECTROCHEMISTRY IN AN ACOUSTICALLY LEVITATED DROP

3.1   Introduction

An acoustically-levitated drop reactor opens avenues of solid-surface-free

microchemical analysis. While most drop characterization has been accomplished by

spectrochemical measurements [1] or mass spectrometry, [2] electrochemical

measurements of the drop may also be implemented with a suitably positioned

microelectrode. Admittedly, introducing an electrode into a drop adds a solid surface,

but with the use of a microelectrode, the added surface area relative to the drop volume

is small; minimizing surface chemical effects compared to other invasive approaches,

and provides sensing modes otherwise not feasible.

Acoustically-levitated drops have distinctive characteristics compared to other

microfluidic systems. Sample volumes in analyses using lab-on-chip, digital

microfluidics (sessile drops on surfaces, moved by changes in surface charge), or

capillary microfluidic systems likewise reduce the amount of analyte required

compared to conventional analytical methods. This is advantageous when working

with limited quantities of difficult-to-obtain compounds such as some enzymes. When

in equilibrium with air, levitated drops allow rapid exchange of O_2 and CO_2 with the

47

surroundings, which is important for studying enzyme-catalyzed reactions or living cells. Continuous-flow reactors may be realized for drops fed and drained by capillaries; a batch micro-reactor results when isolated drops are augmented with a sample introduction system, such as an electrostatic or piezoelectric droplet launcher. Intradrop vortex flow, induced by acoustic pressure, ensures that added reactants are mixed faster than would occur from diffusion alone.

In the 1 to 10-watt ultrasound transducer power range,[3] cavitation and enhanced mass transport of the type demonstrated in higher-wattage sonoelectrochemical experiments[4-6] is unlikely. However, at the acoustic power required to counteract the weight of the drop, the compression and rarefaction of the drop (the 'breathing mode') affords a fluid motion[7-9] that amounts to a stirring or convective streaming that can be investigated by amperometry.

Electrochemical measurement in small volumes has been aided with the development of microfabricated electrodes.[10-12] By way of example, for *in vivo* work, most microelectrodes were traditionally microwires encased in a pulled glass capillary which, when polished, results in an inlaid microdisk electrode. More recently, microfabrication allows arbitrary electrode shapes: Microfluidic electrochemical sensors often take the form of channel microband electrodes for flow-through applications as well as arrays of

microdisks. [13, 14] While there is a multitude of shapes that a microelectrode can take, a microdisk electrode gives a well-characterized voltammetric and chronoamperometric response. And although a wide variety of electrode materials is used (platinum, glassy carbon), gold is a suitable noble metal for use as an electrode material in a microfabricated platform, as it lends itself well to metal deposition and microfabrication techniques, and allows simultaneous electrochemical and spectroscopic monitoring. [15] A gold electrode also allows the formation of self-assembled thiolate monolayers, leading to modified electrodes. [16] This chapter describes the application of a microfabricated planar gold microdisk electrode to the small-volume environment of an ultrasonically levitated drop.

3.2   Experimental

3.2.1   *Apparatus.*

The ultrasonic levitated drop instrument used was previously described in the literature. [3, 17] Voltammetric measurements were made using a Gamry PCI4/FAS2 "Femtostat", controlled by Gamry Framework software (Warminster, PA). Where experiments were done in static solution in a container, a 3.0 M NaCl-filled Ag/AgCl electrode (BASi, West Lafayette, IN) was used with gold wire counter-electrode. For purposes of measuring electrode dimensions, images of the electrode were acquired using a Zeiss Axioscope A1 microscope with a Zeiss AxioCam ICc3 color CCD camera accessory

49

controlled by AxioVision LE software (Carl Zeiss Microscopy, Thornwood, NY). A

calibration slide (MicroBrightField, Inc., Chicago, IL) with both 250 μm and 25 μm grids

was used to set the image scale for 2.5x, 10x and 20x microscope objectives. A 3D optical

profiler (Wyko NT 1000, Veeco Instruments, Inc., Plainview, NY) was used to measure

the recess depth of the working electrode.

3.2.2 *Electrode Fabrication.*

The microelectrode used in experiments done in the levitated drop was fabricated

under clean room conditions. The fabrication procedure was described in detail in the

previous chapter. Briefly, a 3-inch silicon wafer was used as the substrate. Polyimide

was spin-coated on the wafer and cured at elevated temperature to form a passivation

(nonconducting) layer on silicon. Metal layers were subsequently deposited under

vacuum, with gold being the electrode material of choice. After patterning the metal

through lift-off, a protective top coating of photodefinable polyimide was spin-coated,

patterned and cured. This final layer contains the patterns for electrode areas and

contact pads.

3.2.3   Reagents and Solutions.

All chemicals used were of analytical grade and used as received without further
purification. Solvents used for cleaning were isopropyl alcohol (Fisher, electronic
grade) and absolute ethanol (Decon Laboratories, King of Prussia, PA). Solutions were
prepared using 18.2 MΩ cm water (Elga Labwater, Woodridge, IL). A 0.1M sodium
phosphate buffer was prepared by dissolving the appropriate quantities of Na_2HPO_4
and NaH_2PO_4 (EMD Millipore, Billerica, MA) to make a buffer of pH 6.75. Solutions of
ferrocenemethanol (Sigma-Aldrich, St. Louis, MO) was made by dissolving the
appropriate quantity in the above buffer, and filtered with a Millipore (Billerica, MA)
Steri-cup 0.22μm filter.   A 50 mM solution of potassium ferrocyanide was made by
dissolving the appropriate quantity of $K_4Fe(CN)_6$ (Aldrich) in phosphate buffer.

3.2.4   Experimental Procedure.

The microfabricated electrode was cleaned by rinsing in DI water and ethanol.
Sonication for 5 minutes (Ultrasonic Wave Cleaner, Sharper Image, San Francisco, CA)
in ethanol/water solution was also done to clean the recessed electrode areas. The
working and reference electrodes were then cycled in phosphate buffer (-0.1 to 1.1 V
against Ag/AgCl) until a voltammogram characteristic of a gold electrode resulted.
This was found to be useful not only for cleaning the working electrode, but also for
stabilizing the quasi-reference electrode (QRE) potential.

51

The electrode was then characterized in an unstirred container against an Ag/AgCl reference electrode. Cyclic voltammetry of ferrocenemethanol was used to evaluate the electrode characteristics. After characterization in static solution, the electrode was transferred to the levitated drop instrument. The equilibrium position of a freely levitated drop is determined by a high-speed camera (Stingray F-033, Allied Vision Technologies, Newburyport, MA) and marked on the computer monitor. The clean, dry electrode tip is placed close to the equilibrium position. Then, a drop containing ferrocenemethanol of volume 2 to 3 μl is applied by means of a pipette. Pairs of cyclic voltammograms were obtained with and without sound, corresponding to the levitated and pendant drop situations, respectively (see Figure 3.1). Each voltammogram took only 5 seconds to run, however, a minute or two would elapse between experiments, so there was a need to correct for drop evaporation and the consequent increase in concentration with elapsed time. The rate of evaporation was determined in a separate experiment (discussed below) in order to determine the time-dependent correction for the increase in concentration between the first and second experiment in each pair.

For the chronoamperometric (CA) experiments, an induction-based fluidics (IBF) droplet injection system from Nanoliter LLC (Henderson, NV) was used to ballistically launch a 185 nL volume of 50 mM ferrocyanide toward a levitating drop of 2.85 μl initial

volume, suspended on the same electrode used in the CV experiments. The system uses a stepper motor-driven Hamilton syringe (Reno, NV) to dispense a 185 nL droplet at the tip of the syringe needle. A high voltage source supplied with the IBF system delivers a voltage pulse to capacitively charge the droplet, causing its repulsion and detachment from the needle. Because the acoustic levitator components are at ground potential, the charged droplet is electrostatically drawn towards the levitator. The grounded apparatus ensures a constant electrostatic environment into which the drop and droplets can be injected with repeatable trajectories. The arriving droplet is caught in the sound field and is "funneled" to impact with the levitated drop. Undergraduate student Khanh Ngo is undertaking extensive characterization of the drop-on-demand system. Its properties and operation will be described in detail in his Bachelors thesis (UIUC Department of Chemical and Biomolecular Engineering, 2013). As supplied by Nanoliter, a footswitch operates the high voltage supply. To improve the reliability and repeatability of droplet launch, the footswitch was replaced with a solid-state relay activated by trigger outputs generated by USB-6009 control and data-acquisition hardware (National Instruments, Austin, TX). The Stingray high-speed camera system was focused on the drop and electrode and was capable of taking image sequences up to speeds of 150 frames s^{-1}. The high-voltage pulse and camera were both controlled by a program written in LabVIEW (National Instruments, Austin, TX). This allowed the user to adjust the relative timing of droplet launch and camera triggering, enabling

image capture of events prior to, during and after droplet impact for later analysis. The acquired images were analyzed off-line to obtain droplet dimensions using another program written with the "Vision Builder for Automated Inspection" (VBAI) machine vision application (National Instruments, Austin, TX). Droplet volume was calculated based on an oblate-spheroid model (to be discussed in section 3.3.3). Images were calibrated against a 0.5 mm grid printed on film at 5080 dpi resolution (University of Illinois Printing Services). Multiple additions could be made, while the current was monitored at 300 mV against the Au QRE using the Gamry potentiostat. Data on the effect of evaporation on drop volume were obtained by taking camera images of a 2.9 µl levitated drop of 0.1 M phosphate buffer on the electrode over a period of 5 minutes and plotting the calculated volume against time. The volume of the drop was calculated in the same manner described above. It is assumed that the electrode does not significantly distort the drop from an oblate spheroidal shape, and that the volume displaced by the electrode is negligible. Since the maximum displaced volume is ~50 nL (obtained by calculating the volume of the wetted portion of the electrode as 0.2 mm× 0.25mm×1 mm = 0.05 mm^3), the error is ~1%, approximately the level of volume uncertainty. Images taken along the longitudinal axis of the electrode (Figure 3.2) show that surface tension causes the drop to position itself on the electrode surface in a way that the contact between the wettable parts of the tip is minimized. This way, electrode contact was maintained with minimal distortion of drop shape and volume.

3.3 Results and Discussion

3.3.1 *Fabrication*

Gold has been intensively studied as an electrode material. Platinum is the electrode of choice for its hydrogen adsorption and surface catalytic properties, but gold is preferred for its high overpotential for hydrogen evolution, its lower cost and biocompatibility. As an electrode material, gold is extensively used for electrochemical detection in microfluidic systems. It lends itself well to microfabrication techniques such as thin film metallization either through sputtering or evaporation, photolithographic patterning and chemical etching. [18-21] Surface modification of gold with thiol adsorbates[16, 22, 23] allows attachment of a variety of ligands for surface electrochemistry[24-28] and sensing applications. [29-35] The usefulness of gold as an electrode is limited by its surface oxidation at highly positive potentials. The cyclic voltammogram of gold in pH 6.75 phosphate buffer shows that the formation of gold oxide commences around 700 mV vs Ag/AgCl. A further limitation is introduced by surface adsorption of chloride when small amounts of Cl$^-$ are present in solution at millimolar quantities. [36, 37] Gold's surface properties are markedly affected by chloride through surface reconstruction, and increase in specific interfacial capacitance. Anodic dissolution of gold by virtue of complexation to form chloroaurate anion increases roughness. [38] All of the above impact the reproducibility of the electrode. Because of these complications, this study avoided contamination of solution with chloride. Most

electrochemical studies of noble metals are carried out in concentrated 1:1 electrolytes ($HClO_4$, H_2SO_4, KOH, etc.) at either high or low pH. While rarely used as supporting electrolyte in electrochemical studies, phosphate buffer solutions are prevalent in physiological and biochemical studies. There are few studies of phosphate anion adsorption on gold,[36, 39-42] and even fewer at near-neutral pH.[40] These studies suggest that phosphate adsorbability is higher than sulfate adsorption, but is considerably weaker than halide ion adsorption,[42] and is reversible upon cycling the electrode potential.[40] Also, the adsorption of HPO_4^{2-} and PO_4^{3-} starts at the potential of the anodic peak in the gold cyclic voltammogram.[39, 40] This potential region is avoided when investigating redox species in solution. Thus, there is no strong reason to preclude the use of phosphate-containing solutions (used as a buffer in biological research) as a suitable supporting electrolyte. Finally, in most electrochemical investigations, inert gas is bubbled through the solution to remove molecular oxygen, but it is not desirable to do the same in the levitated drop, if biological processes requiring oxygen are to be studied. It was found that below 0 V, reduction of dissolved oxygen occurs at the gold microelectrode. The latter has been reported for both Au and Pt microelectrodes in aqueous solution.[43] Consequently, only in the range of 0 to 700 mV (vs Ag/AgCl), in neutral phosphate buffer solutions in equilibrium with air, does gold behave as an ideal polarizable electrode. This potential range is often referred to as the "double-layer" region: at the gold surface a layer of adsorbed solution ions forms a

firmly held surface charge, and in addition to that, another layer made up of counterions, distributed more diffusely within the solution in contact with the interface.[44]

Cyclic voltammograms of gold in phosphate buffer are shown in Figure 3.3. It is important to note that by keeping the solution composition and the voltammetric scan rate the same, the double-layer capacitance remains more or less constant in the double-layer region: the contribution of capacitive charging (the non-faradaic charging current) to the overall current is easily subtracted by a baseline shift. Switching transients generated at changes in scan direction do not influence the important portions of the cyclic voltammogram and are ignored in measuring and subtracting charging current. These transients are unavoidable artifacts due to cell time constant and finite electronic amplifier and/or filter response time.

3.3.2   *Electrode Characterization.*

Ferrocenemethanol was selected for its reversible electron transfer characteristics and for its well-documented diffusion coefficient. The latest estimate of heterogeneous electron charge transfer rate of ferrocenemethanol (abbreviated as FcMeOH or FcCH$_2$OH) from literature [45] is 0.2 cm s^{-1}, with a diffusion coefficient of 6.7×10^{-6} cm^2 s^{-1} in phosphate buffer (ionic strength 0.187 M, pH 6.75), and transfer coefficient $\alpha\approx0.5$

(temperature was 25 °C). [46, 47] Using a polished gold macro electrode (radius = 1 mm),

cyclic voltammograms were taken in 2000 μl of 0.1 M sodium phosphate buffer, against

a 3.0 M NaCl Ag/AgCl reference electrode. Then, 200 μl of 300 μM FcCH$_2$OH was

added and the CV was taken again. Due to the limited solubility of FcCH$_2$OH in

aqueous solution, concentrations of 300 μM and lower were used to prevent

precipitation. Because of the low concentration, the charging current is comparable to

the redox current, but is reproducible. Figure 3.4 shows the typical cyclic

voltammogram, taken in static solution at 25 °C. The background non-faradaic current

in buffer was subtracted from the raw voltammogram. The result is shown in Figure

3.5. The formal potential E^0 of ferrocenemethanol in 0.1M Na phosphate buffer was

found to be 0.216 V versus Ag/AgCl, which agrees with the literature value.[48]

For the gold microelectrode, the background current in buffer was similarly subtracted

from each voltammogram, and one such background corrected CV is shown in Figure

3.7. The CV extends to negative potentials against the Ag/AgCl reference, and here it

was observed that the FcCH$_2$OH solution shows increased oxygen reduction current

compared to that in buffer alone. This points to the possibility that adsorption of

FcCH$_2$OH or its oxidized couple FcCH$_2$OH$^+$ on the gold electrode catalyzes oxygen

reduction. However, above 0.03 V (vs. Ag/AgCl), no reduction of oxygen was observed.

In an inlaid disk electrode, the metal disk is flush to the insulator surrounding it, such that the insulating medium forms a continuation of the electrode plane, as shown on the left in Figure 3.6. An instantaneous change in potential step applied to the electrode while sampling current-time response (Cottrell experiment) reveals the character of mass transport of the electroactive species. At short times, the thickness of the diffusion layer that is depleted of reactant is smaller than the electrode radius leading to planar diffusion, but at long times the diffusion layer thickness becomes hemispherical and mass transport is radial in character. For a disk microelectrode, the steady-state limiting current is given by [49]

$$I_{lim} = 4nFCDr \qquad (3.1)$$

where F, n, C, D and r are Faraday's constant (96485 C mol^{-1}), number of electrons appearing in the half-reaction for the redox couple, bulk concentration (mol cm^{-3}), diffusion coefficient (cm^2 sec^{-1}) and electrode radius (cm), respectively. Using cyclic voltammetry to obtain steady-state response (resulting in a sigmoidal-shaped CV) with a microdisk electrode, certain experimental conditions must be met. For radial diffusion to dominate, the scan rate v must satisfy the condition:

$$\nu \ll \frac{RTD}{nFr^2} \tag{3.2}$$

where R and T are the ideal gas constant (8.314 J mol^{-1} K^{-1}) and absolute temperature in K, respectively. [44] The actual microfabricated electrode radius, based on calibrated microscope image measurements of several electrodes, averaged at 19 μm. Assuming an inlaid disk of that radius and using the diffusion coefficient of ferrocenemethanol 6.7×10^{-6} cm^2 s^{-1}, the right hand side of the equation suggests that the scan rate be much less than 50 mV s^{-1}. This slow scan rate is somewhat limiting for experiments where CV data should be acquired as fast as possible, but improvements can be made and will be discussed below. The shape of the voltammogram in Figure 3.7 displays a discernible diffusion peak, so it can be said that the current to the microelectrode has not quite achieved a steady state at the scan rate of 100 mV s^{-1}. The more general Randles-Sevcik equation gives the peak current for linear sweep voltammetry as a function of concentration C:

$$i_p = 0.4463(F^3/RT)^{1/2}n^{3/2}\nu^{1/2}D^{1/2}A\,C \tag{3.3}$$

In this equation, A is the electrode area (cm^2). For a microfabricated electrode with electrode areas defined by photolithography, the finite thickness of the polyimide coating over the gold metal forms a shallow recessed microdisk electrode (Figure 3.6,

right). The mass transport to a recessed electrode is more complex than to an inlaid microdisk electrode, but fortunately, there are models that describe the behavior for a recessed microdisk electrode. [50, 51] The voltammetric, rather than chronoamperometric, response of a microelectrode is also of importance to this study; it is sometimes advantageous in small volumes to recycle the redox species rather than completely convert it to the oxidized or reduced state, which is bound to occur in a small volume. Recently, cyclic voltammetry at a shallow recessed microelectrode has been investigated by Guo and Lindner, paying close attention to the transition from Cottrellian to steady-state behavior. [52] Their model for a recessed electrode requires a modification to the electrochemical response of an inlaid microdisk electrode:

$$\frac{i_{ss,recessed}}{i_{ss,inlaid}} = \frac{1}{1+1.6843L-1.3237L^2+1.7116L^3-0.7585L^4} \tag{3.4}$$

The parameter L is the ratio of recess depth to the electrode radius. For the inlaid disk where there is no recess, $L=0$. The above formula is true for a shallow recess where $0<L<1$. The above equation predicts a diminished steady-state current for the recessed electrode compared to an inlaid electrode of similar radius. The depth of the recess, determined from the 3D optical profiler image, was 7.8 μm. Consequently, the parameter L is equal to 0.41, and the right-hand side of equation 3.4 is equal to 0.64. This is a deviation from the design radius of 22.5 μm and depth of 5 μm, but as

explained in Chapter 2, there are limits to the registration accuracy of the lithographically defined polyimide overcoat. Nonetheless, a constriction of the radius is preferred over a widening, as the behavior tends toward that of a UME (ultramicroelectrode). Also, Guo and Lindner have shown that in the range of 0<L<2, the voltammetric response of a single recessed microdisk does not differ greatly from the steady-state, provided that the scan rate does not exceed a critical value, similar to Equation 3.1 above. This was done by first defining a dimensionless scan rate:

$$V = \frac{nF}{4RT} \cdot \frac{vr^2}{D} \tag{3.5}$$

For an inlaid microdisk, at a value of dimensionless scan rate $V = 0.0856$, it was found that the ratio of the maximum current in the reverse scan to the maximum current in the forward scan, γ, was equal to 0.05. The latter value was chosen as the benchmark for a sigmoidal CV shape such that $V > 0.0856$ results in a $\gamma > 0.05$, representing a deviation from steady state. For a recessed electrode, the criterion $\gamma \leq 0.05$ results in a maximum $V=0.05$ at $L=0.75$, and tapers off at either extreme (see Figure 4 of reference 52).

The optimum L is thus in the vicinity of 0.75, and this result offers a design guideline for the recessed electrode format, and is recommended for future optimization of the design. The microelectrode design radius of 22.5 µm and depth of 5 µm would have

resulted in L= 0.22, but the actual dimensions resulted in L=0.41. Either would result in a steady-state voltammetric response up to a certain scan rate, but the scan rate limit could be increased further if L could be made to equal 0.75. The optimal design and fabrication approach would then be:

1. Choose an electrode radius, in the range of 3 to 25 μm. Taking into account the narrowing of the lithographically defined features, it is reasonable to expect about a 1-3 μm reduction in radius. In general, the smaller the design radius, the larger the deviation will be.

2. Determine the thickness of the cured polyimide, and choose the appropriate HD-4100 series product for that thickness. The ratio of the *cured* insulating layer thickness and the *actual* radius should be approximately 0.75. Achieving this result requires optimization of the polyimide lithography process, as discussed in the previous chapter.

3. To obtain steady-state voltammograms, limit the dimensionless scan rate to 0.05. The actual scan rate is calculated from Equation 3.3.

Ideally, to obtain UME behavior, radii in the micron or sub-micron range are required. However, in practice, a larger radius is needed to obtain ample sensitivity to make up for very low electrode current. The low current is due to low analyte concentration, such as sub-millimolar ferrocenemethanol in this case, or the application of the microelectrode as a biosensor where enzymes immobilized on a self-assembled monolayer (SAM) are used. The latter application suffers from low enzyme coverage, despite the relatively fast enzyme kinetics. [53] Also, irregularities in electrode geometry

play an increasing role as feature sizes shrink. Finally, it cannot be stressed enough that surface impurities, such as adventitious adsorbed material or unetched overlay material, exert greater influence and become harder to clean as the electrode size shrinks. The following discussion of attempts at determining the electrode radius electrochemically underscores this difficulty.

Using equation 3.3, the slope of a plot of the anodic peak currents against the square root of various scan rates was used to obtain the electrochemical area for the reversible electrooxidation of 0.205 mM ferrocenemethanol (Figure 3.8). Using the diffusion coefficient of ferrocenemethanol, the area was calculated to be 3.51×10^{-6} cm^2. This area, compared to the theoretical geometric area of 1.13×10^{-5} cm^2, is 3.2 times smaller than expected. Taking into account the factor due to the effect of the recess (equation 3.4, which for L=0.41 amounts to 0.64), this is still half of the geometric area. It is expected that the plot of the square root of scan rate and current should be linear, but this data shows a poor correlation. This can be ascribed to the difficulty of obtaining a proper baseline at higher scan rates where the charging current exceeds the magnitude of the faradaic current.

Another way to obtain the electrode area with cyclic voltammetry is to use the same scan rate, but vary the concentration of ferrocenemethanol. In a small beaker, five

additions of 834 μl of 0.205 mM FcMeOH were made to an initial volume of 4.5 mL of 0.1 M Na phosphate buffer. The solution was stirred after each addition, and a CV was taken at 0.1 V s^{-1} in the absence of convection. Gamry's E-Chem Analyst software was used to locate the anodic peak for each CV (the 7th of 8 CV waves were used in each, and all except the first wave of every set are identical). The peaks are all within +/- 6 mV of 194 mV against the gold quasi-reference electrode. We have the option of using either the Aoki-Osteryoung expression for limiting current (equation 3.1) or the Randles-Sevcik equation (equation 3.3), in conjunction with the correction factor for the recess (Guo-Lindner model, equation 3.4) to obtain an estimate for the peak current at various concentrations at each calibration point (taking into account the total volume). Figure 3.9 shows a plot of peak current versus concentration of the experimental data as well as the prediction of the two models. The model using the limiting current overestimates the experimental currents by a factor of 2.9, while the combination of Randles-Sevcik and the Guo-Lindner model gives a better estimate of the experimental slope, only 12.5% less than the theoretical value. It is apparent that at the scan rate of 0.1V s^{-1}, steady state is not achieved. Also, the lower than expected slope of the combined model implies that the electrode has a smaller active area than the geometric area. Such reduction in area may be attributed to surface contamination. One of the difficulties in using a microelectrode is keeping the surface free of adventitious material. Normally, careful polishing is done to renew the electrode surface. But in this planar

electrode format, polishing is not possible without abrading the polyimide layer. There may also be remnants of the titanium adhesion layer not removed by Ti etchant, in which case passivation of the electrode over these areas typical of Ti is expected. The Ti etchant used was found to affect the polyimide with prolonged immersion, so, the required time based on the Ti layer thickness and etch rate was calculated to avoid over-immersion. Ultrasonication was done while etching to ensure that the etchant liquid reaches the bottom of the recess. However, despite these measures, some Ti may still remain. The Pourbaix diagram for Ti (Figure 3.10, top) shows that TiO_2 forms in the region of neutral pH at potentials -0.6 to 1.0 V vs SHE (-0.8 to 0.8 vs Ag/AgCl). To completely remove the titanium, keeping electrode potential while soaked in acid (pH=2) down to -0.5 vs SHE (-0.7 vs Ag/AgCl) should oxidize Ti to soluble Ti^{2+}, which should be carried away from the electrode by stirring. In the Pourbaix diagram for Au (Figure 3.10, bottom) in the same region, gold is stable and does not corrode.

3.3.3 *Drop shape, volume and surface area and evaporation.*

The levitated drop acquires the approximate steady-state shape of an oblate spheroid from the balance between the acoustic, gravitational, capillary, and hydrostatic forces acting on it. [54] In effect, the acoustic pressure "flattens" the unperturbed sphere that a drop would normally assume in the absence of acoustic forces. The oblate spheroid is a rotationally symmetric ellipsoid having a polar axis shorter than the equatorial axis.

Defining the equatorial radius a and polar radius c, the volume of such a spheroid, is given by:

$$V_{os} = \frac{4}{3}\pi a^2 c \qquad (3.6)$$

By obtaining the lengths of the polar and equatorial axis from the camera images, the volume of the drop may be calculated from the formula above. The aspect ratio as defined in Yarin, et al. [54] is the ratio of equatorial to polar lengths. The surface area of an oblate spheroid is:

$$S_{os} = 2\pi a^2 \left(1 + \frac{c/a}{\sqrt{(a/c)^2-1}} arcsinh\sqrt{(a/c)^2 - 1}\right) \qquad (3.7)$$

Because the evaporation of a liquid is mainly controlled by diffusion of vapor from its surface, the surface area is relevant to the rate of evaporation of the levitated drop. The evaporation of a drop of volatile liquid in still air, expressed as a change of surface area with time, is given by [55]

$$\frac{dS}{dt} = \frac{8\pi DM}{R\rho}\left(\frac{P_\infty}{T_\infty} - \frac{P_d}{T_d}\right) \qquad (3.8)$$

where M is the gram molecular weight of the liquid, D is the vapor diffusivity in the surrounding gas of the liquid species, ρ is the density of the liquid, and P and T are the saturation vapor pressure and temperature. The subscripts d and ∞ specify values at the

drop surface and in the gas well away from the drop. If the liquid and vapor attain

equilibrium, the equation above suggests that the rate is constant, such that a plot of

surface area and time is linear. The surface area of a sphere $S = 4\pi r^2$ is contained in the

above expression. This has been experimentally shown for spherical levitated drops, [55]

and seems to hold true even for spheroidal drops in an acoustic field, as our data,

shown in Figure 3.11, suggest. Tian and Apfel [56] use a model that shows a linear

decrease of drop diameter *squared* over time. This would be strictly true of a spherical

drop, as the surface area is a function of the square of the radius.   The inset in Figure

3.11 shows the evolution of the equatorial and polar diameter with time, and it can be

seen that while equatorial diameter decreases with a linear trend, the change in polar

diameter is nonlinear. From the data in Figure 3.11, the change of surface area with

evaporation of the drop levitating about the electrode can be obtained, which in this

case is -1.74×10^{-2} mm^2 sec^{-1} (r^2=0.9987) under the conditions of relative humidity RH =

52.1%, air temperature T = 23.5°C, and atmospheric pressure P = 986.3 mbar.

In an intense sound field, acoustic streaming can be generated and the resulting

convection contributes to evaporation. The exact delineation of "intense" is dependent

on many factors, but, for water, it seems that a sound pressure level (SPL) >165 dB is

intense enough to cause a deviation from the theoretical evaporation rate. [57] Tian and

Apfel have stated that below 150 dB SPL, for ethanol droplets, the acoustic field offers

no perturbation to the droplet evaporation process. [56] Since we used the minimum

power required for levitation, and maintained this power constant throughout the experiment, we simply assume either an insignificant or a small constant contribution of acoustic streaming to evaporation.

The rate of evaporation is critical to accurate determination of drop volume, and thus analyte concentration. While the surface area loss is linear, the same cannot be said for volume. Figure 3.12 shows a plot of drop volume against time from the same experiment shown in Figure 4. The volume was calculated from the equatorial and polar axes obtained from the camera images, using the spheroid formula. The parameters obtained from modeling volume loss using linear and quadratic fits are tabulated in Table 3.1. These parameters were used in the succeeding experiments to correct analyte concentration for evaporation, which will be discussed next.

3.3.4 *Cyclic Voltammetry of Pendant Versus Levitated Drop.*

Figure 3.13 shows one complete cycle of a voltammogram of the pendant and levitating drop containing 0.098 mM ferrocenemethanol in 0.1M sodium phosphate buffer. The background voltammograms made in buffer alone over the same potential range and scan rate are also superimposed on the graph. The CV of the levitated drop exhibits oscillations in the signal that are absent in the pendant drop: these may be ascribed to the motion of the drop. Figure 3.14 shows the anodic wave of a baseline-corrected voltammograms of the pendant and levitating drop containing 0.098 mM

ferrocenemethanol in 0.1 M sodium phosphate buffer. The steady-state currents are calculated from such baseline corrected anodic voltammograms. Using a model for evaporation under the conditions of the experiment, the steady-state currents are corrected for the increased concentration brought about by evaporation, allowing the calculation of valid enhancement factors. Table 3.2 summarizes the data for 3 determinations of steady-state currents for levitating and pendant drops. On average, 16% enhancement in steady-state current occurs in the levitating condition.

3.3.5   *Acoustic Streaming Effects.*

Here, an attempt at describing the source of the enhanced diffusion-limited current will be made. However, some history of electrochemistry in the presence of ultrasound is required first. Early investigations into voltammetry coupled with ultrasound (sonovoltammetry) theorized that in the presence of ultrasound, the effect of cavitation in solution was to promote mixing in the solution adjacent to the electrode so that the diffusion layer becomes truncated. [58-61] A comparison between hydrodynamic voltammetry and sonovoltammetry has been made, demonstrating 10^2-10^3 higher transport rates for ultrasound than hydrodynamic methods. [61] It is interesting to note that the limiting velocity using a rotating disk electrode (RDE), given by $U_0 = \lim_{y \to \infty} -0.8847(\omega \nu)^{1/2}$ where ω and ν are the angular velocity and kinematic viscosity, respectively, is around 9 cm s^{-1} in water for an angular velocity of 10^4 radians s^{-1}. More

recently, the hydrodynamic flow to the electrode due to pressure waves from an ultrasound source was approximated as an axisymmetric wall jet, where the limiting current i_{lim} is related to the axial velocity by: $-i_{lim} = k(U_y)^b$, where k is a constant, U_y is the axial velocity of the fluid and $b \approx 0.5$ [62]. Stefan, et al.,[6] have provided an analysis of the limiting current in relation to fluid mechanical behavior, and also acoustic power. In this case, a plot of limiting current versus acoustic power $P^{3/8}$ gave a straight line. Henley, et al. [63] found a linear plot of limiting current with acoustic power $P^{1/2}$.

However, all of these studies involved relatively high acoustic powers where the ultrasonic horn and electrode are both immersed in the same liquid, which is subject to cavitation as a result. Also, the applied ultrasound powers used in the above studies are on the order of 50 W cm^{-2}, with axial flow velocities up to 14 cm s^{-1}. [6, 63, 64] In the LDR, the electrical power (42.6 volts peak-to-peak into 300 ohms, phase angle of 0.96 rad) fed to the resonator is on the order of 10 watts, and because of losses and low acoustic power transfer from the aluminum resonator to air and then to the drop [3], the acoustic power in the resonant cavity and thus in the drop is estimated to be even lower. It is also estimated that the velocities do not exceed 1 cm s^{-1}, measured for 4.6 mm diameter water drops under acoustic levitation. [9] Instead of cavitation, streaming flows in the standing waves induce internal flows in the drop. [7, 65] Theory predicts that for water, the liquid motion inside the drop consists of two toroidal vortices for drops of radii < 12

mm,[7] which has been experimentally verified through particle image velocimetry

(PIV).[9] Furthermore, modulation of the ultrasound pressure gives rise to very rich drop

dynamics[66] that can be used for enhancing convection and accelerating mixing in the

drop.

3.3.6 *Dropwise Addition of Analyte.*

The chronoamperometric experiment was meant to demonstrate the utility of a

levitated drop reactor where continuous monitoring of an analyte occurs simultaneous

with additions of reactants. In this simple model system, ferrocyanide concentration

was monitored through chronoamperometry by the electrode piercing the drop. The

acoustic streaming enhances mixing. Although spontaneous mixing requires times on

the order of several seconds to reach steady state, we are currently investigating

methods to obtain even faster mixing. In these experiments, humidity was not

controlled. Temperature and humidity were, typically, 25°C and 50%. Drop

evaporation increases concentration. To allow compensation for this effect, we collected

evaporation data in separate experiments. Using the evaporation data, current was, as

expected, linearly proportion to concentration for at least the first 5 minutes after drop

formation. Correction of volume, knowing the initial volume and elapsed time, allows

the calculation of instantaneous concentration. The IBF system, originally designed to

spot MALDI targets, was adapted for use in adding 185 nl droplets to a levitated drop,

but the droplet velocity at impact must be controlled. With too much velocity, we have

observed the incoming droplet knocking the target drop off the electrode, and also

spattering drops, prematurely ending the experiment. We have found that a -1200 V

pulse of 100 milliseconds is sufficient to eject a 185 nl droplet while avoiding those

undesired outcomes. It was observed that the high voltage pulse from the droplet

launcher caused a negative-going excursion in the chronoamperogram, which recovers

over a period of 20 seconds. In cases where the ballistic drop missed the electrode

(confirmed by reviewing the images taken by the camera), the current recovered to a

new, higher value due to increased concentration through evaporation. Figure 3.15

shows one such chronoamperogram featuring ballistic addition of analyte to the

levitated drop. A series of three chronoamperograms, with three or four successful

droplet additions, and no lost volume, was obtained. The data was then corrected for

drop evaporation beginning from the time of introduction of the drop. Using a linear

model with V_0 as the initial volume and k as the rate of evaporation, the loss of volume

with time t is:

$$V_t = V_0 - kt \tag{3.9}$$

The volume added by the nth ballistic drop of volume V_b at time t is:

$$V_{n,t} = V_t + nV_b \tag{3.10}$$

From the known concentration of ferrocyanide in the ballistic drop C_b, the accumulated

concentration of ferrocyanide in the levitated drop at each successful addition n was

calculated as:

$$[Fe(CN)_6^{+4}]_n = (nC_bV_b)/V_{n,\text{t}} \qquad (3.11)$$

Figure 3.16 shows the results of three separate chronoamperometric experiments, with

each point equivalent to successful addition of 185-nl volume of 50 mM ferrocyanide

toward a levitating drop of 2.85 μl initial volume. It can be seen that there is a linear

correlation with droplet additions, and fair reproducibility between experiments.

3.4 Conclusions

Characterization of microfabricated recessed microdisk type electrodes made with

photodefinable polyimide insulating areas show that it is possible to determine the

electrode area by performing cyclic voltammetry utilizing a redox species with a known

concentration and diffusion coefficient. There is a significant deviation between the

designed features and those realized by lithography and microfabrication, so it is

important that accurate tools for measurement of electrode radii and recess depth be

available. The Randles-Sevcik peak current modified by the recessed microdisk theory

of Guo and Lindner gives satisfactory results even though steady-state voltammograms

are not fully achieved. However, that model does not take into account the close

proximity of the counter- and reference electrodes to the working electrode in the

present microelectrode design, a feature not common in modeling electrode behavior. Cyclic voltammetry in a 2-microliter drop suspended by acoustic levitation has been demonstrated, and the results compared with voltammetry in unstirred solution and in pendant drops. In the case of the electrode inside the levitated drop, the diffusion sphere runs into the counter-electrode, the reference electrode, and the wall of the drop so that "semi-infinite" diffusion doesn't hold true. [67] In addition, there is a circulation due to the ultrasonic field that has not yet been completely characterized, so that diffusion alone is transport-limiting only to a finite, but not yet well-understood, distance. Thus, any model developed for quiescent solution cannot adequately describe the mass transfer in our system. Cyclic voltammetry in the levitated drop shows that increased convection on the order of 16% occurs in a levitated drop at the conditions used. Drop evaporation complicates experiments that last for more than a minute, but with appropriate evaporation models, accurate correction for drop volume can be made.

3.5   References

1. Priego-Capote, F.; Luque de Castro, M. D., Analytical uses of ultrasound II. Detectors and detection techniques. *TrAC, Trends Anal. Chem.* **2004,** *23,* 829-838.

2. Westphall, M. S.; Jorabchi, K.; Smith, L. M., Mass Spectrometry of Acoustically Levitated Droplets. *Anal. Chem.* **2008,** *80,* 5847-5853.

3. Field, C. R.; Scheeline, A., Design and implementation of an efficient acoustically levitated drop reactor for in stillo measurements. *Rev. Sci. Instrum.* **2007,** *78,* 125102.

4. Marken, F.; Kumbhat, S.; Sanders, G. H. W.; Compton, R. G., Voltammetry in the presence of ultrasound: surface and solution processes in the sonovoltammetric reduction of nitrobenzene at glassy carbon and gold electrodes. *J. Electroanal. Chem.* **1996,** *414,* 95-105.

5. Saterlay, A. J.; Compton, R. G., Sonoelectroanalysis--an overview. *Fresenius J. Anal. Chem.* **2000,** *367,* 308-313.

6. Stefan, I. C.; Greber, I.; Zanelli, C. I.; Scherson, D. A., Electrochemical Applications of Acoustic Streaming Generated by a Focused Ultrasonic Source. *Isr. J. Chem.* **2008,** *48,* 197-201.

7. Zhao, H.; Sadhal, S. S.; Trinh, E. H., Internal circulation in a drop in an acoustic field. *J. Acoust. Soc. Am.* **1999,** *106,* 3289-3295.

8. Abe, Y.; Yamamoto, Y.; Hyuga, D.; Aoki, K.; Fujiwara, A., Interfacial stability and internal flow of a levitated droplet. *Microgravity Sci. Technol.* **2007,** *19,* 33-34.

9. Yamamoto, Y.; Abe, Y.; Fujiwara, A.; Hasegawa, K.; Aoki, K., Internal Flow of Acoustically Levitated Droplet. *Microgravity Sci. Technol.* **2008,** *20,* 277-280.

10. Suzuki, H., Advances in the Microfabrication of Electrochemical Sensors and Systems. *Electroanalysis* **2000,** *12,* 703-715.

11. Wang, J., Electrochemical detection for microscale analytical systems: a review. *Talanta* **2002,** *56,* 223-231.

12. Prakash, S.; Yeom, J.; Jin, N.; Adesida, I.; Shannon, M., Characterization of ionic transport at the nanoscale. *Proceedings of the Institution of Mechanical Engineers, Part N: Journal of Nanoengineering and Nanosystems* **2006,** *220,* 45-52.

13. Cooper, J. A.; Compton, R. G., Channel Electrodes — A Review. *Electroanalysis* **1998,** *10,* 141-155.

14. Menshykau, D.; O'Mahony, A. M.; del Campo, F. J.; Munõz, F. X.; Compton, R. G., Microarrays of Ring-Recessed Disk Electrodes in Transient Generator-Collector Mode: Theory and Experiment. *Anal. Chem.* **2009,** *81,* 9372-9382.

15. Wanunu, M.; Vaskevich, A.; Rubinstein, I., Widely-Applicable Gold Substrate for the Study of Ultrathin Overlayers. *J. Am. Chem. Soc.* **2004,** *126,* 5569-5576.

16. Love, J. C.; Estroff, L. A.; Kriebel, J. K.; Nuzzo, R. G.; Whitesides, G. M., Self-Assembled Monolayers of Thiolates on Metals as a Form of Nanotechnology. *Chem. Rev.* **2005,** *105,* 1103-1169.

17. Pierre, Z. N.; Field, C. R.; Scheeline, A., Sample Handling and Chemical Kinetics in an Acoustically Levitated Drop Microreactor. *Anal. Chem.* **2009,** *81,* 8496-8502.

18. Wang, J.; Tian, B.; Sahlin, E., Integrated Electrophoresis Chips/Amperometric Detection with Sputtered Gold Working Electrodes. *Anal. Chem.* **1999,** *71,* 3901-3904.

19. Martin, R. S.; Gawron, A. J.; Lunte, S. M.; Henry, C. S., Dual-Electrode Electrochemical Detection for Poly(dimethylsiloxane)-Fabricated Capillary Electrophoresis Microchips. *Anal. Chem.* **2000,** *72,* 3196-3202.

20. Wang, J., Electrochemical detection for microscale analytical systems: a review. *Talanta* **2002,** *56,* 223-231.

21. Cheng, J.; Jandik, P.; Avdalovic, N., Development and Characterization of Microfabricated Disposable Gold Working Electrodes for High-Performance Ion Chromatography and Integrated Pulsed Amperometric Detection. *Anal. Chem.* **2003,** *75,* 572-579.

22. Nuzzo, R. G.; Allara, D. L., Adsorption of bifunctional organic disulfides on gold surfaces. *J. Am. Chem. Soc.* **1983,** *105,* 4481-4483.

23. Nuzzo, R. G.; Zegarski, B. R.; Dubois, L. H., Fundamental studies of the chemisorption of organosulfur compounds on gold(111). Implications for molecular self-assembly on gold surfaces. *J. Am. Chem. Soc.* **1987,** *109,* 733-740.

24. Chidsey, C. E. D.; Loiacono, D. N., Chemical functionality in self-assembled monolayers: structural and electrochemical properties. *Langmuir* **1990,** *6,* 682-691.

25. Creager, S. E.; Rowe, G. K., Competitive self-assembly and electrochemistry of some ferrocenyl-n-alkanethiol derivatives on gold. *J. Electroanal. Chem.* **1994,** *370,* 203-211.

26. Galka, M. M.; Kraatz, H., Electron transfer studies on self-assembled monolayers of helical ferrocenoyl-oligoproline-cystamine bound to gold. *ChemPhysChem* **2002,** *3,* 356-359.

27. Kraatz, H.; Bediako-Amoa, I.; Gyepi-Garbrah, S. H.; Sutherland, T. C., Electron Transfer through H-bonded Peptide Assemblies. *J Phys Chem B* **2004,** *108,* 20164-20172.

28. Murgida, D. H.; Hildebrandt, P., Disentangling interfacial redox processes of proteins by SERR spectroscopy. *Chem. Soc. Rev.* **2008,** *37,* 937-945.

29. Lötzbeyer, T.; Schuhmann, W.; Schmidt, H., Electron transfer principles in amperometric biosensors: direct electron transfer between enzymes and electrode surface. *Sensors Actuators B: Chem.* **1996,** *33,* 50-54.

30. Schuhmann, W.; Zimmermann, H.; Habermuller, K.; Laurinavicius, V., Electron-transfer pathways between redox enzymes and electrode surfaces: Reagentless biosensors based on thiol-monolayer-bound and polypyrrole-entrapped enzymes. *Faraday Discuss.* **2000,** *116,* 245-255.

31. Gaspar, S.; Zimmermann, H.; Gazaryan, I.; Csöregi, E.; Schuhmann, W., Hydrogen Peroxide Biosensors Based on Direct Electron Transfer from Plant Peroxidases Immobilized on Self-Assembled Thiol-Monolayer Modified Gold Electrodes. *Electroanalysis* **2001,** *13,* 284-288.

32. Ge, B.; Lisdat, F., Superoxide sensor based on cytochrome c immobilized on mixed-thiol SAM with a new calibration method. *Anal. Chim. Acta* **2002,** *454,* 53-64.

33. Cortina-Puig, M.; Muñoz-Berbel, X.; Calas-Blanchard, C.; Marty, J., Electrochemical characterization of a superoxide biosensor based on the co-immobilization of cytochrome c and XOD on SAM-modified gold electrodes and application to garlic samples. *Talanta* **2009,** *79,* 289-294.

34. Chen, X. J.; West, A. C.; Cropek, D. M.; Banta, S., Detection of the Superoxide Radical Anion Using Various Alkanethiol Monolayers and Immobilized Cytochrome c. *Anal. Chem.* **2008,** *80,* 9622-9629.

35. Wilson, R. C. K.; Phuong, D. T.; Chainani, E.; Scheeline, A., Flexible, micron-scaled superoxide sensor for in vivo applications. *J. Electroanal. Chem.* **2011,** *662,* 100-104.

36. Lipkowski, J.; Shi, Z.; Chen, A.; Pettinger, B.; Bilger, C., Ionic adsorption at the Au(111) electrode. *Electrochim. Acta* **1998,** *43,* 2875-2888.

37. Kolics, A.; Thomas, A. E.; Wieckowski, A., [36]Cl labelling and electrochemical study of chloride adsorption on a gold electrode from perchloric acid media. *J. Chem. Soc. , Faraday Trans.* **1996,** *92,* 3727-3736.

38. Oesch, U.; Janata, J., Electrochemical study of gold electrodes with anodic oxide films—I. Formation and reduction behaviour of anodic oxides on gold. *Electrochim. Acta* **1983,** *28,* 1237-1246.

39. Weber, M.; Nart, F. C., On the adsorption of ionic phosphate species on Au(111)—an in situ FTIR study. *Electrochim. Acta* **1996,** *41,* 653-659.

40. Niaura, G.; Gaigalas, A. K.; Vilker, V. L., Surface-Enhanced Raman Spectroscopy of Phosphate Anions: Adsorption on Silver, Gold, and Copper Electrodes. *J. Phys. Chem. B* **1997,** *101,* 9250-9262.

41. Weber, M.; de Moraes, I. R.; Motheo, A. J.; Nart, F. C., In situ vibrational spectroscopy analysis of adsorbed phosphate species on gold single crystal electrodes. *Colloids Surf. Physicochem. Eng. Aspects* **1998,** *134,* 103-111.

42. Silva, F.; Martins, A., Surface structural effects on specific adsorption of oxoanions on gold single crystal electrodes. *J. Electroanal. Chem.* **1999,** *467,* 335-341.

43. Pletcher, D.; Sotiropoulos, S., Cathodic reduction of oxygen in water and media of low ionic strength. *J. Chem. Soc. , Faraday Trans.* **1995,** *91,* 457-462.

44. Bard, A. J. ; Faulkner, L. R., *Electrochemical Methods: Fundamentals and Applications;* Wiley, 2001.

45. Sun, P.; Mirkin, M. V., Kinetics of Electron-Transfer Reactions at Nanoelectrodes. *Anal. Chem.* **2006,** *78,* 6526-6534.

46. Bourdillon, C.; Demaille, C.; Moiroux, J.; Saveant, J., Catalysis and Mass Transport in Spatially Ordered Enzyme Assemblies on Electrodes. *J. Am. Chem. Soc.* **1995,** *117,* 11499-11506.

47. Cannes, C.; Kanoufi, F.; Bard, A. J., Cyclic voltammetry and scanning electrochemical microscopy of ferrocenemethanol at monolayer and bilayer-modified gold electrodes. *J. Electroanal. Chem.* **2003,** *547,* 83-91.

48. Harper, A.; Anderson, M. R., Electrochemical Glucose Sensors—Developments Using Electrostatic Assembly and Carbon Nanotubes for Biosensor Construction. *Sensors* **2010,** *10,* 8248-8274.

49. Aoki, K.; Akimoto, K.; Tokuda, K.; Matsuda, H.; Osteryoung, J., Linear sweep voltammetry at very small stationary disk electrodes. *J. Electroanal. Chem.* **1984,** *171,* 219-230.

50. Bond, A. M.; Luscombe, D.; Oldham, K. B.; Zoski, C. G., A comparison of the chronoamperometric response at inlaid and recessed disc microelectrodes. *J. Electroanal. Chem.* **1988,** *249,* 1-14.

51. Bartlett, P. N.; Taylor, S. L., An accurate microdisc simulation model for recessed microdisc electrodes. *J. Electroanal. Chem.* **1998,** *453,* 49-60.

52. Guo, J.; Lindner, E., Cyclic voltammetry at shallow recessed microdisc electrode: Theoretical and experimental study. *J. Electroanal. Chem.* **2009,** *629,* 180-184.

53. Vertova, A.; Forlini, A.; Rondinini, S., Probing the Electron Transfer Process of Cytochrome C Embedded in Mixed Thiol SAM on Electrodeposited Gold. *J. Electrochem. Soc.* **2012,** *159,* 81-F86.

54. Yarin, A. L.; Pfaffenlehner, M.; Tropea, C., On the acoustic levitation of droplets. *J. Fluid Mech.* **1998,** *356,* 65-91.

55. Seaver, M.; Galloway, A.; Manuccia, T. J., Acoustic levitation in a free-jet wind tunnel. *Rev. Sci. Instrum.* **1989,** *60,* 3452-3459.

56. Tian, Y.; Apfel, R. E., A novel multiple drop levitator for the study of drop arrays. *J. Aerosol Sci.* **1996,** *27,* 721-737.

57. Yarin, A. L.; Brenn, G.; Kastner, O.; Rensink, D.; Tropea, C., Evaporation of acoustically levitated droplets. *J. Fluid Mech.* **1999,** *399,* 151-204.

58. Compton, R. G.; Eklund, J. C.; Page, S. D.; Mason, T. J.; Walton, D. J., Voltammetry in the presence of ultrasound: mass transport effects. *J. Appl. Electrochem.* **1996,** *26,* 775-784.

59. Compton, R. G.; Eklund, J. C.; Page, S. D.; Sanders, G. H. W.; Booth, J., Voltammetry in the Presence of Ultrasound. Sonovoltammetry and Surface Effects. *J. Phys. Chem.* **1994,** *98,* 12410-12414.

60. Marken, F.; Eklund, J. C.; Compton, R. G., Voltammetry in the presence of ultrasound: can ultrasound modify heterogeneous electron transfer kinetics? *J. Electroanal. Chem.* **1995,** *395,* 335-338.

61. Hagan, C. R. S.; Coury, L. A., Jr, Comparison of hydrodynamic voltammetry implemented by sonication to a rotating disk electrode. *Anal. Chem.* **1994,** *66,* 399-405.

62. Stefan, I. C.; Mo, Y.; Zanelli, C. I.; Scherson, D. A., Electrochemistry in the Presence of Convective Flow Generated by Acoustic Streaming from a Focused Ultrasonic Source. *Anal. Chem.* **2001,** *73,* 4384-4387.

63. Henley, I. E.; Fisher, A. C.; Compton, R. G.; Banks, C. E., Computational Electrochemistry: Finite Element Simulation of a Disk Electrode with Ultrasonic Acoustic Streaming. *J. Phys. Chem. B* **2005,** *109,* 7843-7849.

64. Compton, R. G.; Eklund, J. C.; Page, S. D., Sonovoltammetry: Heterogeneous Electron-Transfer Processes with Coupled Ultrasonically Induced Chemical Reaction. The "Sono-EC" Reaction. *J. Phys. Chem.* **1995,** *99,* 4211-4214.

65. Trinh, E. H.; Robey, J. L., Experimental study of streaming flows associated with ultrasonic levitators. *Phys. Fluids* **1994,** *6,* 3567-3579.

66. Yarin, A. L.; Weiss, D. A.; Brenn, G.; Rensink, D., Acoustically levitated drops: drop oscillation and break-up driven by ultrasound modulation. *Int. J. Multiphase Flow* **2002,** *28,* 887-910.

67. Neufeld, Z. ; Hernández-García, E., *Chemical And Biological Processes In Fluid Flows - A Dynamical Systems Approach;* Imperial College Press, 2009.

3.6   Chapter 3 Figures

Figure 3.1. Photographs of the electrode positioned in the resonant cavity. From left to right: A) Electrode without a drop, showing region of tip which is CYTOP-polymer coated. B) Electrode with pendant drop. C) Electrode with acoustically levitated drop.
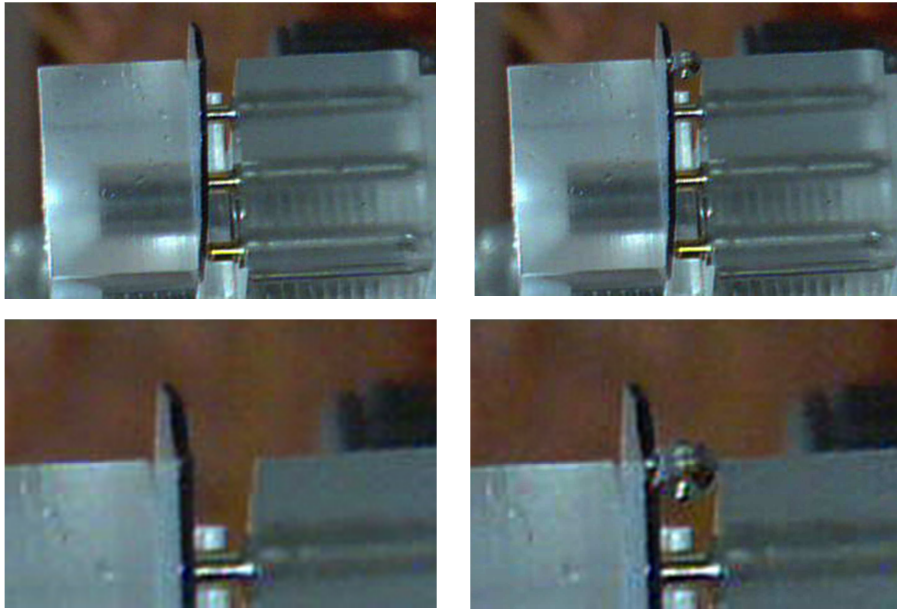
Figure 3.2. Photograph of electrode taken along the longitudinal axis (top left) showing the position of the drop during levitation (top right). Bottom pictures show enlargements of the pictures above.
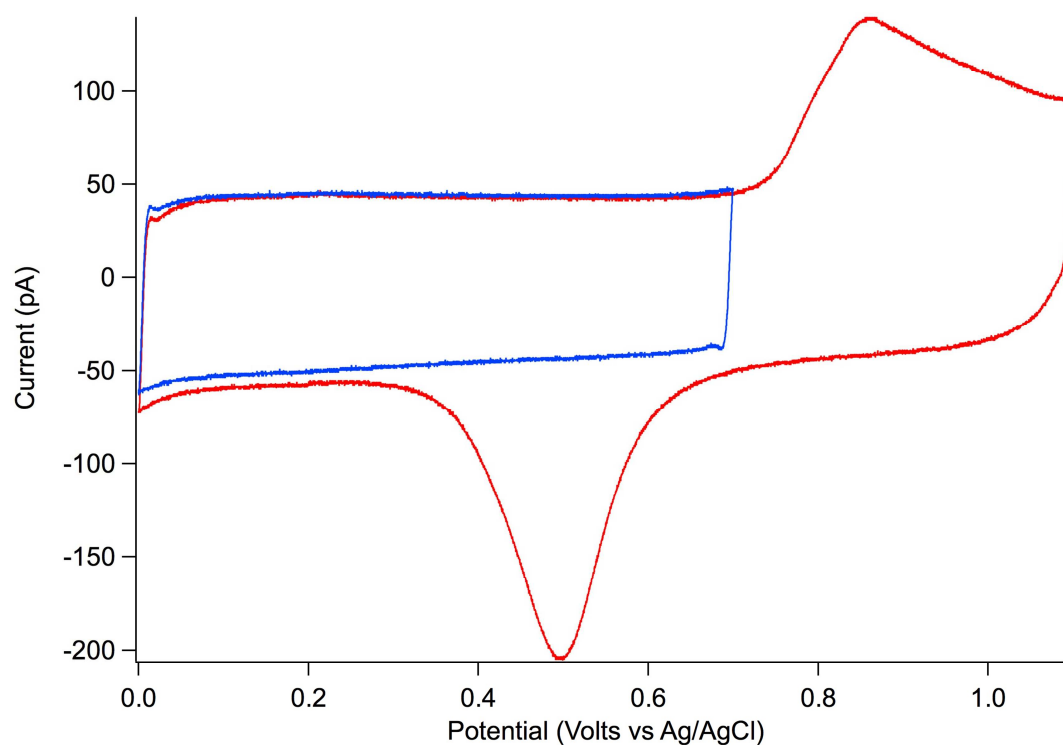
Figure 3.3. Cyclic voltammogram (microelectrode) of gold in 0.1 M sodium phosphate buffer, pH 6.75, at a scan rate of 100 mV s^{-1}. The CV from the range 0 to 1.1 V vs Ag/AgCl is in red, showing the oxide formation commencing beyond 0.7 V, and the gold reduction peak centered around 0.5 V. The CV in the double-layer region (0 to 0.7 V vs Ag/AgCl) is shown in blue.
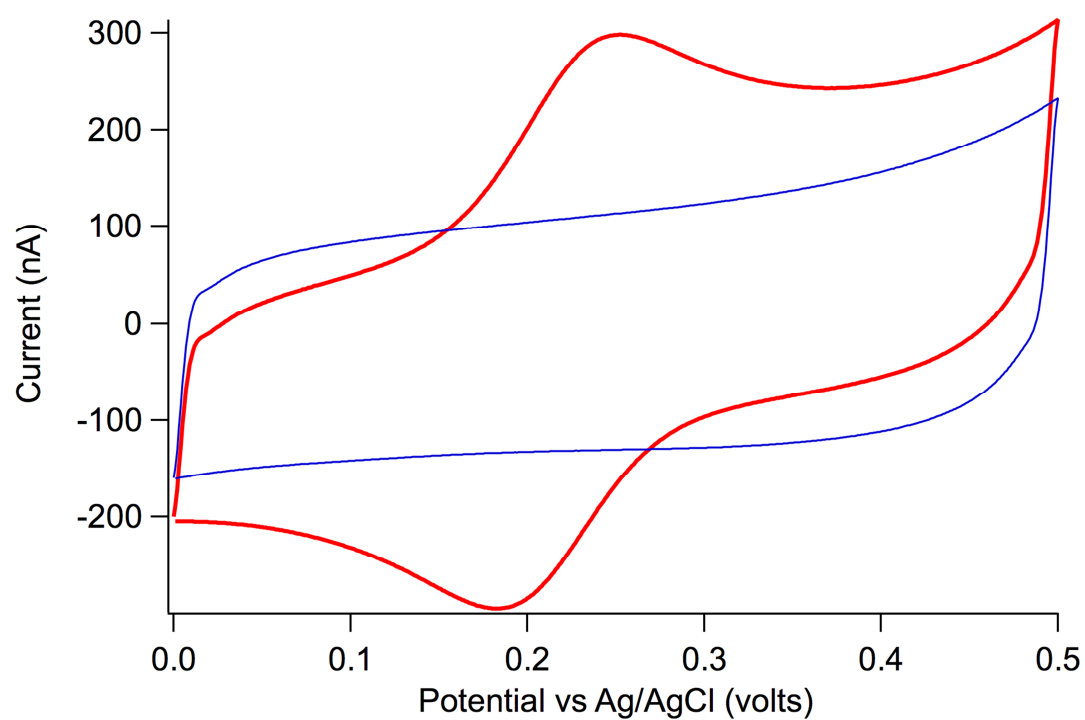
Figure 3.4. Cyclic voltammogram of 0.3 mM ferrocenemethanol (red) in 0.1 M sodium phosphate buffer taken with 1 mm radius gold electrode. Background scan is shown in blue.
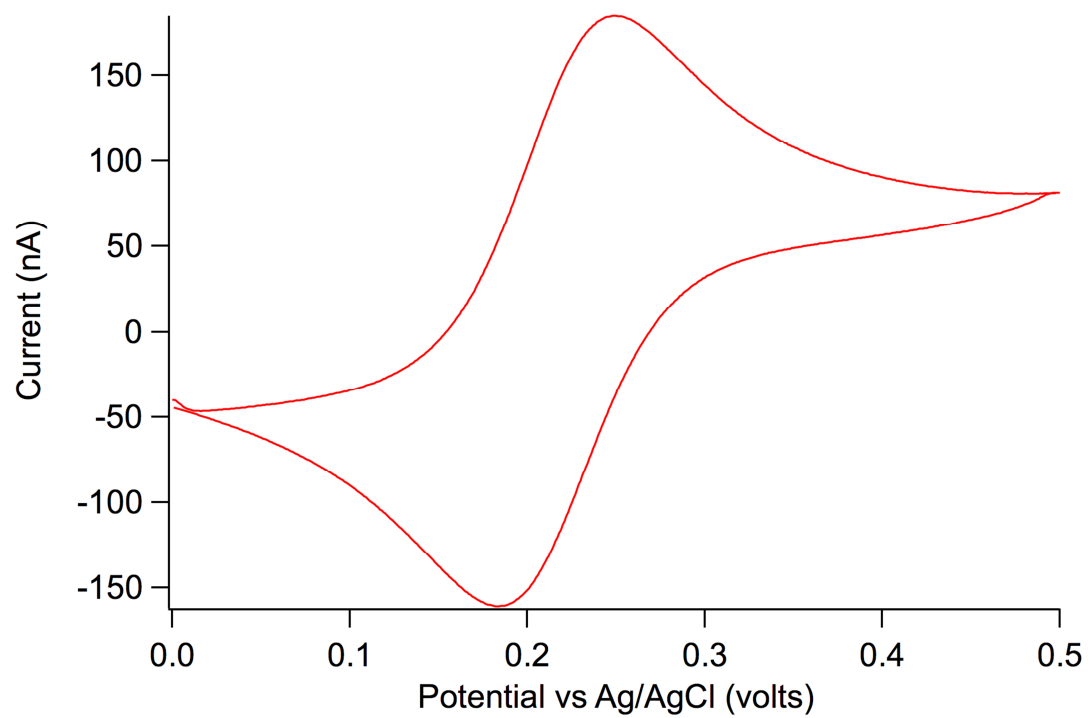
Figure 3.5. Background-subtracted CV from gold macroelectrode CVs of **Figure 3.4**.
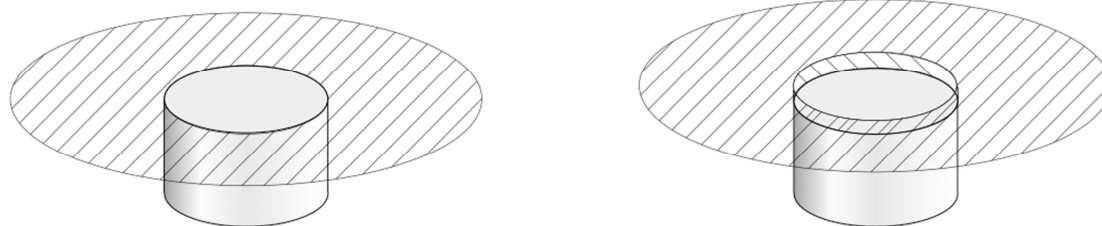
Figure 3.6. Representations of inlaid disk and recessed disk electrodes. The hatched areas constitute insulating material.
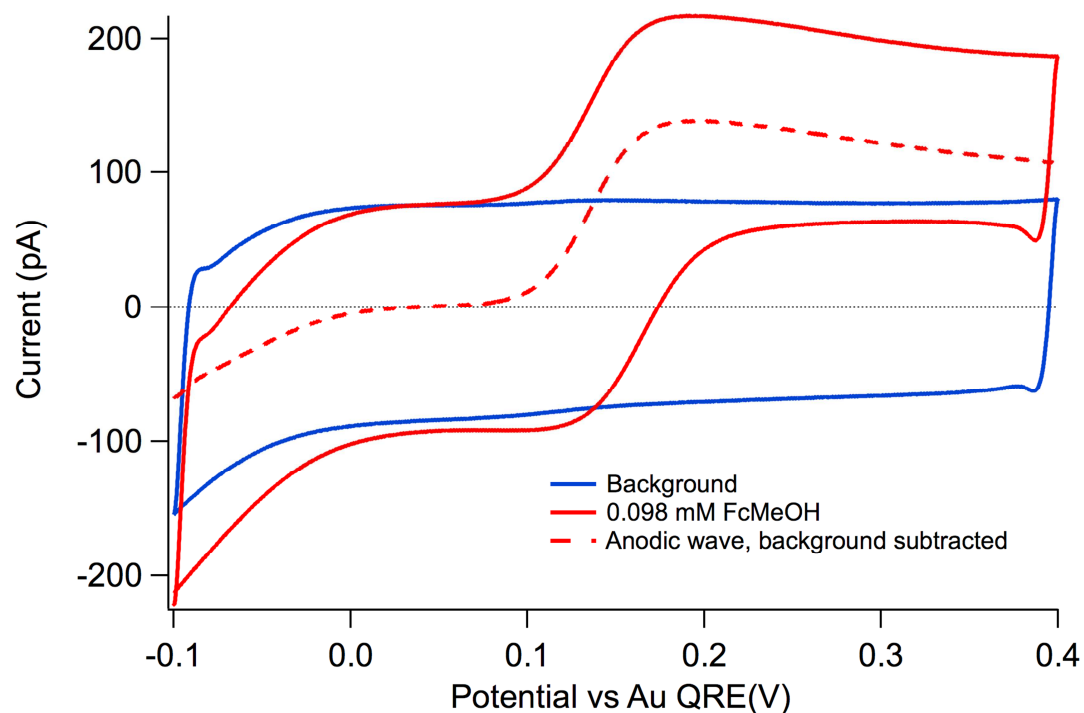
Figure 3.7. Cyclic voltammogram (microelectrode) of 0.098 mM ferrocenemethanol in unstirred (solid red line) and the background scan in 0.1 M Na phosphate buffer (solid blue line). The dotted red line corresponds to the background-subtracted anodic wave used in obtaining peak currents.
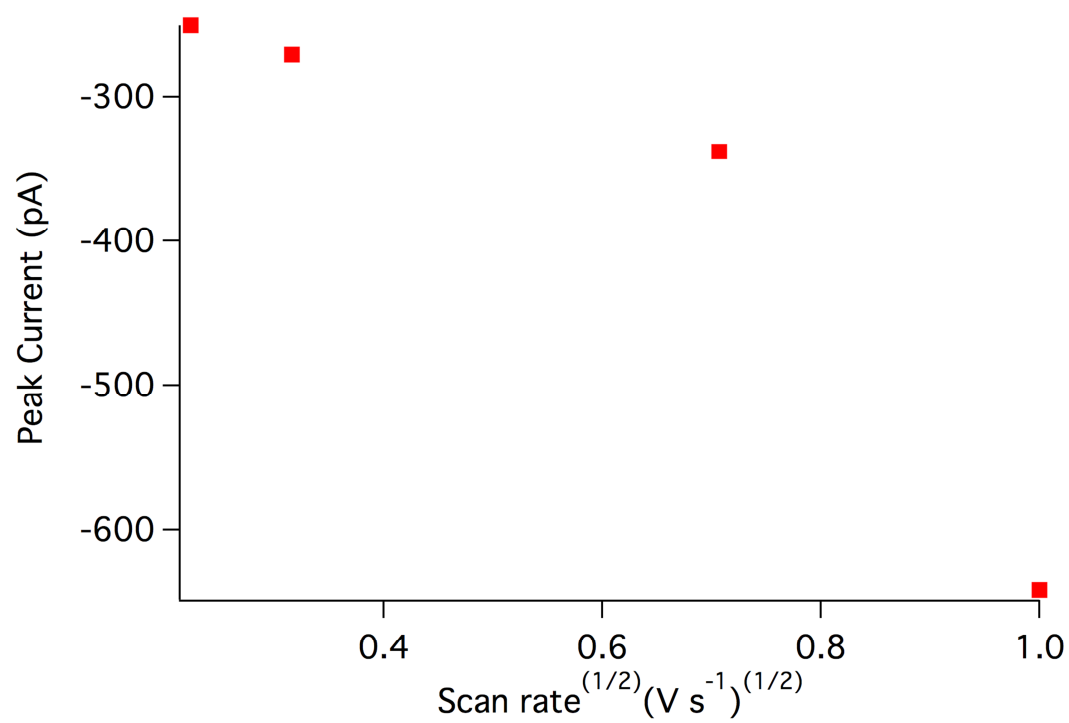
Figure 3.8. Plot of peak current versus square root of scan rate, cathodic wave of ferrocenemethanol.
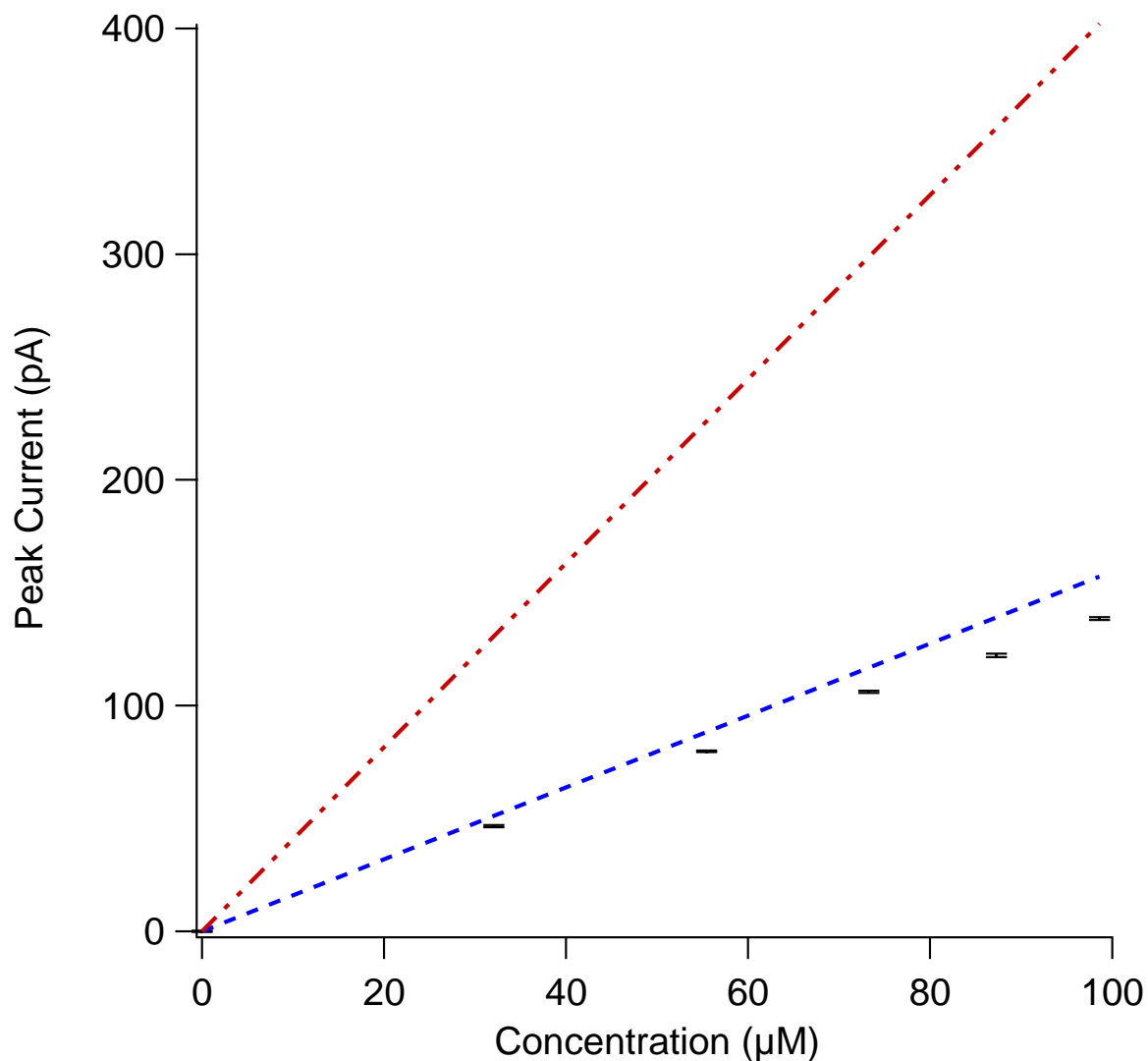
Figure 3.9. Plot of anodic peak currents against various concentrations of ferrocenemethanol. The red dotted line (−••−) is the current calculated from the steady-state model combined with the Guo-Lindner recessed disk model. The blue dotted line (− − −) represents the peak current from the Randles-Sevcik equation modified with the Guo-Lindner model using a 19-μm radius disk with a recess of 7.8 μm. The black lines are experimental data, with error bars depicting 2 SD.
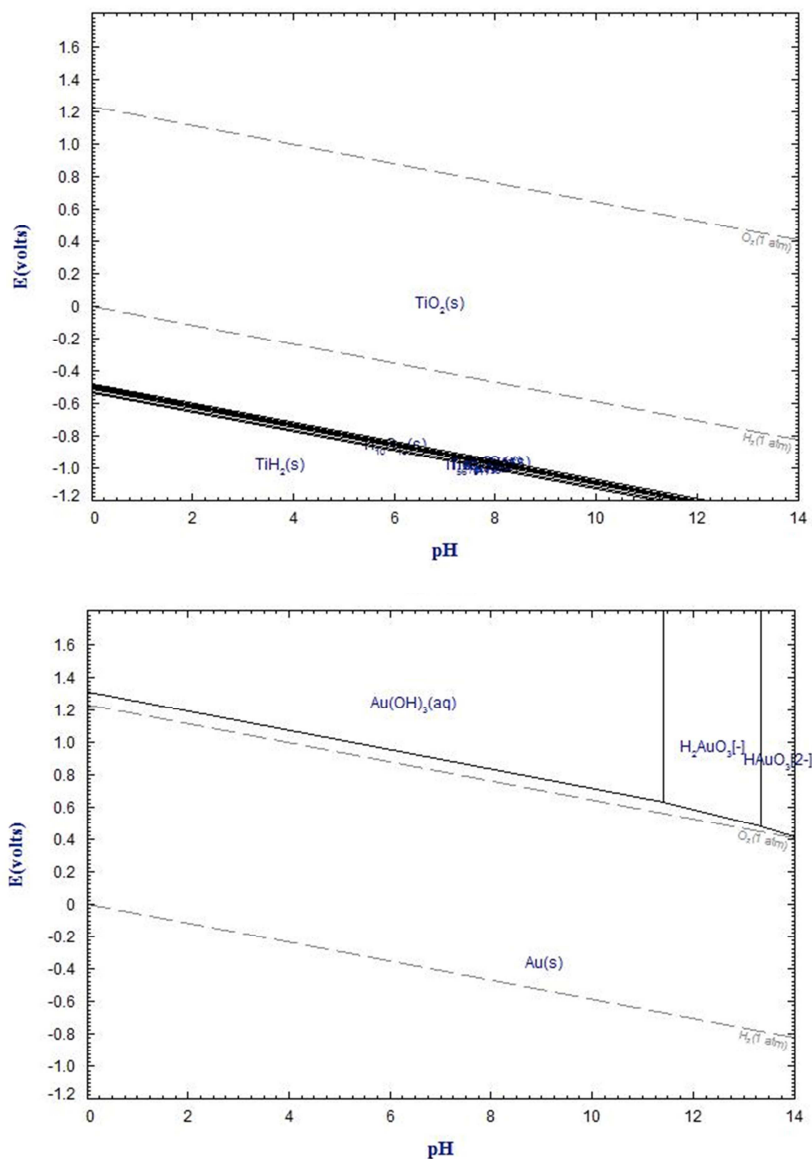
Figure 3.10. Pourbaix diagrams for titanium (top) and gold (bottom). These diagrams are reproduced with permission from the free version of the FactSage package at http://www.crct.polymtl.ca/factweb.php (Bale, C. W. and Belisle, E.).
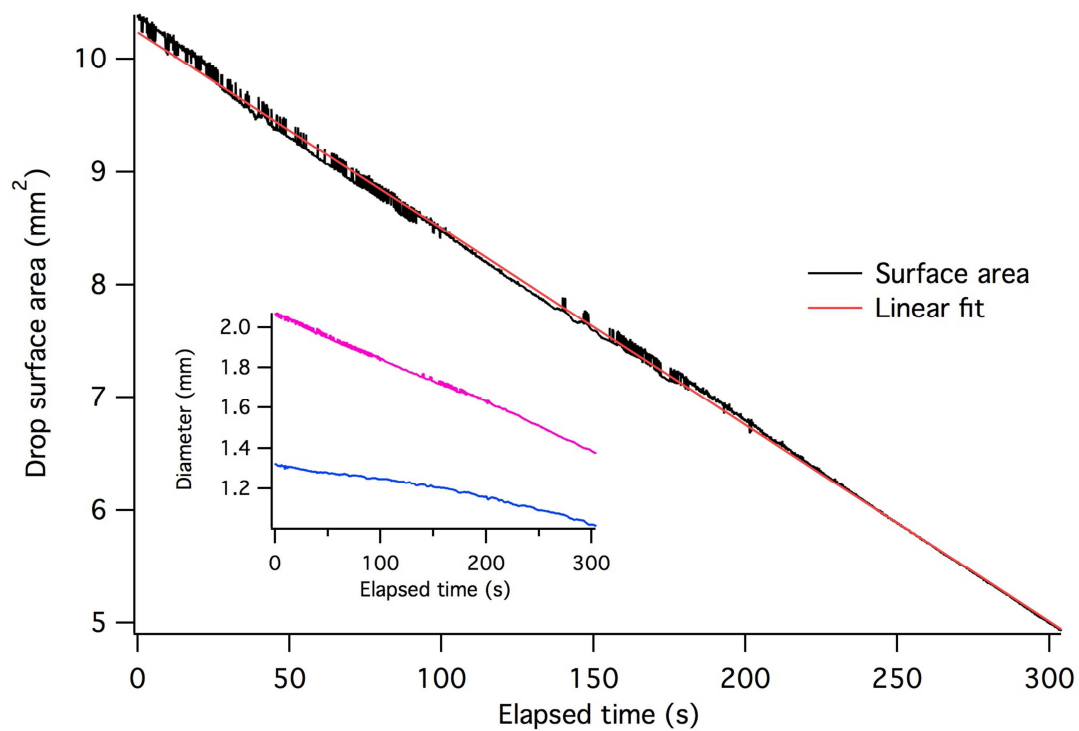
Figure 3.11. Plot of drop surface area against time. The drop is levitated on an electrode. RH = 52.1%, T = 23.5 °C, P = 986.3 mbar. The inset shows the evolution of the equatorial (magenta) and polar (blue) diameters over time.
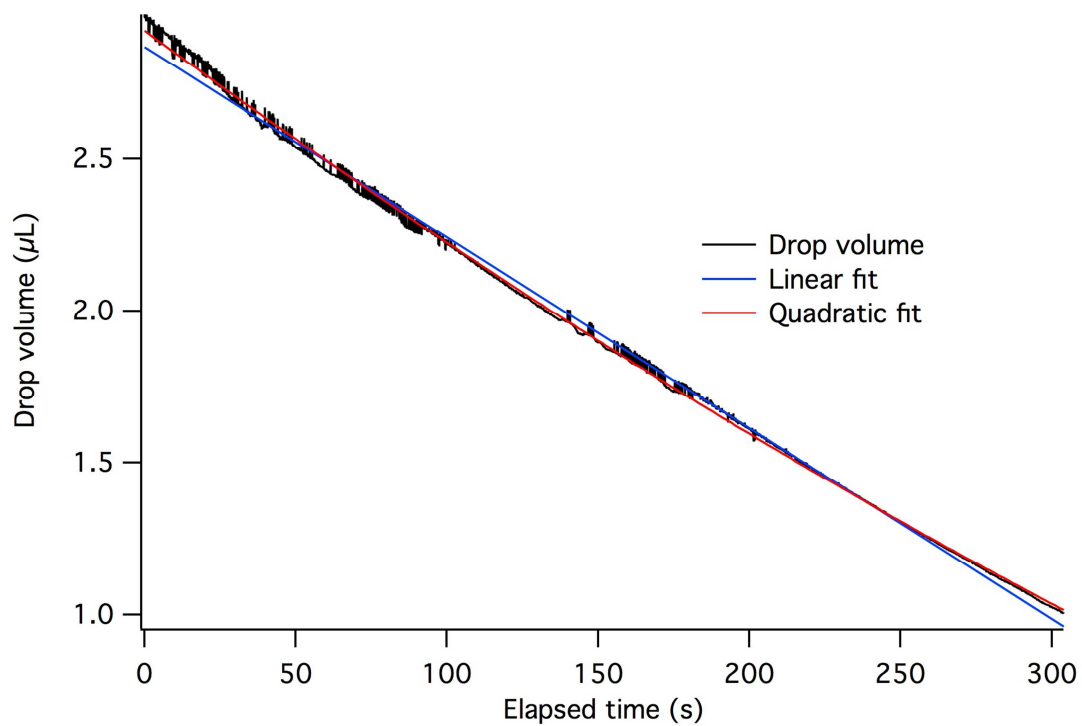
Figure 3.12. Plot of drop volume against time, with the same conditions as **Figure 3.11**. A linear (blue) and a quadratic fit (red) are superimposed over the data points (black).
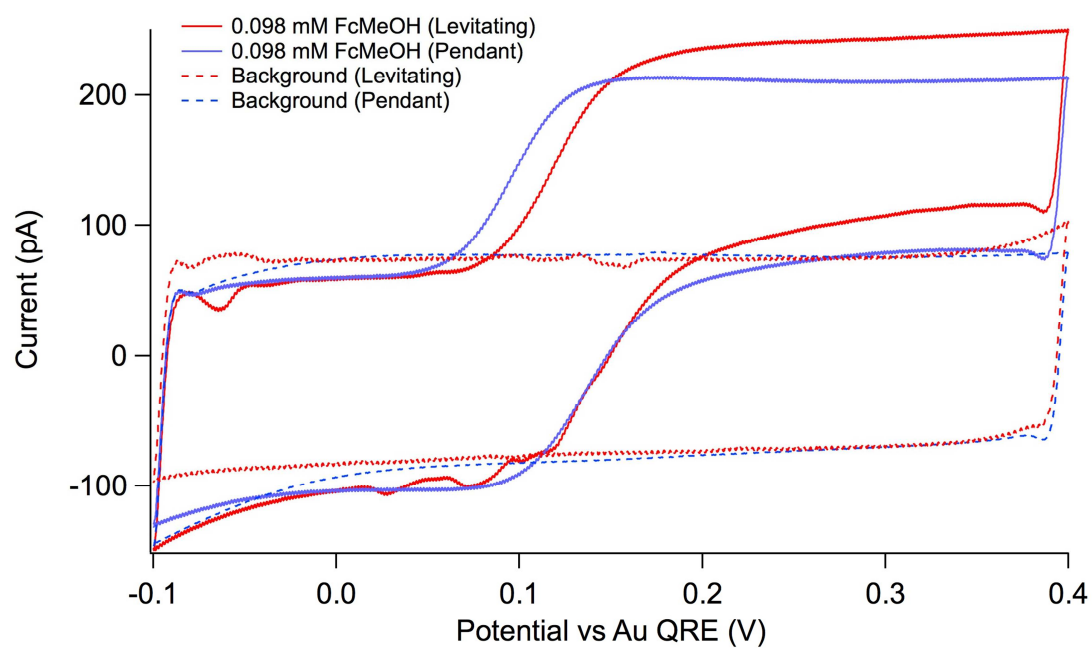
Figure 3.13. Typical voltammograms of 0.098 mM ferrocenemethanol (FcMeOH) in pendant (blue lines) and levitated (red lines) drops. The background currents are shown as dotted lines. Scan rate is 0.1 Vs^{-1}.
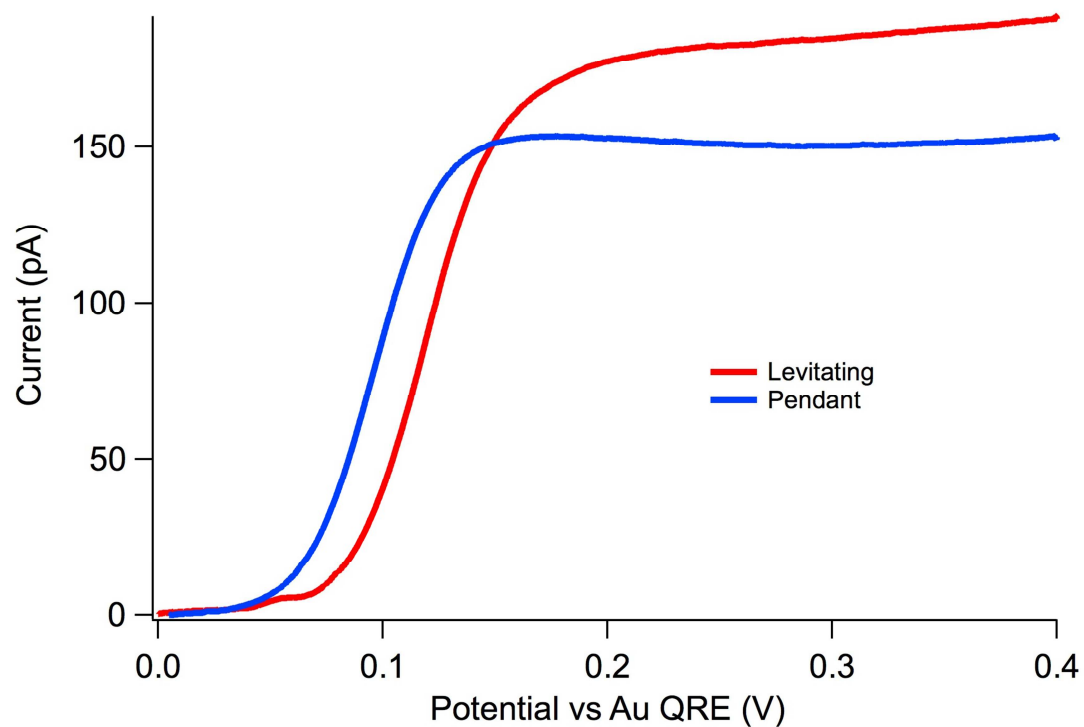
Figure 3.14. Baseline-corrected positive-going sweep of the voltammograms generated from **Figure 3.13**.
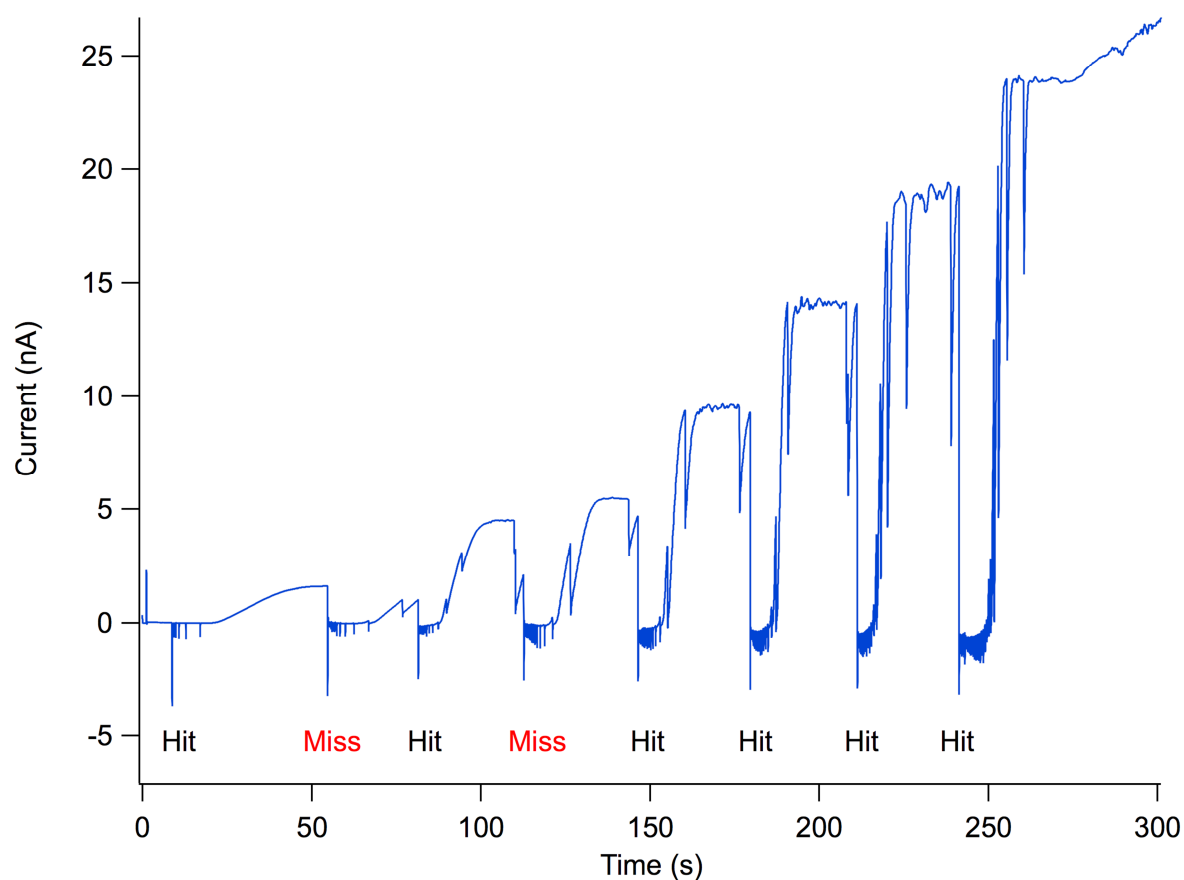
Figure 3.15. Chronoamperogram taken during ballistic additions of 185 nl droplets of 50 mM $K_4Fe(CN)_6$ toward a 2.85 µl levitated drop containing initially 0.1M sodium phosphate buffer. Negative-going excursions coincide with the pulsed high-voltage launch event. The camera aimed at the electrode is triggered by each launch, allowing review of the trajectory and recognition of successful impacts or misses, as noted below the graph.
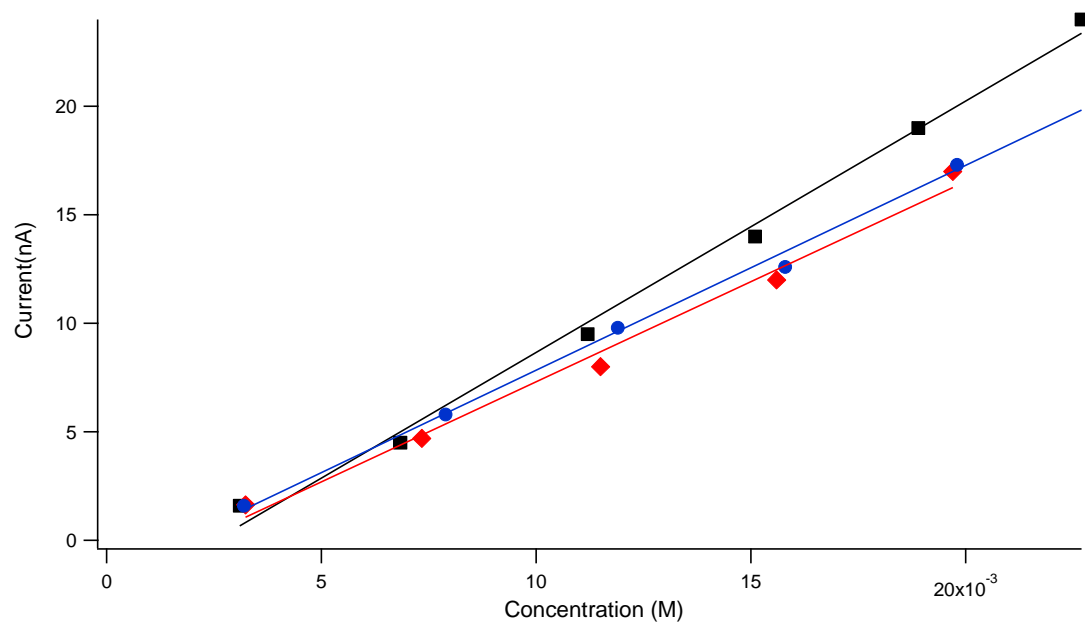
Figure 3.16. Plot of current versus concentration (corrected for evaporation) of successive additions of 185 nl of 50 mM $K_4Fe(CN)_6$ to a levitated Na-phosphate buffer drop of 2.85 µl initial volume. Data from three chronoamperograms (such as **Figure 3.15**) are shown.

3.7   Chapter 3 Tables

Table 3.1. Fit parameters for the rate of evaporation of a levitated drop positioned on the microelectrode.

Linear		Quadratic	
Parameter	*Value*	*Parameter*	*Value*
intercept (L)	2.87×10^{-6}	a_0 (L)	2.93×10^{-6}
slope (L s^{-1})	-6.28×10^{-9}	a_1 (L s^{-1})	-7.34×10^{-9}
		a_2 (L s^{-2})	3.47×10^{-12}

Table 3.2. Data for three sets of cyclic voltammetry experiments of levitated and pendant drops containing 0.098 mM ferrocenemethanol in 0.1 M sodium phosphate buffer.

Trial	Condition	I_P (pA)	Elapsed time (s)	Concentration change	Enhancement
1	Levitating	183.1	76	1.04	1.17
1	Pendant	150.5	76	1.04	1.17
2	Pendant	140.0	134	1.06	1.16
2	Levitating	174.0	134	1.06	1.16
3	Levitating	180.0	79	1.04	1.15
3	Pendant	150.0	79	1.04	1.15

CHAPTER 4

FLOWING SOURCE OF SUPEROXIDE AT NEAR-BIOLOGIC PH

4.1   Introduction

Following phagocytosis of bacteria, macrophages and neutrophils deliver toxic substances inside the vacuole containing the bacteria in an attempt to kill it. These antimicrobials include superoxide ($O_2^{\bullet-}$) and nitric oxide (NO) that are produced by the host enzymes NADPH-dependent oxidase complex and nitric oxide synthetase, respectively.[1]   In neutrophils, myeloperoxidase (MPO) is also discharged into the phagosome and accounts for a quarter of the neutrophil proteins in the vacuole. MPO uses superoxide and hydrogen peroxide as substrates to form hypochlorous acid, which is strongly biocidal.[2]   Superoxide interacts with MPO in three enzymatic cycles that may influence the killing mechanism of neutrophils.[3]

The exact mechanism by which the macrophage kill pathogenic bacteria such as *Salmonella enterica* during the phagocytic oxidative burst process is still unclear. This much is known: superoxide is involved, but its exact role is uncertain. Peroxynitrite ($ONOO^-$) formed from $O_2^{\bullet-}$ and NO is irrelevant: $O_2^{\bullet-}$ and NO production are temporally separated.[4] $O_2^{\bullet-}$ cannot damage membranes in bacteria, as lipid peroxidation requires unsaturated fatty acids, nor can it damage proteins.[5] H_2O_2 from

the dismutation of $O_2{}^{\bullet-}$ is scavenged by several cytoplasmic peroxidases and catalases to prevent DNA damage. Evidence points to an extracytoplasmic target for superoxide: *Salmonella* lacking periplasmic SOD (SodCI mutants) are attenuated, yet survive *in vitro* or in NADPH oxidase-knockout mice. The damage outside the cytoplasm is by $O_2{}^{\bullet-}$ alone, and not downstream ROS, but the identity of the target is not known. Comparison SodCI mutants against wild type show that wild-type surprisingly had higher H_2O_2 entering the cytoplasm. This suggests one-electron scavenging of $O_2{}^{\bullet-}$ in the periplasm of the SodCI mutant. Identifying the target of exogenous $O_2{}^{\bullet-}$ requires a means to produce superoxide in the laboratory at concentrations approximating those produced in the phagosome. [6] It is estimated that NADPH oxidase is capable of producing $O_2{}^{\bullet-}$ of 100 μM inside the phagosome, whereas xanthine/xanthine oxidase typically used *in vitro* generates only < 1μM for a few minutes. [4, 7] Because superoxide in the anionic form cannot cross membranes, it is equally important that superoxide be delivered at neutral pH or even lower, similar to conditions in the acidified phagosome. Clearly, there is a need for a superoxide source that delivers concentrated superoxide at biologically relevant pH. This chapter describes the attempts at designing and making such a source of superoxide.

4.2   Design of apparatus

4.2.1   Version 1

The central idea was to store KO_2 at high pH where dismutation is slow, and then

quickly lower the pH by ion-exchange through a membrane/buffer system. The first

version of the superoxide delivery system (see Figure 4.1) was a microfluidic device that

featured a channel where KO_2 dissolved in 0.86 M KOH would flow. On top of the

superoxide flow channel, a thin (<10 µm), polycarbonate track etched membrane (GE-

Osmonics K01CP09030, Hopkins, MN) separates the superoxide channel from two,

counter-flow channels of carbonate and phosphate buffer. The membrane was treated

with Nafion solution (Sigma-Aldrich, St. Louis, MO) to coat the surface and fill the

pores, and then acidified in 2M HCl. This was used since commercial Nafion

membranes were only available in thicknesses of over 100 µm. The desired end result

was that the buffer flows would neutralize the base by the time it exited the device at

pH 7-8.

This device was built from acrylic blocks and ports made for Upchurch fittings. It was

discovered that the diffusion rate across the porous membrane was too slow to

neutralize the base. Slowing down the superoxide flow rate to allow more proton

diffusion would only provide more time for dismutation of superoxide, and increasing

106

the pressure on the flow of buffer in an effort to speed transport across the membrane would lead to leakage.

4.2.2   Versions 2 and 3

If the first version of the superoxide source worked as desired, it would have delivered microliter volumes and would have been mainly useful for calibration of a superoxide microsensor. As stated in the introduction, being able to produce $O_2^{\bullet-}$ in the laboratory at concentrations relevant to killing *Salmonella* in the phagosome is an unsolved problem. The goal for subsequent versions was to generate superoxide at near biological pH in order to rapidly introduce the superoxide to *Salmonella* bacteria. These bacteria are grown in medium and immobilized on filter paper by injecting the medium through a Swinnex filter holder (Millipore, Billerica, MA) containing 0.45-micron filter. Syringe pumps were then used to force a near biological pH buffer to mix with various concentrations of superoxide in 0.25M KOH in a high-pressure mixing tee, (model U-466, Upchurch Scientific, Oak Harbor, WA). Several problems occurred with this system. The rate of flow was limited to a few mL min^{-1}. Besides the low flow rates, there was too much backpressure for the syringe pumps to handle, causing the pumps to discharge at uneven rates. From this exercise, the following lessons were learned: 1) The flow rate needs to be sufficiently high to create rapid turbulent mixing between the superoxide solution and the buffer. The flow rates generated by syringe pumps in the

small diameter tubing (0.3-inch inner diameter) could never be made high enough to generate turbulence needed for efficient mixing. 2) A system with low dead volume past the point of mixing toward delivery was required, so that the superoxide would not have time to dismute once in a solution with lower pH solution than its storage pH. A re-design of the system was in order. Prof. Alex Scheeline came up with the idea of using a mixer from a stopped-flow spectrometer as the model to mix the buffer and superoxide. Prof. James Slauch suggested Robert Berger's rapid mixer [8] . Berger's flow mixer required very high rates of flow (velocities of upwards of 30 m sec^{-1}) at high pressures (upwards of 100 psi) to create turbulence in order to achieve the sub-millisecond mixing times required for kinetics studies. Highly efficient mixing at moderate flows are needed, otherwise, immense amounts of buffer would be required to sustain such high flows. A design for a mixer, based on division and recombination of flow, was found in the article detailing a stopped-flow spectrophotometer by Gibson and Milnes. [9] The syringes were replaced by larger 1-liter Nalgene polyethylene bottles that would be pressurized with nitrogen gas to produce the flow. Caps for these reservoirs with fittings for nitrogen gas pressurization as well as liquid withdrawal were machined out of Delrin (see Figure 4.2). Tubing of larger diameter was used to minimize back-pressure. The mixer "puck" based on the Gibson-Milnes design (see Figure 4.3), easily machined out of acrylic, was sandwiched between two blocks of acrylic: The inlet (top) block (Figure 4.4) had two threaded ports for fittings for the tubings of the KO_2-containing base and the buffer. These two flows were combined by

the mixer and lead to a single stream out to the bottom block, which divided the flow into four smaller streams, each leading to a threaded port to attach the Swinnex 13-mm diameter filter holder (Figure 4.5). Four separate streams each fed into a filter holder, allowed for a high total flow rate (387 mL min^{-1} at 40 psi gas pressure) while keeping the backpressure on each filter within limits. Thus, four immobilized samples of *Salmonella* could be subjected to the superoxide stream in one go. As the stream exits the mixer, there is a finite distance to the filters. The flow-rate dependent transit time to the filters defines the dead time over which dismutation of superoxide occurs. The concentration delivered to the filter units is then a function of pH after mixing, flow rate, and initial superoxide concentration. Using rate constants and flow rate data obtained by Aaron Keith[10] from trials in the flow system, theoretical concentrations of superoxide at the filters can be calculated, the results of which are shown in Table 4.1.

4.2.3   Version 4

Relative to conditions that the *Salmonella* are subjected to in the macrophage, pH 9 is quite high. To bring this down further, a more concentrated buffer is required, leading to an unrealistically high ionic strength in the mixed solution. Either situation calls into question the biological relevance of superoxide delivered at high pH and ionic strength. Also, it was observed that upon addition of KO_2 to 0.25 M KOH solutions, fizzing of the resulting solution invariably occurs, regardless of how the KO_2 powder is added to the aqueous base. Nguyen Hoai Thu (summer student from Vietnam National University,

Hanoi) obtained data that showed no spectroscopic evidence of superoxide when KO_2 was added rapidly to 0.25 M KOH. Over a period of 30 minutes after addition, the spectra displayed only features characteristic of H_2O_2 in base. This meant that the KO_2 dismuted rapidly, even in strong base, and that the calculated initial concentration of 200μM will never be reached. This is ascribed to local high concentrations of potassium superoxide at the solid/aqueous interface, and it is this high concentration that drives disproportionation in the presence of water. Many studies in the past used dissolved potassium superoxide in dry dimethyl sulfoxide (DMSO), an aprotic organic solvent, to make stable KO_2 solutions. [11, 12] A small amount of crown ether may be added to enhance solubility in DMSO. Kept away from heat and moisture, the KO_2 is stable in DMSO for hours or even days. The resulting pale yellow solution must then be mixed rapidly into an aqueous buffer to produce an aqueous solution containing superoxide. By avoiding the use of a concentrated base, which needs to be neutralized by an equally concentrated buffer, lower concentrations of buffer can be used. The challenge is that DMSO is more viscous than water, and upon mixing it tends to form layers or streams rather than quickly dissolving in water. To efficiently mix DMSO with water, the flowing DMSO must be broken into several streams; then the streams must intersect the rapid aqueous solution flow at right angles. The resultant mixture is then passed into a narrowing, leading to turbulence, and then divided and recombined in a tangential mixer to homogenize the solution. The mixing process is considered to involve the

breakup of the DMSO into small solution packets that are further subdivided by the subsequent turbulent wake, and then finally mixed, through diffusion, into a homogenous solution. McClune and Fee described a device that accomplishes the efficient mixing of 1 part of DMSO with 25 parts aqueous solution in the above manner.[13] The flow rate for their mixer was about 7 mL s^{-1} or 420 mL min^{-1}, with a maximal linear flow velocity of 9 m s^{-1}, and achieved a dead time of 10 to 20 milliseconds. This design was adapted by reducing the channel and orifice diameters while keeping the Reynolds numbers above the transition value for turbulence (> 2000) at half the flow rates for the McClune-Fee device. This adaptation of the aqueous-organic mixer is shown in Figure 4.6. The tangential flow divider for water/DMSO is shown in Figure 4.7, and the four-jet mixer is shown in Figure 4.8. This organic-aqueous mixer will form the first of two stages of mixing. The first stage mixes superoxide dissolved in DMSO rapidly with weak pH 9 buffer. The second stage uses the tangential-jet mixer used in version 3 and mixes the output of the first stage with an equal flow of lower pH buffer to achieve pH below 9. Each stage is fed by a buffer reservoir. The reservoirs were 1-liter Nalgene bottles molded from Eastman Tritan ™ copolyester, which is a high impact and chemically resistant alternative to polycarbonate. These containers withstood pressure much better than their polyethylene counterparts. The same caps for the reservoirs used in version 3 could also be used with the new Nalgene bottles. Tubing within the system was made of high-

111

purity PFA. The diameter of tubing has been increased to 1/8" for lower pressure drop

at the buffer flow rates encountered. The tubing material for DMSO use was Tefzel

(ETFE).   The syringe used with DMSO was all-polypropylene. The materials of the

fittings and connectors were PEEK, Delrin, ETFE, polypropylene, or polycarbonate as

dictated by the required chemical resistance. No metal part came into contact with

solutions. Syringe filters (0.45 µm) were added in-line with the gas supply to the

reservoir bottles. These are meant to keep out any metal particles that may have shed

from the gas supply piping and fittings, where the use of copper, brass and stainless

steel are unavoidable. After the gas filters, all tubing and fittings leading to the

reservoir were made of the plastic materials listed above, which avoids metallic

contamination.   A shutoff valve was added to the DMSO line to prevent contamination

and leaking during replacement of the syringe containing DMSO.

4.2.4   Flow cell

Superoxide in aqueous solution can be observed spectroscopically. The absorption

maxima of the protonated and anionic forms are at 230 nm and 245 nm, respectively.

The extinction coefficient at these and longer wavelengths and various pH have been

obtained; these range from 1800 to 2300 $M^{-1}cm^{-1}$. [14] Direct monitoring of the absorbance

of superoxide in stopped flow has been done. [15] To characterize the superoxide source,

a custom flow cell for monitoring superoxide was constructed to work with fiber-optic

coupled spectrophotometer (StellarNet EPP-2000, Tampa, FL). Initially designed with

flat quartz windows, it was found that the efficiency of coupling light to and from the

fiber optics and into and out of the flow path was very low. This required a

modification using sapphire ball lenses (Edmund Optics, Barrington, NJ) to collimate

the light from the fiber optics to increase the signal. Figure 4.9 shows the design of the

core of the flow cell, which holds ball-lens collimator, while Figure 4.10 shows the

mating frame that holds the optical fiber connectors that couple light from the source

and to the spectrophotometer.

4.3   Path length and wavelength calibration

To obtain the path length of the flow cell, a set of calibration standards was used to

obtain transmittance data on both a standard quartz 1-cm path length using the

Shimadzu UVPC-2401 (Tokyo, Japan) and the flow cell on the StellarNet EPP2000C.

Stock calibration solution was made by dissolving 8.145 mg of 4-hydroxybenzoic acid in

1 mL absolute ethanol, and then in 1 L of 0.1M hydrochloric acid. Further dilutions of

50% and 25% of the stock concentration in 0.1 M HCl were accurately made using a

buret and 100 mL volumetric flask. The absorbance maxima were at 255.3 nm

(Shimadzu) and 256.01 nm (StellarNet). The wavelength scales on both spectrometers

were calibrated with the use of a mercury lamp at the wavelength of 253.65 nm. This

peak appeared at 253.90 nm and 253.26 nm for the Shimadzu (0.1 nm resolution) and

StellarNet spectrophotometers, respectively. The corrected wavelength for the absorbance peak of 4-hydroxybenzoic acid would then be 255.05 nm on the Shimadzu, which agrees with the literature. Transmittance data were converted to absorbance and plotted against concentration. When the two sets of working curves are plotted against one another, the two agree closely. The slopes (14312 ± 92 M^{-1} for Shimadzu data and 14204 ± 228 M^{-1} for StellarNet data) are in effect the product of molar absorptivity and path length. Assuming an accurate path length of 10.00 mm for the quartz cuvette used to obtain the Shimadzu data, the flow cell path length is 9.92 ± 0.23 mm.

4.4   Buffer selection

Accurate superoxide concentrations can be obtained if interferences can be avoided or otherwise subtracted out. The buffer itself can be a source of interference, since some buffers are organic molecules and may absorb in the region below 300 nm. Table 4.2 summarizes spectroscopic data obtained for various candidate buffers and aqueous solutions. The criterion for buffer selection is that it must not absorb strongly in the 230-270 nm range where superoxide can be monitored. It can be seen from the data that buffers other than MOPS (3-(N-morpholino) propanesulfonic acid) do not absorb strongly above 250 nm. Phosphate buffer is in fact usable down to 230 nm. It is upon addition of DMSO (1/10 volume of buffer) that absorbance increases for wavelengths below 260 nm. Glycine, tetraborate, and phosphate buffers may be used with addition

of DMSO, provided a wavelength of 260 nm or greater is used. MOPS may be used at much lower concentrations.

4.5   Initial mixing test

As a test of the mixer, phenolphthalein dissolved in DMSO (0.16 mg mL^{-1}) was used to fill the syringe, resulting in a clear solution. The reservoir was filled with 0.01 M Na tetraborate buffer.   The flow cell was used to mix the two in a 1:25 ratio, resulting in the pink phenolphthalein/borate buffer solution that absorbed at 554 nm. Using the flow cell with the StellarNet spectrophotometer, absorbance data were taken during flow. The flow was stopped and the liquid in the cell allowed time to come to equilibrium. The absorbance was taken again. The difference in absorbance between the 554 nm phenolphthalein peak and 700 nm background was taken as the reading. The results of three trials are tabulated in Table 4.3. A t-test of the data showed that means are not significantly different, implying that mixing can be considered completed.

4.6   Recommendations

So far, the results are encouraging in that the mixer will work as designed. Below is a summary of how two sequential mixers could be used to deliver the target 50 μM superoxide to the filters. This is based on both the literature and the results from our current mixing apparatus.

The first mixer will take 2.5 mM KO_2 in DMSO and rapidly mix that into a weak pH 9 buffer at a ratio of 1:25. This will result in a solution of 100 µM superoxide at pH 9 where the half-life is 2 seconds. By mixing and delivering to the next stage with a dead time of 200 milliseconds or faster, this concentration will be maintained. At the current flow rates, this sets a 34 cm limit to the length of the tubing from the first mixer, which is achievable. The output of the first mixer then goes immediately to the 2nd mixer, where the pH 9 solution is mixed with strong buffer at pH 8 (or lower) at 1:1 ratio resulting in a 50 µM superoxide concentration to be delivered to the syringe filters. At pH 8, the half-life is 0.4 sec, and maintaining this requires mixing and delivery at 40 milliseconds or less. The current mixer does this with a dead time of 115 milliseconds, so this section will have to be re-engineered, and a lower final pH becomes increasingly challenging. The final concentration of DMSO at the filters, considering the two dilution steps, would be 2%. Katka Golubeva (Slauch group) has demonstrated that *Salmonella* tolerates this concentration of DMSO.

At the first mixer, if the pH 9 buffer flow rate is 200 mL min^{-1}, then DMSO flow rate should be 8 mL min^{-1} (1:25). A syringe pump will be used to deliver the DMSO. The following buffers may be used: For the 1st mixing stage, sodium tetraborate / hydrochloric acid or boric acid at pH 8.1 to 9.2, 0.01 M. Tetraborate at pH 9.33, 0.02M

116

proved to be too concentrated when combined with an equal amount of pH 7.8, 0.1 M

phosphate buffer. It was found that 0.01 M tetraborate has a pH of 9.2 at 25 $^{\circ}$C. The

addition of a little hydrochloric acid or boric acid should suffice to bring the pH down

to 9.0. Bielski found that borate, chloride, and perchlorate do not react with

superoxide.[16] McClune reported that the apparent rate of dismutation decreased when

0.1 mM or 0.25 mM EDTA was added.[17] Fe-EDTA complexes act as catalysts for

superoxide dismutation,[18] while a similar chelator, diethylenetriamine pentaacetic acid

(DTPA or DETAPAC) does not.[19]

The buffer for the 2nd mixing stage will be sodium monobasic/dibasic phosphate pH

6.8 to 8.0, 0.10 M. The advantages of the above reagents are that they are available at

high purity and have low trace metal content. Also, the addition of base (KOH or

NaOH) is avoided: bases are difficult to purify. Hydrochloric acid may be substituted

by boric acid if the iron content of hydrochloric acid is an issue.

As was shown above, the UV absorption of these buffers is significant only upon

addition of DMSO. However, there is the option of detecting at 260 nm, where the

buffers and DMSO absorb very little but where superoxide has an absorptivity of 1933

M^{-1} cm^{-1} at pH 8-9. Below pH 9, the extinction coefficient of hydrogen peroxide

decreases as well (50 µM H_2O_2 in a path length of 1 cm would give less than 0.1

absorbance). Bolann *et al.* monitored two wavelengths: 250 nm for superoxide

absorbance and 360 nm as background, and obtained the difference [20] , and it would be

prudent to do the same here. If any kinetics work is to be done, one should be aware

that a small first-order component to the spontaneous dismutation kinetics will be

observed in parallel to the second order process. [17] This was eliminated with the

addition of 1 mM KCN.

To achieve 50 µM superoxide after the second mixer, the concentration of superoxide

coming out of the first mixer should be 100 µM at pH 9, where it has a half-life of 2

seconds. Since the DMSO/pH 9 buffer is mixed at a ratio of 1:25, at a total flow rate of

200 mL min^{-1}, the flow rate of superoxide-containing DMSO is 8 mL min^{-1}, neglecting

the small volume change that occurs upon mixing. This flow is to be effected by a

syringe pump driving the DMSO into the flow divider of the first mixer.   The required

concentration of superoxide in DMSO is then 2.5 mM. In 50 mL of dry DMSO, 8.89 mg

KO_2 needs to be added to obtain this concentration. Addition of crown ether to help

dissolve this amount KO_2 may not even be needed.

Redox-active metal ions of relevance to oxygen radical chemistry (iron, copper,

manganese, zinc) remain catalytically active even at $<10^{-10}$ M concentration. [21] These

metals catalyze the disproportionation of superoxide via Fenton and Haber-Weiss

chemistries. All glassware used must be cleaned: acid wash glassware, even pipet tips. Pyrex glassware or plastic labware may be used after soaking overnight in 0.1 N HCl (ultrapure or de-metaled on an anion-exchange resin and redistilled), and rinsed 3 times in high-purity water. One article described the cleaning method thus: all utensils and glassware were first washed with 0.1 N HCl, followed by purified water, followed by a rinse in a 10^{-4} M EDTA bath at pH 8, rinsed with purified water and dried at 65°C for several hours. [15] The flow system itself must be similarly washed and then thoroughly rinsed with pure water. The purest reagents possible should be used, checking the certificate of analysis for metal content. Water of the highest purity (18.2 MΩ-cm) should be used for solution preparations. Acids and bases should be of the highest purity. Organic reagents should be purified. Do not add EDTA to sequester metals in buffers as Fe-EDTA complexes increase the dismutation rate (use DTPA instead [19]). Containers, syringes, or spatulas made of metal should never be used. Use plastic or glass, not metal spatulas.

4.7 References

1. Haas, A., The Phagosome: Compartment with a License to Kill. *Traffic* **2007,** *8,* 311-330.

2. Winterbourn, C. C.; Kettle, A. J., Redox Reactions and Microbial Killing in the Neutrophil Phagosome. *Antioxid. Redox. Sign.* **2012** [Published online ahead of print October 9 2012].

3. Kettle, A. J.; Anderson, R. F.; Hampton, M. B.; Winterbourn, C. C., Reactions of Superoxide with Myeloperoxidase. *Biochem.* **2007,** *46,* 4888-4897.

4. Craig, M.; Slauch, J. M., Phagocytic Superoxide Specifically Damages an Extracytoplasmic Target to Inhibit or Kill Salmonella. *PLoS ONE* **2009,** *4,* e4975.

5. Imlay, J. A., Pathways of Oxidative Damage. *Annu. Rev. Microbiol.* **2003,** *57,* 395-418.

6. Slauch, J. M., How does the oxidative burst of macrophages kill bacteria? Still an open question. *Mol. Microbiol.* **2011,** *80,* 580-583.

7. Korshunov, S. S.; Imlay, J. A., A potential role for periplasmic superoxide dismutase in blocking the penetration of external superoxide into the cytosol of Gram-negative bacteria. *Mol. Microbiol.* **2002,** *43,* 95-106.

8. Berger, R. L.; Balko, B.; Chapman, H. F., High Resolution Mixer for the Study of the Kinetics of Rapid Reactions in Solution. *Rev. Sci. Instrum.* **1968,** *39,* 493-498.

9. Gibson, Q. H.; Milnes, L., Apparatus for rapid and sensitive spectrophotometry. *Biochem. J.* **1964,** *91,* 161-171.

10. Keith, A., *An On-Demand Source of Superoxide in Aqueous Solution at Near Biologic pH,* Dissertation/Thesis, University of Illinois at Urbana-Champaign, 2011.

11. Valentine, J. S.; Curtis, A. B., Convenient preparation of solutions of superoxide anion and the reaction of superoxide anion with a copper(II) complex. *J. Am. Chem. Soc.* **1975,** *97,* 224-226.

12. Gampp, H.; Lippard, S. J., Reinvestigation of 18-crown-6 ether/potassium superoxide solutions in Me_2SO. *Inorg. Chem.* **1983,** *22,* 357-358.

13. McClune, G. J.; Fee, J. A., A simple system for mixing miscible organic solvents with water in 10–20 ms for the study of superoxide chemistry by stopped-flow methods. *Biophys. J.* **1978,** *24,* 65-69.

14. Bielski, B. H. J., Reevaluation of the Spectral and Kinetic Properties of HO_2 and O_2^- Free Radicals. *Photochem. Photobiol.* **1978,** *28,* 645-649.

15. Riley, D. P.; Rivers, W. J.; Weiss, R. H., Stopped-flow kinetic analysis for monitoring superoxide decay in aqueous systems. *Anal. Biochem.* **1991,** *196,* 344-349.

16. Bielski, B. H. J.; Cabelli, D. E.; Arudi, R. L.; Ross, A. B., Reactivity of HO_2/O_2^- Radicals in Aqueous Solution. *J. Phys. Chem. Ref. Data* **1985,** *14,* 1041-1100.

17. McClune, G. J.; Fee, J. A., Stopped flow spectrophotometric observation of superoxide dismutation in aqueous solution. *FEBS Lett.* **1976,** *67,* 294-298.

18. Bull, C.; McClune, G. J.; Fee, J. A., The mechanism of iron EDTA catalyzed superoxide dismutation. *J. Am. Chem. Soc.* **1983,** *105,* 5290-5300.

19. Buettner, G. R.; Oberley, L. W.; Leuthauser, S. W., The effect of iron on the distribution of superoxide and hydroxyl radicals as seen by spin trapping and on the superoxide dismutase assay. *Photochem. Photobiol.* **1978,** *28,* 693-695.

20. Bolann, B. J.; Henriksen, H.; Ulvik, R. J., Decay kinetics of $O_2^{\bullet-}$ studied by direct spectrophotometry. Interaction with catalytic and non-catalytic substances. *BBA-Gen. Subjects* **1992,** *1156,* 27-33.

21. Schaich, K. M., "Preparation of metal-free solutions for studies of active oxygen species," in *Methods in Enzymology,* Packer, L.; Glazer, A. N., eds. Academic Press, **1990**, pp. 121-125.

4.8   Chapter 4 Figures
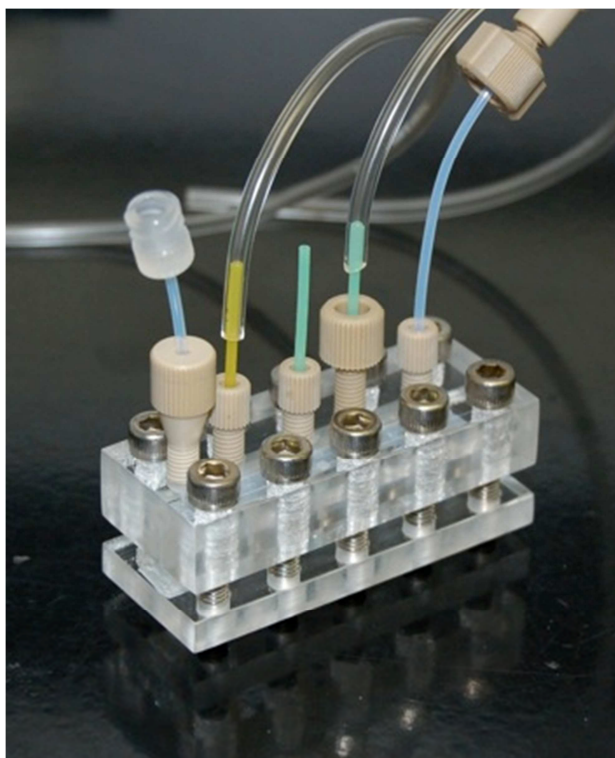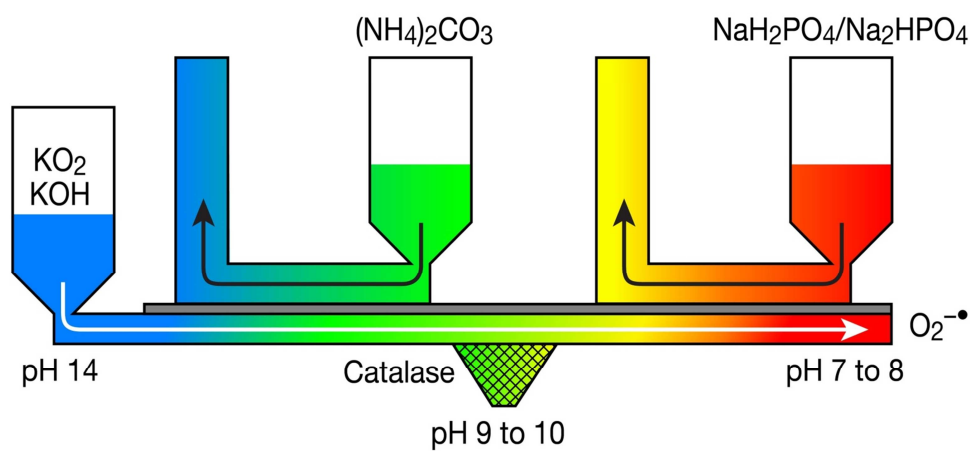
Figure 4.1. Version 1 of the superoxide source. Top: diagrammatic representation. Bottom: realization of device.
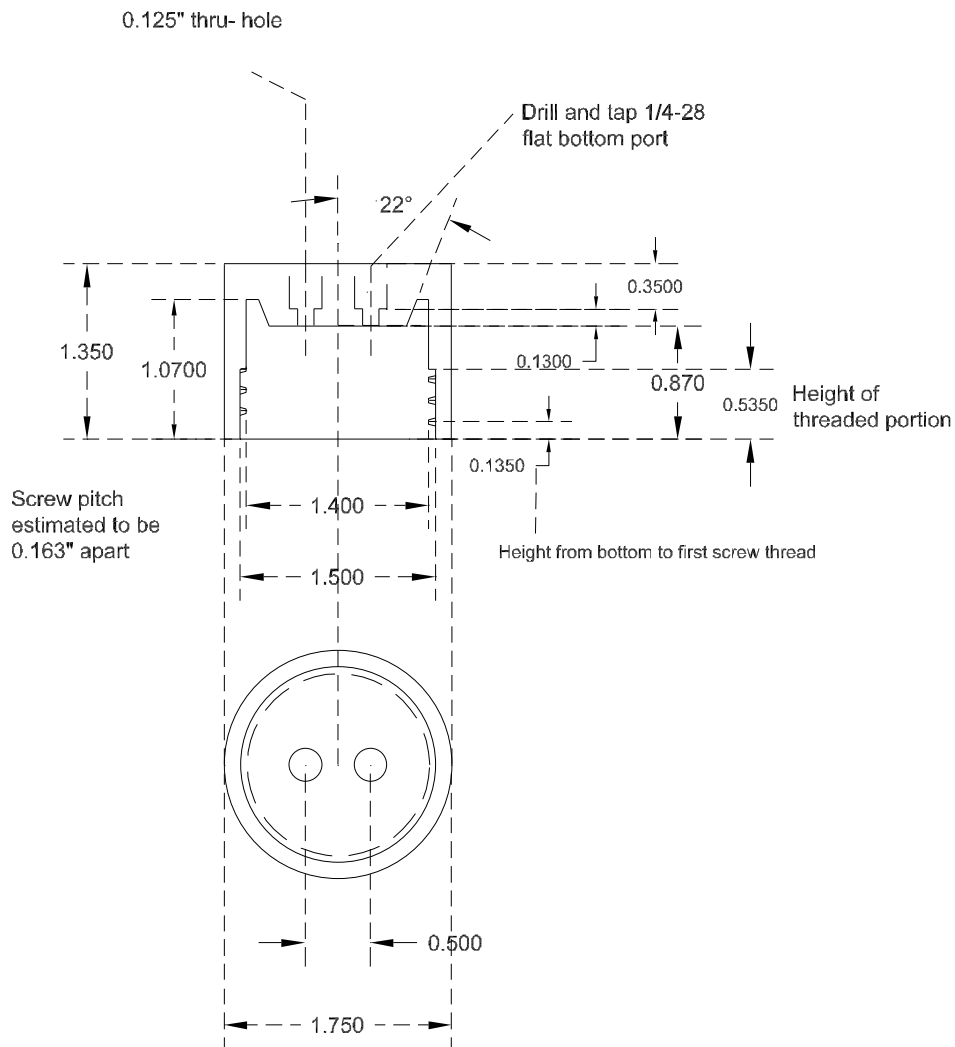
Figure 4.2. Pressure cap for Nalgene bottle.

The following labels appear in the figure:

- 0.125" thru- hole
- Drill and tap 1/4-28 flat bottom port
- 22°
- 0.3500
- 1.350
- 1.0700
- 0.1300
- 0.870
- 0.5350
- Height of threaded portion
- Screw pitch estimated to be 0.163" apart
- 0.1350
- 1.400
- 1.500
- Height from bottom to first screw thread
- 0.500
- 1.750
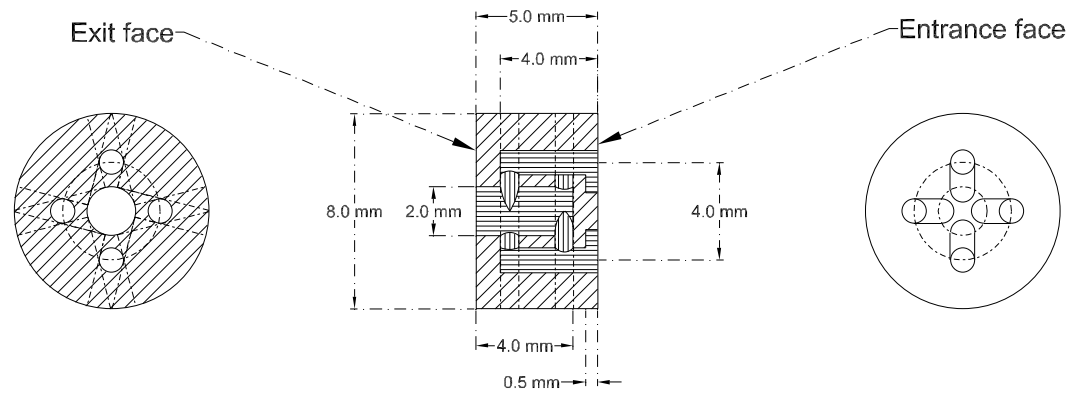
Figure 4.3. Four-jet tangential flow mixer described by Gibson and Milnes (1964).
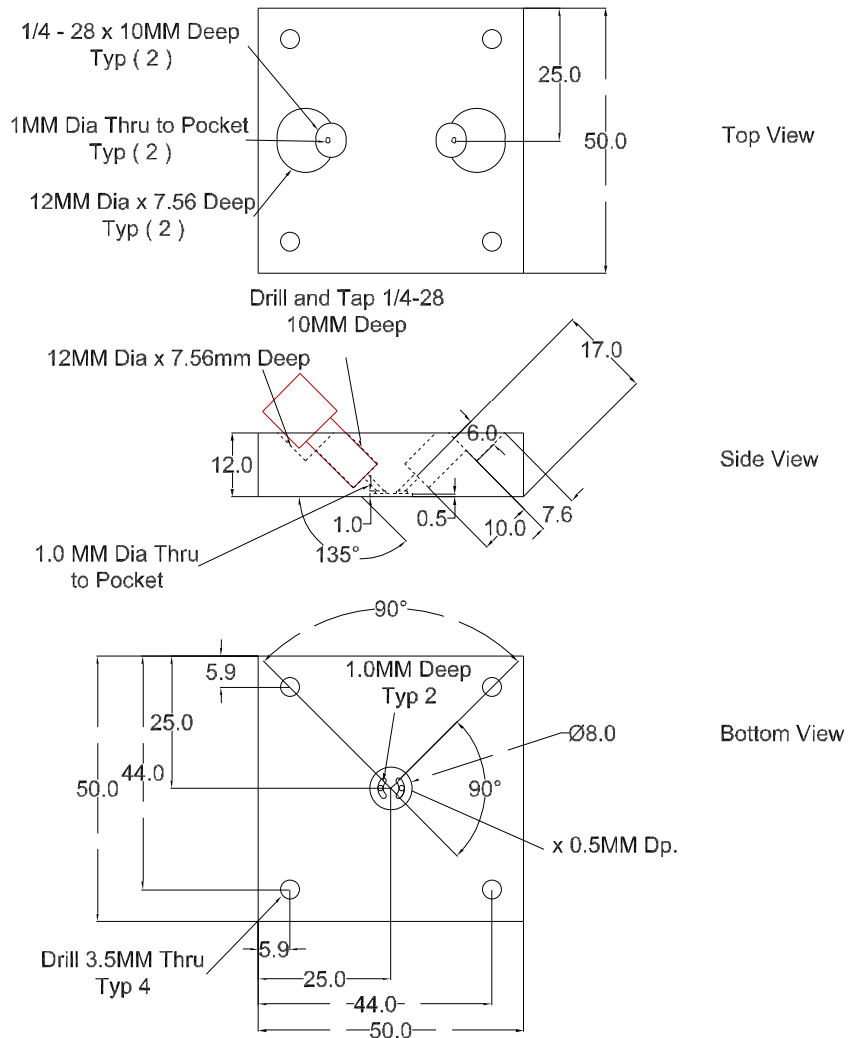
Figure 4.4. Inlet block. Flow from two tubings are combined at the tangential flow mixer (not shown), which is sandwiched between this and the outlet block.

TOP VIEW

BOTTOM VIEW

SIDE VIEW

Unless specified, dimensions are in millimeters
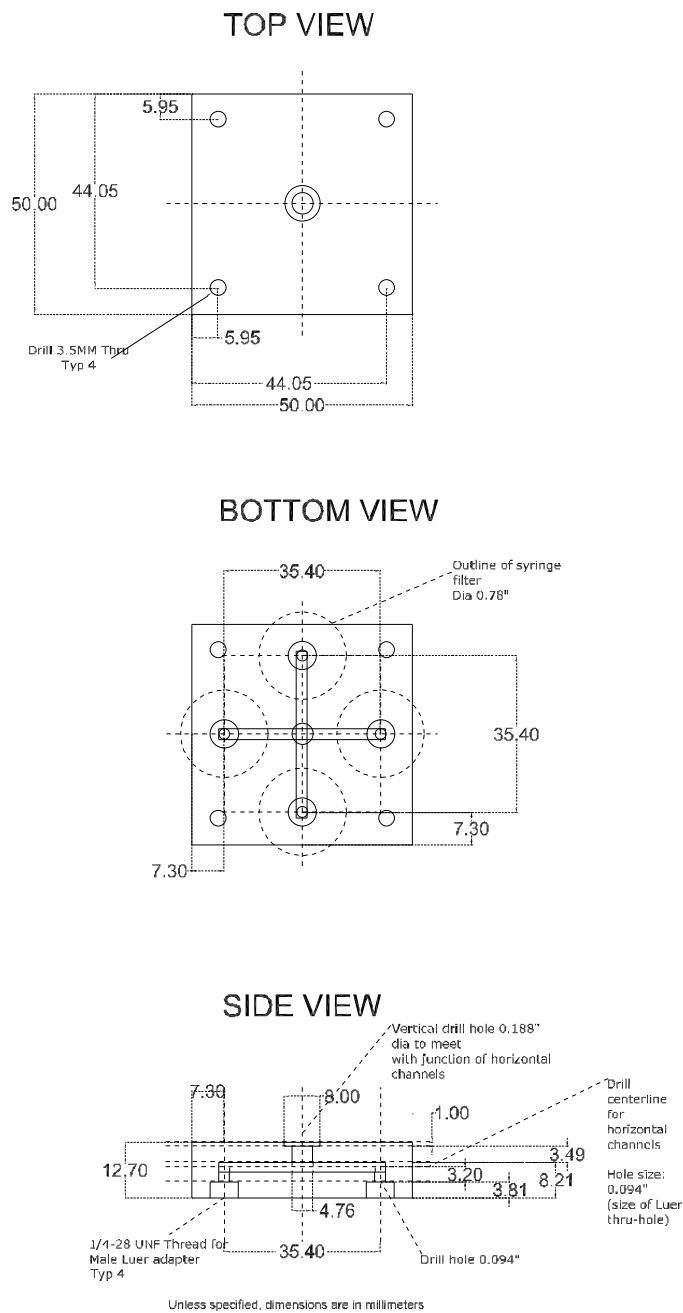
Figure 4.5. Outlet block. Four channels distribute the superoxide solution to four male-Luer adapters (not shown). The tangential mixer is sandwiched between the inlet and outlet blocks.

127
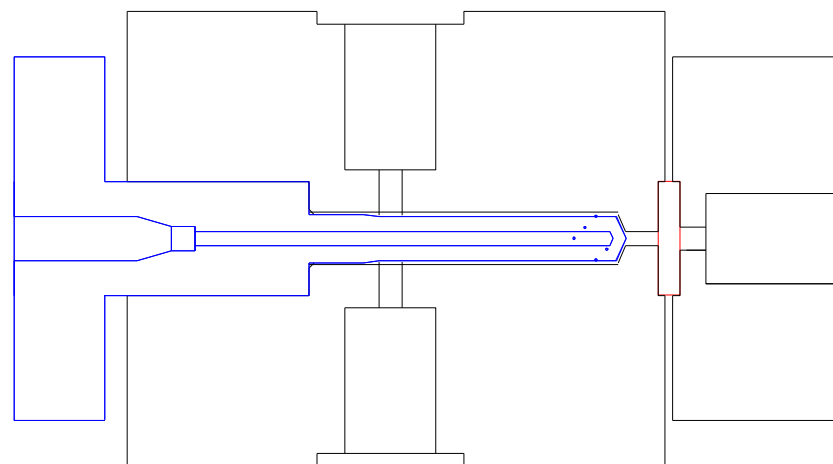
Figure 4.6. Aqueous-organic mixer showing the body (black), flow divider (blue), and the tangential mixer (red). The inlet for DMSO is on the left, the two inlets for aqueous buffer are at the top and bottom of the body, and the outlet is on the right.

Knurl outside surface

0.250

4 cross (thru) holes
distributed over
0.090

#60 drill depth
1.851

outside thread: 5/16-24

diameter to seal with 0.1319 hole

131°

Upchurch 10-32

Ø1.000

This Ø referenced to actual Ø of
0.1319 hole. Should be no
smaller than 0.0120 less the Ø
of Ø0.1319 hole.

Ø 0.120$^{+0.000}_{-0.002}$

0.813

0.150

0.730

0.500
Depth of Ø 0.067 hole

distance of first hole to shoulder

0.876$^{-0.005}_{-0.000}$

length of finger from shoulder to
point

Flow divider material: Kel-F
Dimensions in inches

center hole: #60 (0.040)

End-on detail of nozzle

4 cross holes: #97 (0.0059)

Figure 4.7. Detail of flow divider. Dimensions in inches.
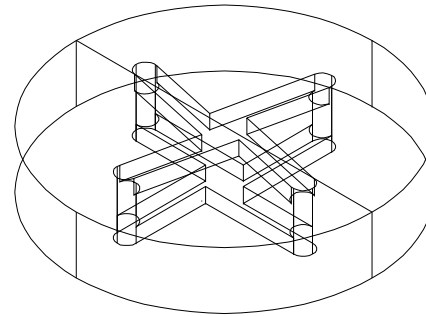
Figure 4.8. Design of the four-jet tangential mixer. Overall diameter is 0.3125 inches, thickness is 0.06 inches.

Mill thru oval hole 3 mm wide

Outside thread metric 14-0.9-4

60 deg countersink (same on other side)

Mouth diameter is critical. Same diameter on other side

3 mm thru hole (diameter not critical)

22.000

18.000

6.008

4.110

View from side

Dril and tap 14-0.9-4
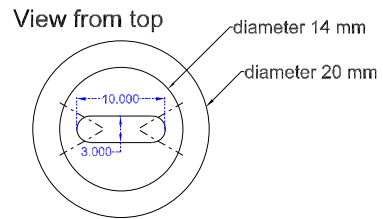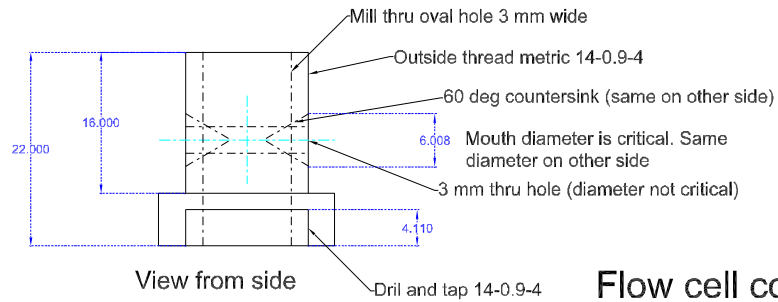
Flow cell core

all units in mm unless specified

Material: black Delrin

Rotated 90 degrees with respect to figure on left

flats 1 mm deep by 6 mm square

View from top

diameter 14 mm

diameter 20 mm

10.000

3.000
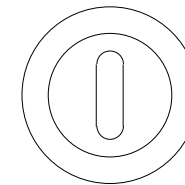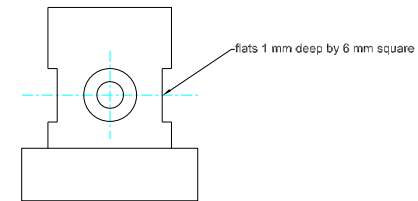
Figure 4.9. Flow cell core consisting of black Delrin body. Recesses for the ball lenses as well as threads for attaching syringe filters are shown.
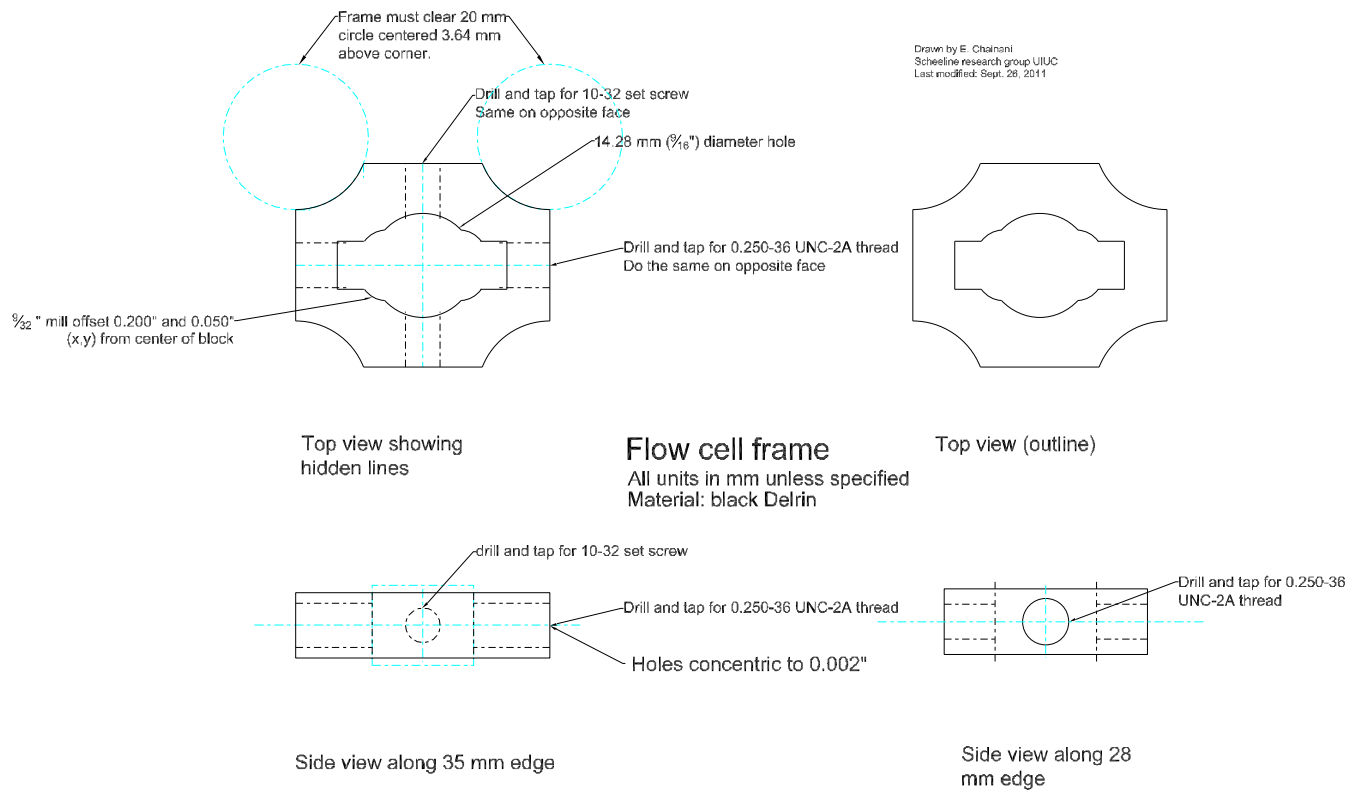
Figure 4.10. Frame for holding the flow cell core and the fiber optic adapters.
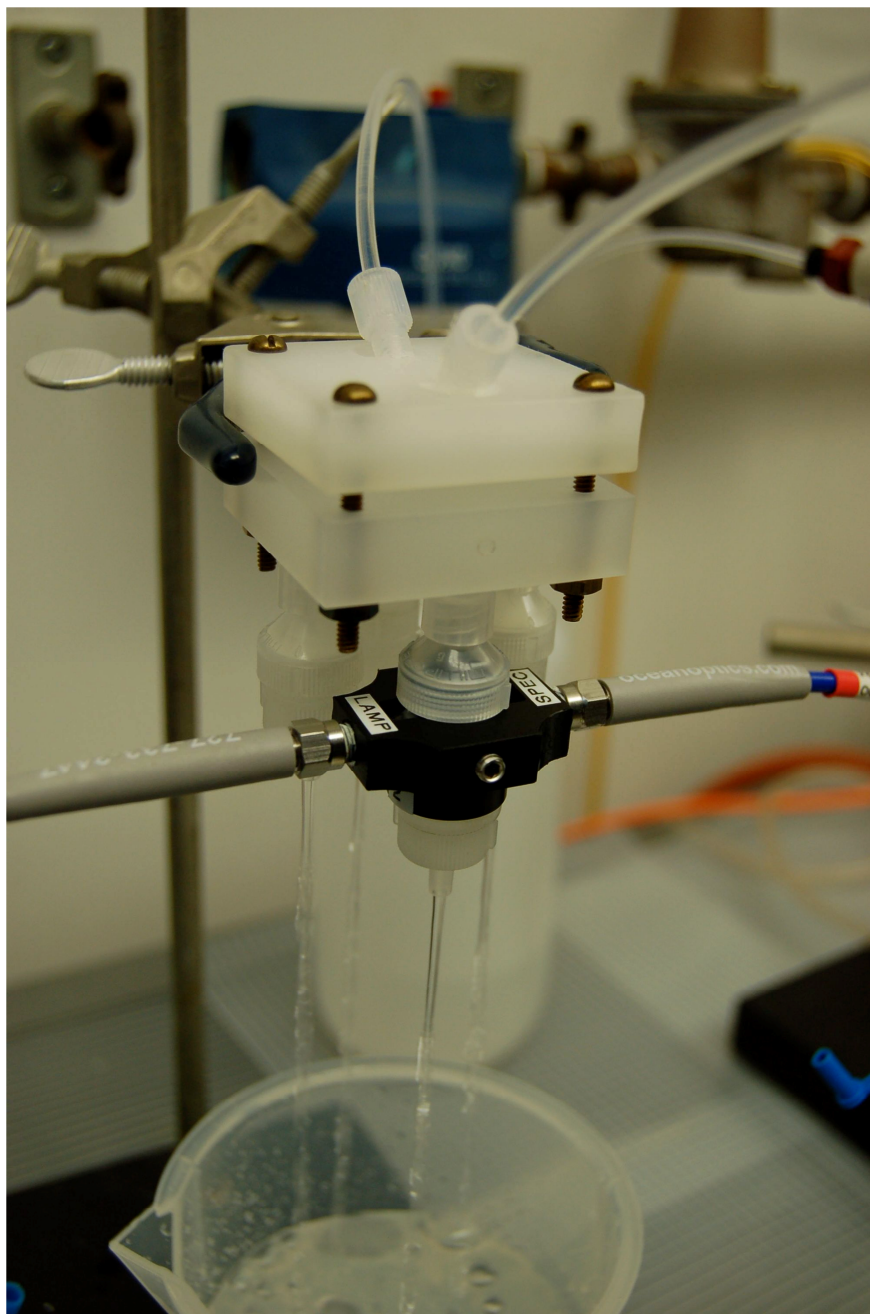
Figure 4.11. The superoxide source during test. The absorbance flow cell is attached in place of one of the four filter holders.
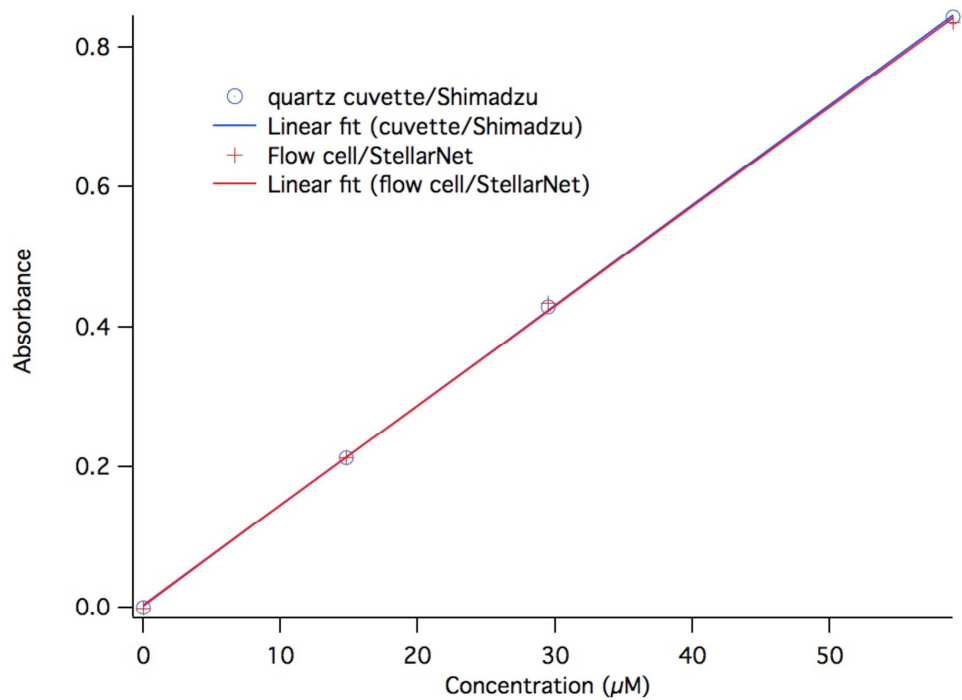
Figure 4.12. Calibration data for path length of the flow cell.

4.9 Chapter 4 Tables

Table 4.1. Final concentration of superoxide as a function of flow rate. Flow rates are measured values, concentrations are calculated. Initial concentration is 200 μM. Final pH = 9.0. Data by Aaron Keith.

Driving Pressure (PSI)	Total flow rate (mL min^{-1})	Dead time (s)	Final Conc. of $O_2^{\bullet-}$ (μM)	Percent remaining $O_2^{\bullet-}$ (%)
20	175 ± 10	0.254	121	66
30	290 ± 13	0.151	144	72
40	388 ± 6	0.114	155	77

Table 4.2. Summary of spectroscopic data for select wavelengths. Reference is Milli-Q water. PB means phosphate buffer, and MOPS is 3-(*N*-morpholino)propanesulfonic acid.

Solution (2.5 mL)	Additive	230 nm	240 nm	250 nm	260 nm	270 nm
Milli-Q water	0.1 mL DMSO	3.127	0.511	0.066	0.017	0.008
0.02 M Na tetraborate	none	0.002	0.003	0.001	0.001	0.001
0.2 M Na tetraborate, pH 9.36	none	0.004	0.003	0.003	0.002	0.002
0.2 M Na tetraborate, pH 9.36	0.1 mL DMSO	3.122	0.505	0.062	0.014	0.007
0.1 M Na PB, pH 7.88	none	0.008	0.007	0.006	0.006	0.006
0.2 M tetraborate + 0.1 M NaPB	0.1 mL DMSO	3.014	0.253	0.037	0.012	0.008
0.1 M glycine, pH 9.2	none	0.321	0.034	0.005	0.002	0.001
MOPS buffer, 1.5 M, pH 6.0	none	3.299	0.834	0.356	0.277	0.264
MOPS buffer, 1.5 M, pH 6.7	none	3.437	0.925	0.411	0.351	0.364

Table 4.3. Results of mixing test using phenolphthalein dissolved in DMSO.

Trial	Flowing			Stopped		
	554 nm	700 nm	Δ Abs	554 nm	700 nm	Δ Abs
1	0.5822	0.0150	0.567	0.59348	0.025395	0.568
2	0.5732	0.0268	0.546	0.58473	0.024247	0.560
3	0.5829	0.0264	0.556	0.62094	0.05325	0.568
		Average	0.556		Average	0.565
		SD	0.010		SD	0.004

CHAPTER 5

CONCLUSION AND RECOMMENDATIONS

5.1 Microfabricated electrode

Silicon is an ideal substrate for rigid sensors, as silicon wafers are designed to undergo metal deposition, lithography, and microfabrication. Silicon may be laser ablated to allow shaping of the sensor, although the desired shape must take into account the crystal planes to avoid. Stealth dicing, where the laser is focused into the interior of the wafer to cause internal fracture, should be used when available to avoid collection of debris on the surface of the sensor.[1] The electrode design and fabrication techniques described here apply to a flexible polymeric substrate with a few modifications. Kapton® polyimide may still be used as a substrate, but it is recommended that a liquid polyimide film be spin coated onto the commercial Kapton® film surface and cured to create a smooth surface that is free of voids (John Yeager, personal communication, March 18, 2010). Adhesion of metals to flexible substrates is critical; thus regardless of design or substrate, it is recommended that a protective overlayer be used to 1) prevent electrolyte from accessing the metal/substrate interface where it can cause corrosion, and 2) define electrode areas. HD MicroSystem's HD-4100 series photosensitive polyimide (PSPI) was chosen as the wafer passivation and protection material mainly due to its compatibility with the original substrate (Kapton® polyimide by DuPont).

The well-matched coefficient of thermal expansion (CTE), high tensile strength and yield strain of polyimide would have brought these advantages to the flexible electrode format. But upon switching to a rigid silicon substrate, it might be argued that polyimide might be a second choice to benzocyclobutene (BCB)-type resins (an example would be DuPont CYCLOTENE 4000). In this case, the rigid electrode would have benefitted from the increased volume resistivity and much lower moisture uptake (0.2% as opposed to polyimide's 2% by weight). It might also have benefitted from improved feature retention, mainly due to the fact that the cure temperature (250 °C) for BCB is lower than its glass transition temperature (>350 °C). BCB also exhibits a high degree of planarization, a property in which the underlying features do not produce "bumps" in the polymer surface. [2]   Table 5.1 compares the characteristics of polyimide and benzocyclobutene.

One other challenge is the development of a true solid-state reference electrode that does not require a filling solution. [3-6] Methods to modify the functionality of each electrode to either respond to a specific analyte or to operate as a reference electrode would have to be addressed to increase the utility of a microfabricated sensor. The microfabrication methods used here can be used to make an array of microsensors as suggested by George Wilson [7]. Enzyme-based amperometric sensors can be made using precision delivery of enzymes with a microinjector into microwells—in this case, the lithographically-defined recess in the polyimide over the gold. This results in a sensor

highly selective for the enzyme substrate (SOD and cytochrome c for superoxide [8], horseradish peroxidase for hydrogen peroxide [9]). The small electrode area poses a challenge to developing amperometric sensors with biologically relevant detection limits, and the situation is not much better for potentiometric sensors with Nernstian response if superoxide is to be determined in micromolar concentrations. It was shown in this work that cyclic voltammetry of ferrocenemethanol in the 100-micromolar range with the bare gold microelectrode resulted in currents of up to a 100 picoamperes. Enzyme biosensors made from cytochrome c bound to self-assembled monolayers of alkanethiols on gold have much lower electron transfer rates (apparent electron transfer rate constant $log\ k$ < 2, alkyl chain length n=10). [10, 11] Besides, there are limits to area coverage of immobilized enzyme. [12] Immobilized enzymes on conducting polymers would increase effective electrode area, but the required diffusion through the polymer matrix muddles temporal resolution. The problem of sensitivity can be resolved by integrating electronics into the holder for extracting and amplifying currents and reducing noise, as close as possible to the signal source. An analog front-end built on advanced low-noise operational amplifiers coupled with a system-on-chip that supports real-time signal processing could overcome the sensitivity barrier. Developments in many areas (microfabrication [13], molecular recognition element, signal processing, sensor calibration) need to come together to make practical *in vivo* microelectode sensor arrays. [14]

5.2   Acoustically levitated drop reactor

Ultraviolet and near-infrared spectroscopy, chemiluminescence, fluorescence, and now electrochemical measurements have been achieved by the group members working on the levitated drop. Further optimization of the LDR will no doubt add to this list of analyses; extension to mass spectrometry as already demonstrated by Smith seems particularly promising. Precise control of the position of the drop will improve spectroscopic methods where the light path is generally fixed in space. Alternatively, a system of tracking the drop position and deflection of light to follow drop movement could be devised. While components are on hand to attempt this for fluorescence, an additional steerable mirror would be required to carry this out for absorbance; in any event, resources were inadequate to implement such tracking. Controlling the humidity in the immediate vicinity of the drop will mitigate drop evaporation. This requires a means of humidifying the air in the enclosure surrounding the instrument. Woo-Hyuck Choi implemented humidification and thermostating with "bang-bang" feedback-controlled hardware, but it was found that the heater drew high currents, causing electrical interference incompatible with electrochemical measurement. Multiple drop-on-demand dispensers would increase the range of time of experiments by being able to either supply distilled water to compensate for evaporation, as well as add multiple reactants. Alternatively, a more precise means of estimating drop volume over time needs to be made for improved corrections to volume, which can be achieved

by increasing resolution and depth of field of the camera used to obtain drop images. The velocity of the incoming drop needs to be limited to avoid ejecting secondary drops or knocking the drop off the electrode. This could be accomplished by imparting the minimum amount of charge to the droplet that would launch it from the syringe, thus decreasing the droplet's initial velocity. This requires adjustment of the applied high voltage, but we only had a limited selection of high voltage supplies to work with. Mixing in the drop may be enhanced by modulating the drive to the resonator, causing a corresponding modulation of the acoustic pressure, which results in excitation of vibration modes of the drop. [15] Preliminary experiments have demonstrated this effect, but quantitative measurements have yet to be done. Enhanced mixing through acoustic pressure modulation has the potential to increase the range of observable first-order constants beyond 1 s^{-1}. Khanh Ngo will investigate this topic in his undergraduate thesis.

5.3   Superoxide source

After several iterations in the design of the superoxide source, the project is at a stage where we are very close to generating sustained flow of superoxide that can be used to determine *in vitro* the effects of biologically relevant concentrations of superoxide on various strains of *Salmonella enterica* serovar *typhimurium.* After exposure to superoxide, the filters containing the bacteria can be plated and incubated, and surviving strains can

be tested to determine which retain the virulence phenotype. Also, the flow system can be used to calibrate microelectrodes designed to detect superoxide. While the on-demand superoxide source shows promise to continuously produce aqueous superoxide fit for biologic research, important modifications must still be made. Provisions for injecting additional compounds into the flow, such as anti-microbial peptides and lysozyme that might modulate the activity of superoxide against *Salmonella* would make useful modifications. [16] Catalase may be introduced into the flow system (perhaps added to the buffer) should the elimination of hydrogen peroxide be required. The resulting apparatus could be the closest approximation to an artificial phagosome so far to be used to clarify mechanisms of bacterial killing in a systematic manner. Assuming protocols can be developed that allow cells other than bacteria to be immobilized and subjected to reactive oxygen in a similar manner, the superoxide source would enable investigation into mechanisms of oxidative damage that are relevant to diseases associated with oxidative stress. Apart from NIHL, this list includes Alzheimer's, amyotrophic lateral sclerosis (ALS), atherosclerosis, and rheumatoid arthritis, to name a few. Comparison of markers produced by oxidation of cells *in vitro* with molecular fingerprints obtained from cells or biological fluids will reveal pathways creating damage *in vivo*. [17] Elucidation of ROS-induced damage can lead to antioxidant therapeutic interventions, and reactive oxygen sensors will prove to be useful in assessing the effectiveness of these therapies. [14]

5.4 References

1. Kumagai, M.; Uchiyama, N.; Ohmura, E.; Sugiura, R.; Atsumi, K.; Fukumitsu, K., Advanced Dicing Technology for Semiconductor Wafer—Stealth Dicing. *IEEE Transactions on Semiconductor Manufacturing* **2007,** *20,* 259-265.

2. So, Y.; Garrou, P.; Im, J.; Scheck, D. M., Benzocyclobutene-based polymers for microelectronics. *Chemical Innovation* **2001,** *31,* 40-47.

3. Ghilane, J.; Hapiot, P.; Bard, A. J., Metal/Polypyrrole Quasi-Reference Electrode for Voltammetry in Nonaqueous and Aqueous Solutions. *Anal. Chem.* **2006,** *78,* 6868-6872.

4. Blaz, T.; Migdalski, J.; Lewenstam, A., Junction-less reference electrode for potentiometric measurements obtained by buffering pH in a conducting polymer matrix. *Analyst* **2005,** *130,* 637-643.

5. Kisiel, A.; Marcisz, H.; Michalska, A.; Maksymiuk, K., All-solid-state reference electrodes based on conducting polymers. *Analyst* **2005,** *130,* 1655-1662.

6. Yang, H.; Kang, S. K.; Choi, C. A.; Kim, H.; Shin, D.; Kim, Y. S.; Kim, Y. T., An iridium oxide reference electrode for use in microfabricated biosensors and biochips. *Lab on a Chip* **2004,** *4,* 42-46.

7. Yu, P.; Wilson, G. S., An independently addressable microbiosensor array: What are the limits of sensing element density? *Faraday Discuss.* **2000,** *116,* 305-317.

8. Wilson, R. C. K.; Phuong, D. T.; Chainani, E.; Scheeline, A., Flexible, micron-scaled superoxide sensor for in vivo applications. *J. Electroanal. Chem.* **2011,** *662,* 100-104.

9. Frasconi, M.; Favero, G.; Tortolini, C.; Mazzei, F., Bioelectrochemical Characterization of Horseradish and Soybean Peroxidases. *Electroanalysis* **2009,** *21,* 2378-2386.

10. Avila, A.; Gregory, B. W.; Niki, K.; Cotton, T. M., An Electrochemical Approach to Investigate Gated Electron Transfer Using a Physiological Model System: Cytochrome c Immobilized on Carboxylic Acid-Terminated Alkanethiol Self-Assembled Monolayers on Gold Electrodes. *J. Phys. Chem. B* **2000,** *104,* 2759-2766.

11. Murgida, D. H.; Hildebrandt, P., Redox and redox-coupled processes of heme proteins and enzymes at electrochemical interfaces. *Phys. Chem. Chem. Phys.* **2005,** *7,* 3773-3784.

12. Vertova, A.; Forlini, A.; Rondinini, S., Probing the Electron Transfer Process of Cytochrome C Embedded in Mixed Thiol SAM on Electrodeposited Gold. *J. Electrochem. Soc.* **2012,** *159,* 81-F86.

13. Buck, R. P.; Cosofret, V. V.; Lindner, E.; Ufer, S.; Madaras, M. B.; Johnson, T. A.; Ash, R. B.; Neuman, M. R., Microfabrication technology of flexible membrane based sensors for in vivo applications. *Electroanalysis* **1995,** *7,* 846-851.

14. Prieto-Simón, B.; Cortina, M.; Campàs, M.; Calas-Blanchard, C., Electrochemical biosensors as a tool for antioxidant capacity assessment. *Sensors Actuators B: Chem.* **2008,** *129,* 459-466.

15. Yarin, A. L.; Weiss, D. A.; Brenn, G.; Rensink, D., Acoustically levitated drops: drop oscillation and break-up driven by ultrasound modulation. *Int. J. Multiphase Flow* **2002,** *28,* 887-910.

16. Kim, B.; Richards, S. M.; Gunn, J. S.; Slauch, J. M., Protecting against Antimicrobial Effectors in the Phagosome Allows SodCII To Contribute to Virulence in Salmonella enterica Serovar Typhimurium. *Journal of Bacteriology* **2010,** *192,* 2140-2149.

17. Dalle-Donne, I.; Scaloni, A.; Giustarini, D.; Cavarra, E.; Tell, G.; Lungarella, G.; Colombo, R.; Rossi, R.; Milzani, A., Proteins as biomarkers of oxidative/nitrosative stress in diseases: The contribution of redox proteomics. *Mass Spectrom. Rev.* **2005,** *24,* 55-99.

5.5   Chapter 5 Tables

Table 5.1. Comparison of properties of cured films of HD-4100 series photosensitive polyimide against CYCLOTENE 4000 benzocyclobutene (BCB) resin. Data compiled from manufacturer's specifications sheets.

Property	PSPI (HD-4100 series)	BCB (CYCLOTENE 4000 series)
Relative permittivity at 1 MHz	3.4	2.65
Volume resistivity ($\Omega \times$cm)	2.4×10^{16}	1×10^{19}
Coeff. of thermal expansion (ppm °C^{-1})	35	52
Glass transition temperature (°C)	330	>350
Cure temperature (°C)	375	250
Moisture absorption (%)	2-3	0.2
Tensile strength (MPa)	200	87
Elongation to break (%)	45	9
Planarization	Poor	Excellent

APPENDIX A

MICROFABRICATION PROCEDURES

A.1 Kasper Model 2001 Wafer alignment system

The Kasper 2001 Wafer Alignment System (commonly referred to as a "mask aligner") is an integrated optical-mechanical, pneumatic-electrical system, which allows accurate alignment of sensitized semiconductor wafers with a mask and exposes them to collimated UV light from a mercury lamp. After the substrate is coated with photoresist by a spin coater, the mask aligner is used to expose the substrate material using broadband UV light. This aligner uses a split field microscope: two parallel optical systems, magnifying two areas across each other on the wafer (the position of each objective is adjustable). The split field microscope presents them both at once, one on each side of the vertical hairline as viewed on the eyepiece. Each half of the split field is roughly 0.4 cm across (with the 2x objectives and 10x eyepieces). Also when centered on the origin, the objectives can be brought to within 2.5 cm from the center.

A.1.1 Mask design

Registration marks should be at least 500 μm wide, to be clearly visible under the microscope. Suggested shapes are crosses or triangles on the mask that line up with sharp features on the substrate such as circles or triangles on the substrate. These sharp

features allow positioning with high accuracy. The movement of stage is the same distance up/down and left/right, but due to the split field optical arrangement, the optical field is narrower up/down (y-axis) than it is left/right (x-axis).

A.1.2 *Important guidelines for placement of alignment marks on mask*

- Left/right movement allows viewing only to the edge of a 3-inch wafer. The best place for alignment marks are within +/- 1.5 inches of center, along the x-axis.

- The range of motion is narrower up/down and does not permit viewing of features more than a few inches above and below the center. Alignment marks along the y-axis are not visible and should not be used.

- Alignment marks in the center of the wafer should not be used with the Kasper. It is possible to view them only on one of the split fields.

- Do not place alignment marks within 1/8 inch from the wafer edge, as this is the edge bead area and is always poorly developed.

- Starting at the center, movement towards the right is limited to the edge of a 4-inch wafer. Towards the left, only up to the edge of a 3-inch wafer can be seen.

A.1.3 *Adjusting the objectives*

Each objective is locked in place by a thumbscrew behind it. To move the objective, loosen the thumbscrew and use the rods to move it across the rails. Always rotate the

objective on its turret after moving it to make sure it is in the locked position. It is best to keep the objectives at the same distance from the center, since most alignment marks are placed that way.

A.1.4 *Procedure for exposure of sensitized wafer*

1. Turn on by pressing POWER.

2. Press MASK LOAD switch "on" to cause the optical head to rise.

3. Lift the mask holder and load the mask on the holder

4. Load the wafer on the chuck.

5. Replace the mask holder to its down (horizontal) position.

6. Press MASK LOAD switch "off" to lower the optical head and apply vacuum to the mask holder.

7. Press the LOADED MANUAL switch. The wafer chuck piston will rise and the unit will enter separation mode.

8. Locate alignment marks using the left-hand scanning control disk (the lock button must be pressed to move the mask and wafer). Align the substrate with the mask using the right-hand X-Y alignment control disk (holding down the button enables coarse movement). Rotate the wafer using the wafer rotation knob if necessary.

9. Press CONT (contact switch) to bring the wafer into contact with the mask.

10. Set exposure time desired.

11. Press MANUAL EXPOSE switch to begin exposure.

12. After exposure, press VISUAL ALIGN to raise the head, and then press EJECT to cause the wafer chuck to descend.

13. Raise the mask holder and remove the wafer.

A.2 Adhesion promoter for AZ 5214E and AZ P5620

A safer alternative to flammable HMDS priming is diphenylsilanediol, which is, available at 95% purity from Sigma-Aldrich (CAS # 947-42-2; 216.31 g/mol.; MP 144 $^{\circ}$C; FP 53 $^{\circ}$C). To prepare adhesion promoter solution, dissolve 1 g diphenylsilanediol in 200 mL solvent, propylene glycol methyl ether acetate (PGMEA or SU-8 developer).

A.2.1 *Procedure for applying adhesion promoter*

1. Prebake Si wafer at 200 $^{\circ}$C for 5 min.

2. Cool in nitrogen (dry) atmosphere.

3. Spin coat at 6000 rpm for 60 s (program Adh_promoter).

4. Post bake at 180 $^{\circ}$C for 2 min. Cool.

5. Proceed with AZ5214E or AZ P4620 spin coating.

A.3 Photodefinable polyimide (HD-4100) Process

HD-4100 is a negative-tone photodefinable polyimide (PI) resist with final cure temperature of 375ºC. It was used as a passivation layer on silicon and as a protection layer over metal patterns. Important notes: Moisture is detrimental to stability of HD-4100. Avoid condensing humidity inside bottle by warming container to room temperature (RT) before opening. Avoid bubble formation by shaking or stirring. Store the original container in the freezer, and transfer to another bottle for dispensing. Keep dispense bottle refrigerated when not in use.

A.3.1 Procedure for HD-4100

1. Set one hotplate to 200 ºC (with nitrogen purge), another hotplate to 95 ºC (for softbake), and another to 150 ºC (for post-development bake, if desired).

2. Clean substrate. Deionized water (DI) followed by acetone then isopropyl alcohol (IPA) is a minimum cleaning step. On blank wafer, use piranha solution (3:1 concentrated sulfuric acid to 30% hydrogen peroxide) if organic residue is suspected.

3. Blank wafer: bake at 200 ºC for 5-10 min. For PI-passivated wafer, O_2 plasma alone is sufficient (the etch rate in O_2 plasma is less than 0.15 µm /min). For wafer with both PI and Si areas, O_2 plasma followed by dehydration bake for 3 min.

4. Spin coat 4000 rpm for 30 s (5 µm cured thickness) or 5000 rpm (4 µm cured) after 10 s spread cycle at 1000 rpm. No adhesion promoter needed for HD-4100.

5. Edge-bead removal by running EBR program on spinner. Use spatula with EBR program to remove no more than 3 mm of PI from the wafer edge.

6. Softbake at 85 °C for 90 s; followed by 95 °C for 90 s (set hotplate to 95 °C, leave open for 90 s, then cover for 90 s). Cool to RT.

7. Exposure: 150 to 400 mJ/cm² (I-line); 100 to 300 mJ/cm² (broadband). Do <u>one</u> of the following:

    a. For blanket passivation layer, no imaging: Flood expose for 80 sec on Kasper (equivalent to 2 x 400 mJ/cm²).

    b. For imaging: 40 s on Kasper @ 10 mW/cm².

    c. Using post-exposure bake (PEB): lower exposure energy. In this case use 115 mJ/cm².

8. Required: Hold for a minimum 5 minutes in a covered container at RT. The wait is critical for best resolution.

9. Optional: PEB 80 °C for 60 s.

10. Develop in PA-401D (puddle 20-60 s, then stream) followed by a rinse in PA-400R. Using squeeze bottles of developer and rinse instead of a soaking bath is a good method. A cloudy residue that forms during rinsing means incomplete development; switch back to developer, then rinse again.

11. Spin dry 3000 rpm or blow dry with nitrogen.

12. Post-development bake to reduce "crowning": 150 °C for 100 s then 200 °C for 100 s. Cool. Inspect on microscope.

13. Cure on hot plate or oven in a nitrogen atmosphere (oxygen <800 ppm): RT to 200 °C @ 10 °C/min, hold 200 °C for 30 min, ramp to 375 °C at 10 °C/min; hold 375 °C for 60 min; gradual cool to RT. Use program #10 on Torrey Pines Scientific hotplate HP 61, with nitrogen purge.

A.4 Image Reversal Process

Positive resists have a typical positive slope of 75-85°. AZ5214E is a special photoresist intended for lift-off techniques, which require a negative wall profile. The image reversal is carried out by an image-wise exposure with lower than normal energy for a positive process. This is followed by an image-reversal bake that activates only above 110 °C and only in the exposed areas of the resist. A flood exposure (no mask) makes the unexposed areas soluble for development. The result is a negative image of the mask pattern, which is ready for metal deposition. Dissolving the metal-coated resist with solvent causes the metal over resist to "lift-off", leaving only the metal pattern that was deposited directly on top of the substrate. This works very well for fine (< 10 μm) features.

A.4.1 AZ 5214E Procedure

In this procedure, the wafers have been pre-coated with polyimide passivation layer and baked to final cure temperature. The critical image-reversal bake temperature was found to be optimum at 120 °C.

1. Set one hotplate to 95 °C, another to 120 °C (+/- 1 °C), and another to 180 °C. Dilute 1:5 AZ 400 K: DI water.

2. Clean wafer with solvent, water, then piranha solution (for blank wafer). For PI-passivated substrate, solvent, water, then O_2 plasma.

3. Bake at 180 °C for 2 min to remove water layer. Cool to room temperature.

4. Spin coat adhesion promoter (needed for adhesion to silicon areas).

5. Spin coat AZ 5214E. For 1.4 μm, spin at 4000 rpm for 30 s.

6. Softbake the spun AZ for 1 min @ 95 °C.

7. Expose with mask 2 sec at 9 mW/cm^2. Recommended is 19 mJ/cm^2.

8. Post exposure bake 2 min @ 120 °C. This temperature is critical.

9. Flood expose (no mask) 124 sec on Kasper @ 9 mW/cm^2. Recommended is > 200 mJ/cm^2, most recipes use about 1100 mJ/cm^2.

10. Develop with AZ 400K 1:5 for 60-90 s.

11. Dry with N_2. Inspect under microscope

12. Bake-out for 1 min @ 95 °C.

13. Prior to metal deposition: O_2 plasma 100W for 30 s.

14. Deposit metal (60 Å Ti-1000 Å Au-60 Å Ti).

15. Lift-off procedure. This requires a lot of patience and time! Start by soaking the wafer in acetone followed by 180 s of ultrasonication. Do this twice. This removes large lift-off areas. Inspect under microscope. If lift-off is incomplete or debris still present, soak for longer in acetone (2 min) followed by 5 min in IPA. May sonicate longer if debris is persistent. Shipley Microposit Remover 1165 (composed primarily of N-methyl-2-pyrrolidone or NMP) may also be used and was found to be effective: sonicating in 1165 for 10 minutes breaks up the metal into tiny particles and does not seem to harm cured HD-4100. Remover 1165 may be heated to 80 °C using the hotplate on top of the fume hood (no higher as the flash point is of Microposit 1165 is 85 °C) to hasten the process. Rinse with IPA. Collect waste 1165 in appropriate container.

A.5 Thick film resist process

AZ P4620 is a thick film resist, used for making a patterned laser cutting debris protection layer, which will be removed after the laser milling procedure.

A.5.1 *AZ P4620 procedure*

1. Set one hotplate to 200 °C for baking out, another to 110 °C.

2. Clean substrates well (piranha solution is recommended). Bake at 200 °C for a few minutes to remove water.

3. Apply 0.5% diphenylsilanediol in PGME. Spin coat using Adh_promoter program. Bake at 180 °C for 2 min. Cool to RT.

4. Dispense AZ P4620 on wafer and spin coat on Cee model 200X using SCHEELINE-P4620-10um program.

5. Perform edge-bead removal on the spinner using EBR-1 and 2 programs.

6. Softbake 110 °C for 180 sec. Cool to RT.

7. Exposure dose: 1500-1700 mJ/cm^2 or 180 s at 10 mW/cm^2.

8. Develop with AZ 400K: water diluted 1:4 by immersion for 300 s (for 10 μm, 60 s will do) at RT. For 25 μm, 1:3 AZ400K: water. Rinse with water.

9. Dry with nitrogen gun, put on 110 °C hotplate for a few minutes. Do not bake above the T_g (glass transition temperature) of 105-110 °C if you intend to strip the resist later with solvent.

10. Cool, then inspect.

11. If needed, strip with undiluted AZ 400K. You may need to sonicate to speed up the process. Rinse with water spray and dry with nitrogen gun.

A.6 Microfabricated gold electrode cleaning

After microfabrication steps and laser cutting were completed, the electrodes were cleaned in solvents and DI water. A Ti etch (Transene TFT) was used to remove the top

Ti adhesion layer while sonicating for 2 s. The gold electrodes on Kapton/Si substrate were then cleaned as follows:

1. Solvent rinse (acetone, methanol, IPA, ethanol)

2. Acid bath nitric sulfuric (2 water: 1 nitric : 1 sulfuric)

3. Rinse in DI.

4. 2 min oxygen plasma at 1 Torr.

5. Cycling in Na phosphate buffer 0.1 M pH 6.75

A.7   Cee 200X Spin Coater Programs

Spin coating is used to apply a uniform film of liquid resist. Tables A.1 through A.7 are the recipes programmed into the spin coater (Cee 200X) and used for the fabrication of the sensor. They are arranged by file name in the order they are used. Each program is a sequence of steps. The spin speed for each step is given, followed by the rate at which that speed is approached, and the hold time at the programmed speed prior to proceeding to the next step.

Table A.1 Adh_promoter – for use with diphenysilanediol adhesion promoter

Step	Velocity (RPM)	Ramp (RPM/s)	Time (s)
1	500	500	5
2	5000	750	60
3	50	300	1

Table A.2 EBR-1 – First step of edge-bead removal

Step	Velocity (RPM)	Ramp (RPM/s)	Time (s)
1	30	10	5
2	30	10	60
3	30	10	1

Table A.3 EBR-2 – Second step of edge-bead removal

Step	Velocity (RPM)	Ramp (RPM/s)	Time (s)
1	100	5	5
2	1000	100	30
3	100	100	1

Table A.4 SCHEELINE-AZ5214E-1p4um – Spin coating AZ5214E to final thickness of 4 μm.

Step	Velocity (RPM)	Ramp (RPM/s)	Time (s)
1	300	300	1
2	1000	200	5
3	4000	500	25
4	300	500	10

Table A.5 SCHEELINE-AZ5214E-2um – Spin coating AZ5214E to final (cured) thickness of 4 μm.

Step	Velocity (RPM)	Ramp (RPM/s)	Time (s)
1	300	300	1
2	1000	200	5
3	2000	500	25
4	300	500	10

Table A.6 SCHEELINE-HD4100 – Spin coating HD-4100 photosensitive polyimide to a final (cured) thickness of 5 μm.

| Step	Velocity (RPM)	Ramp (RPM/s)	Time (s)
1	300	300	1
2	1000	200	5
3	4000	500	45
4	300	500	5

Table A.7 SCHEELINE-P4620-10um – Spin coating AZP4620 photoresist to a final (cured) thickness of 10 μm.

Step	Velocity (RPM)	Ramp (RPM/s)	Time (s)
1	300	300	1
2	500	300	5
3	2000	500	40
4	300	500	10

APPENDIX B

OPTICAL PROFILER DATA

3D optical profilometry was used to obtain the recess depth of the micro-working

electrode. The instrument, a Wyko NT 1000, is an application of interferometry to

examining surface topography.
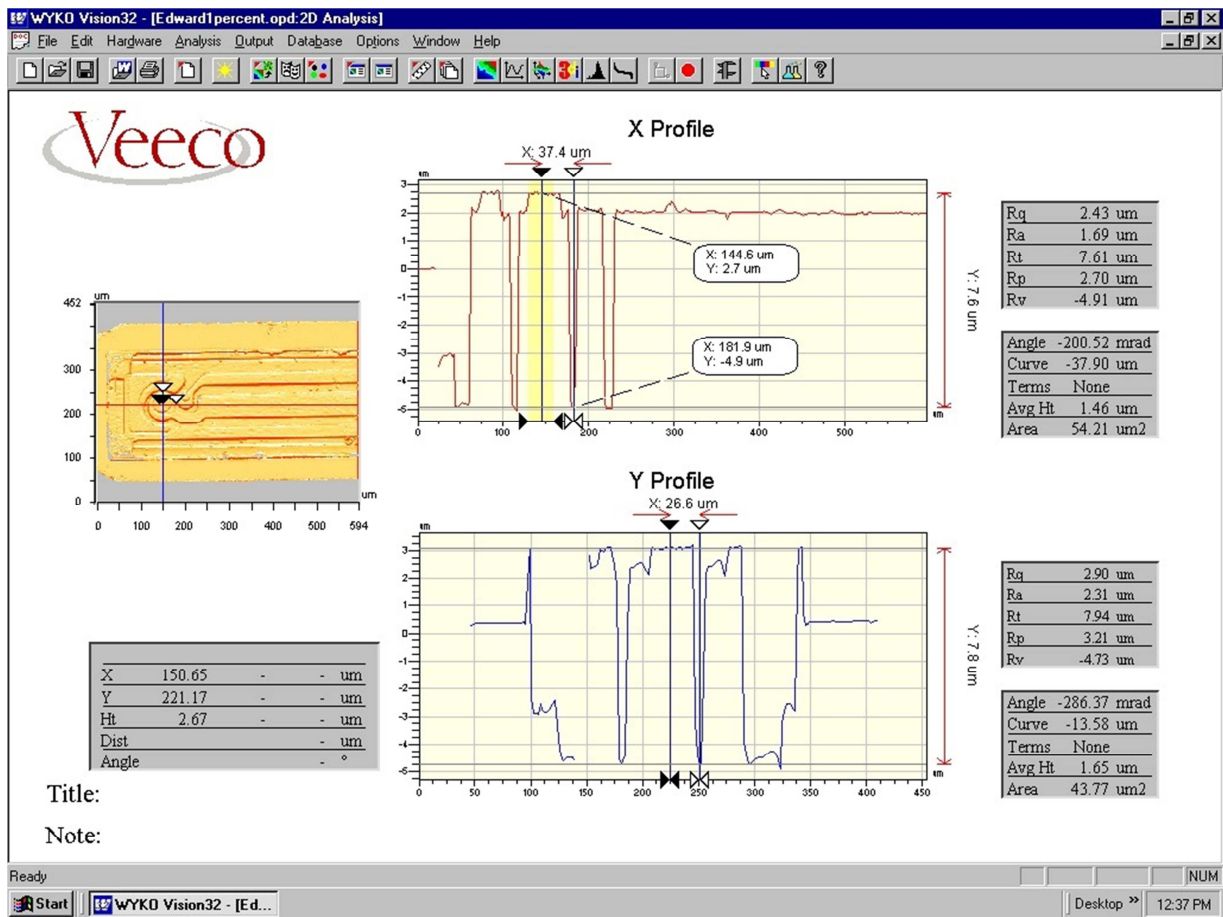
Figure B.1. Screenshot of Wyko NT 1000 profiler program with microelectrode under measurement.

APPENDIX C

DROPLET LAUNCHER AND CAMERA CONTROL

C.1 Droplet launcher program

A droplet launcher drive circuit was made to generate a high-voltage pulse controlled by TTL pulse from digital port 7 of the National Instruments USB-6009 data acquisition module. A LabVIEW application program called "Camera and HV control" was written to independently control the pulses to trigger the camera and the droplet launcher on command (Figure C.1 and Figure C.3). The time that the camera is recording as well the HV pulse ON time could be set in milliseconds, as well as the time delay between camera and HV pulse.

C.2 Camera external triggering

The Hirose connector of the Stingray camera allows an external trigger source to be used instead of the default internal triggering. A box with "Trigger" input and "Camera Ready" output was constructed for this purpose (Figure C.4). The recording of a frame can be triggered and this can be adjusted to level- or edge-trigger using the control panel. A delay can be introduced as well. Normally this is used in conjunction with an LED strobe for illumination of the drop, where the trigger source is the TTL sync from a function generator. The "Camera ON" pulse generated by port 6 of the

USB-6009 is AND'ed with the TTL sync and sent to the camera "Trigger" input (Figure

C.2). The maximum camera frame rate is 149.53 Hz.
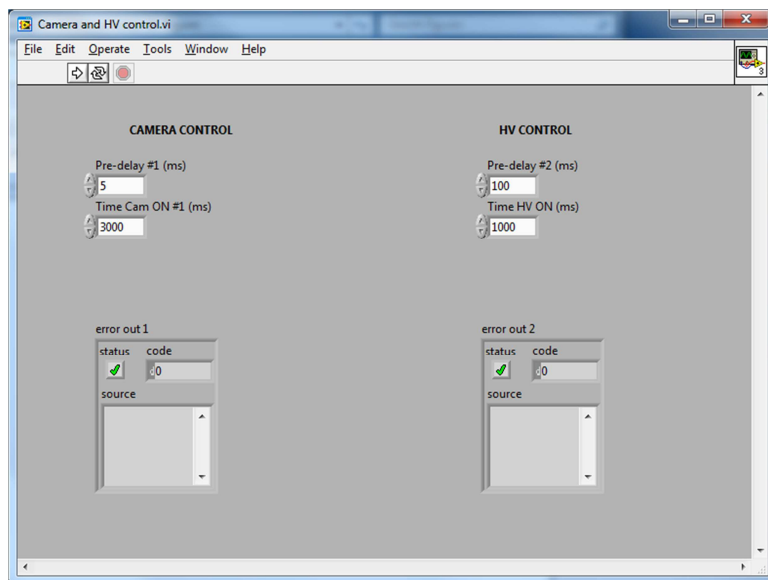
Figure C.1. Top: Screenshot of LabVIEW "Camera and HV control" program. Bottom: Diagram showing the variables "Pre-delay" and "Time ON" in relation to the control pulse.
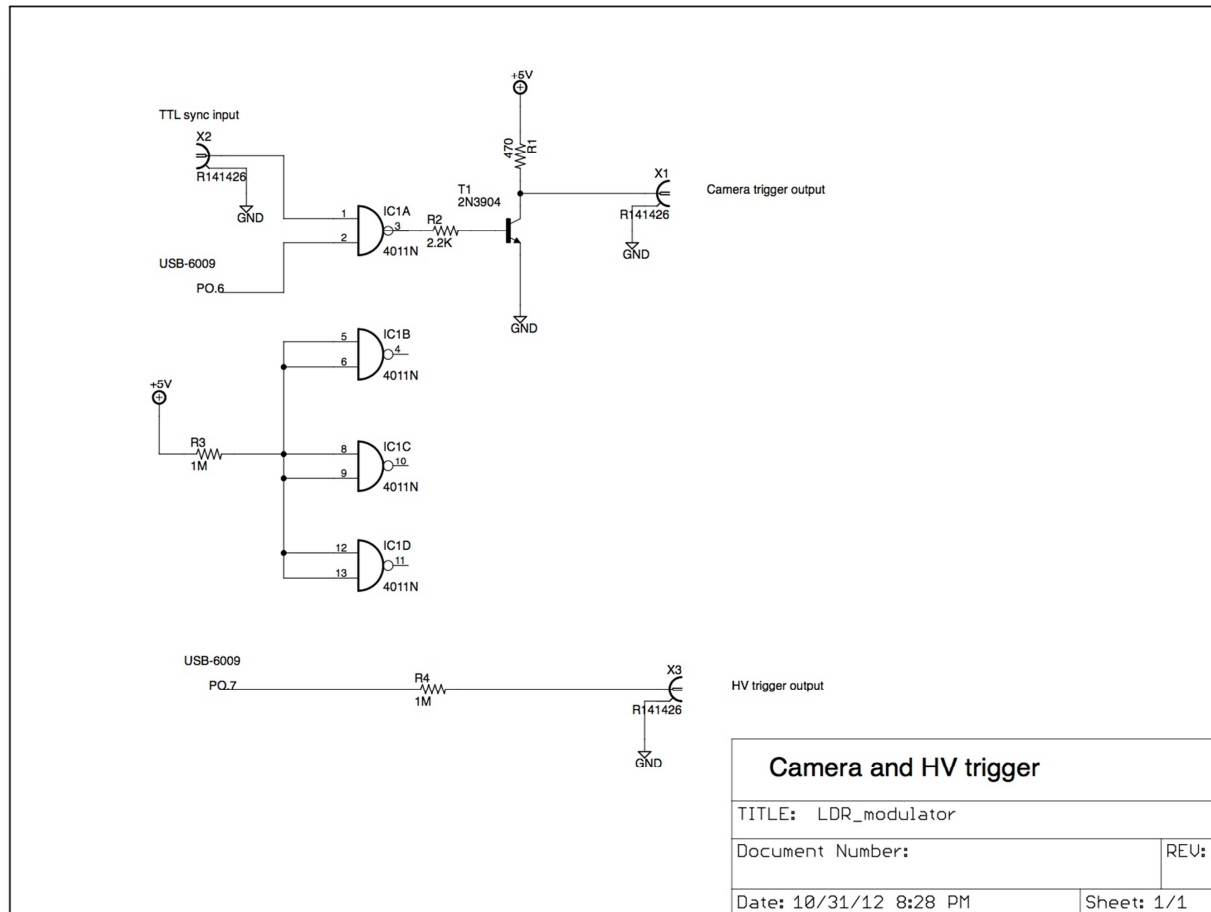
Figure C.2. Camera and HV trigger circuit, receiving inputs from the USB-6009. Outputs wire to droplet launcher drive and camera breakout box circuits.
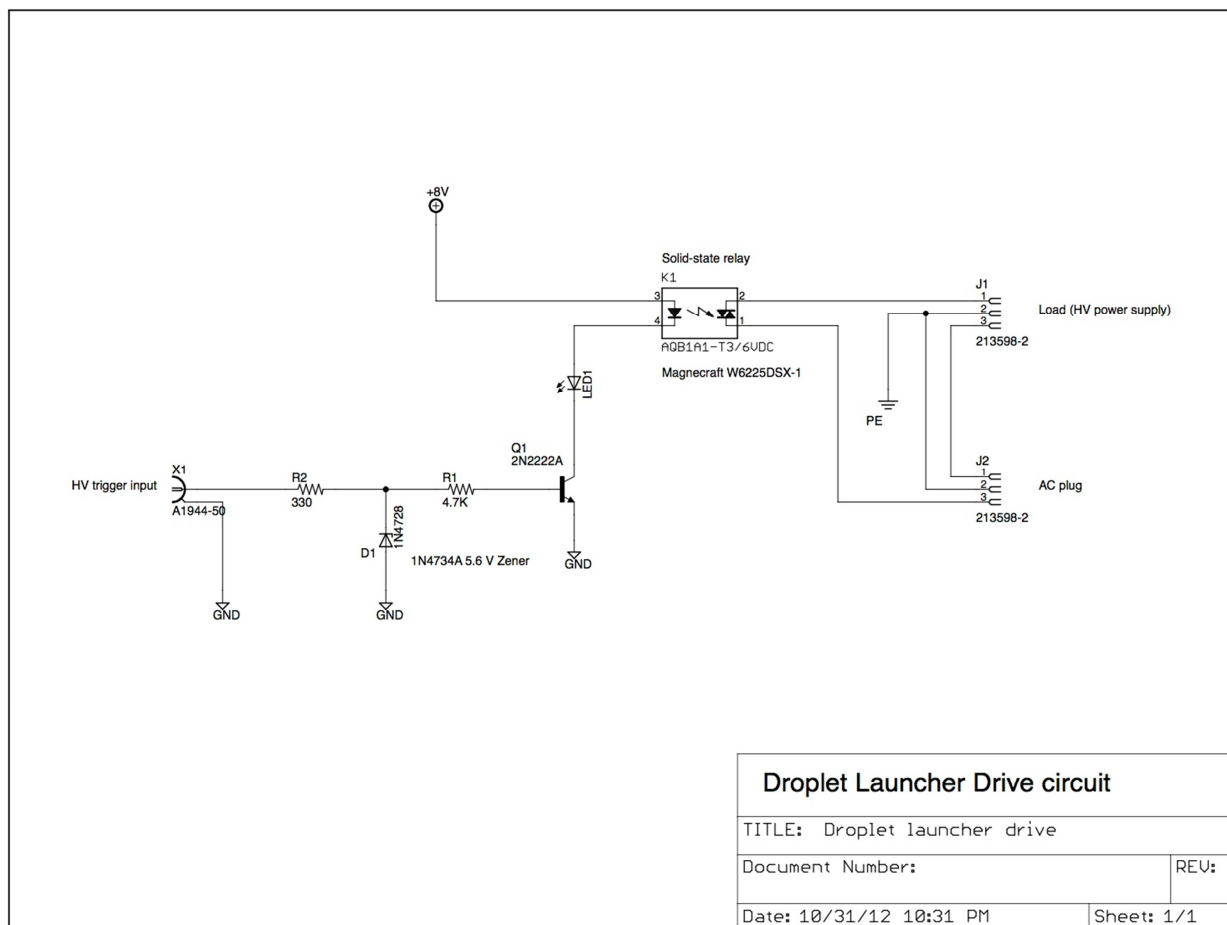
Figure C.3. Droplet launcher drive circuit, receiving input from HV trigger and controlling AC power to the Sauter high-voltage power supply.
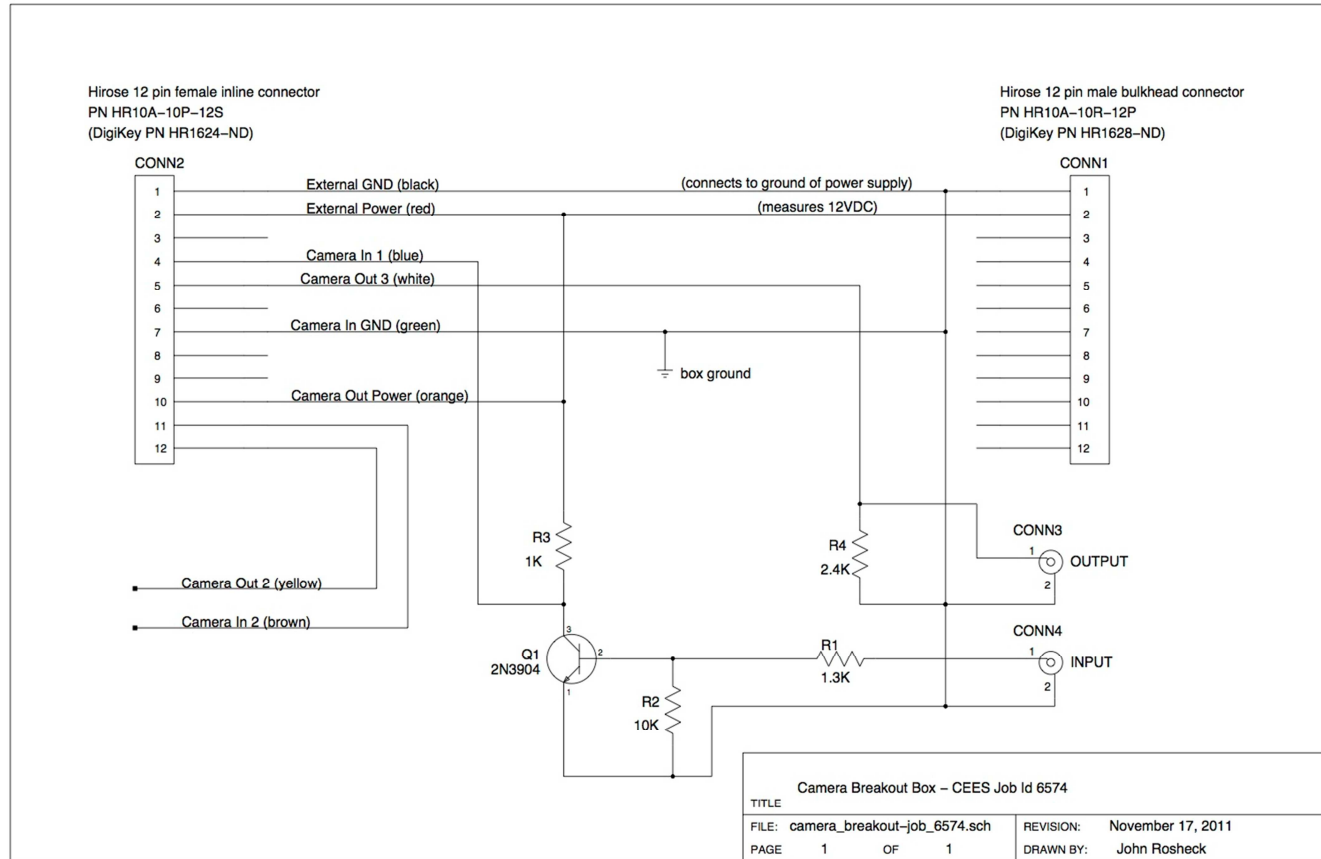
Figure C.4. Camera breakout box (constructed with the assistance of John Rosheck). Input is taken from the camera trigger signal, and output to the Stingray camera external trigger.
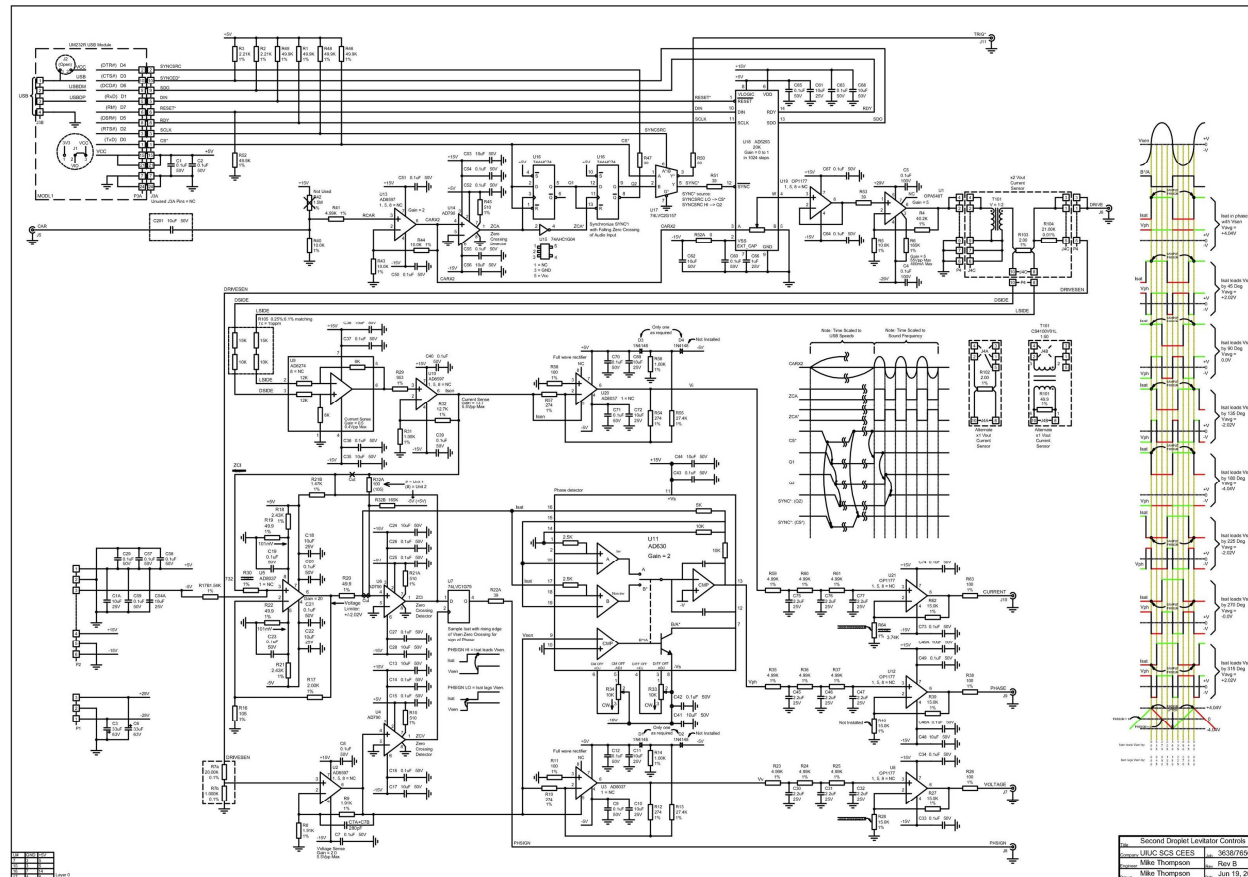
APPENDIX D

LDR AMPLIFIER AND CONTROL CIRCUIT

Figure D.1 Schematic of LDR amplifier circuit built and designed by Michael Thompson.

APPENDIX E

DETERMINATION OF LDR RESONANT FREQUENCY

E.1   LDR resonator forced response

To accurately determine the LDR resonator's frequency, the resonator is driven by a

sine wave of 40 volts peak-to-peak amplitude. Using the phase-locking capability of the

LDR amplifier/controller circuit, voltage signals proportional to current through the

piezos and phase of this current relative to the driving signal are obtained and are here

plotted against the driving frequency. The graphs (Figure E.1) show that current

maxima do not coincide with a minimum in phase (where resistive dissipation

dominates); this is due to the 100-Hz resolution of the experiment around the resonance

frequency. This hysteresis is estimated to be about 1 kHz, and is thought to arise from

coupling between the LDR gap and the electrical impedance. Guyomar, et al. (*J. Phys. III

France*, **1997**, *7*, 1197-1208) investigated the nonlinear behavior of a piezoelectric

Langevin transducer and noted a hysteresis effect of the resonance frequency when the

frequency is swept in the up or down direction.
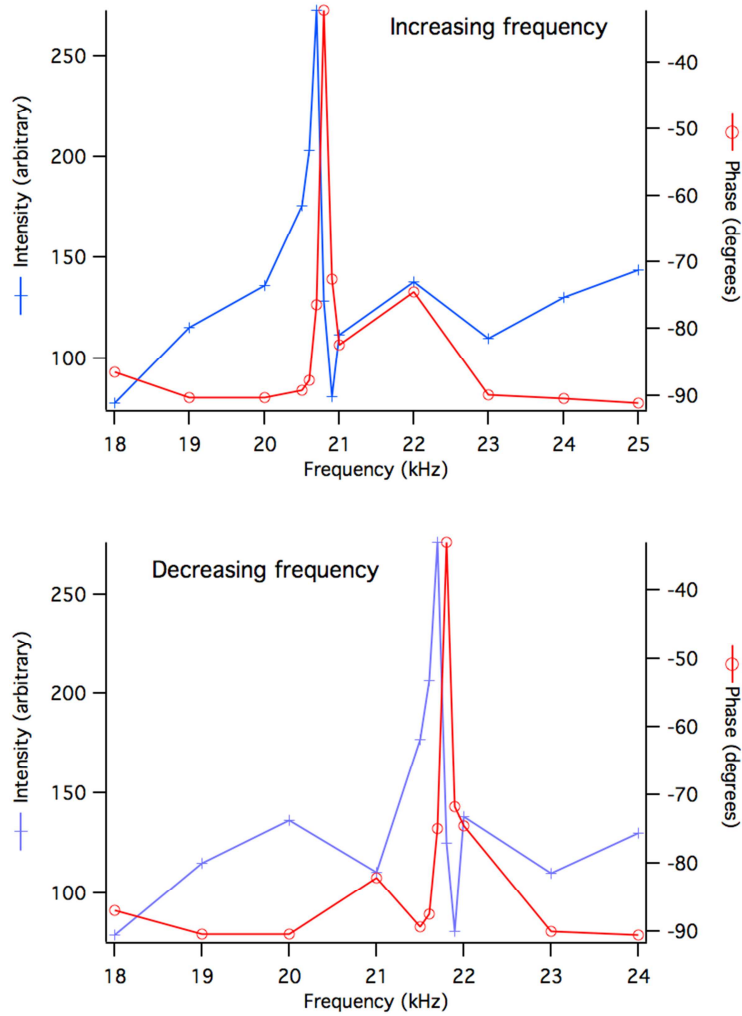
Figure E.1. Graphs of LDR resonator forced response. Intensity units are proportional to current through the crystal resonators. Driving sine wave amplitude is 40 $V_{p\text{-}p}$. Phase shifts measured in relation to driving sine wave. Top: Response with increasing frequency sweep. Bottom: Response with decreasing frequency sweep. Data was obtained using the LDR amplifier and controller circuit.

E.2   LDR resonator free response

An alternative method of determining resonance frequency of the LDR resonator is to tap the horn and acquire the generated piezoelectric voltage. The resonator cable was connected to a data acquisition computer, and the resulting time domain signal is Fourier transformed. Data from 5 trials show that two major peaks agree exactly: The taller peak is at 21289 Hz; the second tallest one is at 18359 Hz. The small mechanical and electrical amplitudes generated this way minimize nonlinear effects. The two smaller peaks at higher frequencies are at 35742 and 39257 Hz.
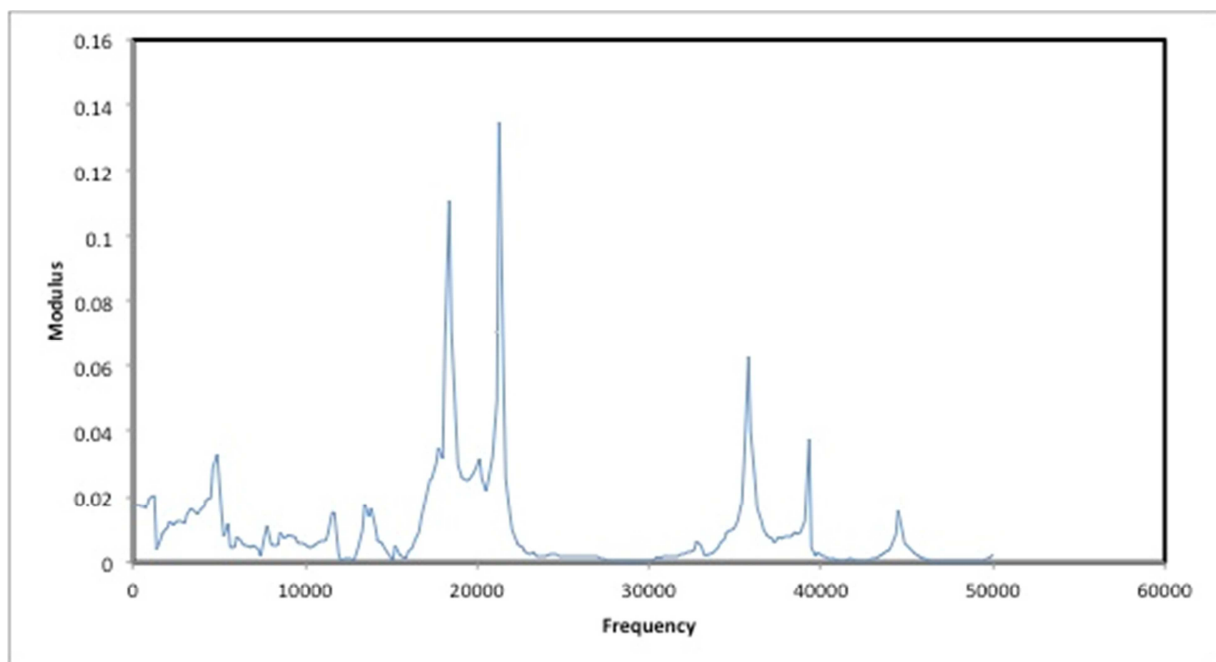
Figure E.2 The Fourier-transform spectrum of the free-response data showing the resonant frequencies of the LDR resonator.